

T-4229

Migration Velocity Analysis

by
Zhenyue Liu

T-4229

A thesis submitted to the Faculty and the Board of Trustees of the Colorado School of Mines in partial fulfillment of the requirements for the degree of Doctor of Philosophy (Mathematical and Computer Sciences).

Golden, Colorado

Date _____

Signed: _____
Zhenyue Liu

Approved: _____
Dr. Norman Bleistein
Professor of Mathematics
Thesis Advisor

Golden, Colorado

Date _____

Dr. Graeme Fairweather
Professor and Head
Department of Mathematical and
Computer Sciences

ABSTRACT

Prestack depth migration, which can both handle dipping reflectors and lateral velocity variations, is a robust method for imaging complex structures. In order to process data by this method, one often needs to have a more accurate velocity model than may be obtained from simple velocity analysis methods, such as normal moveout.

On the other hand, prestack depth migration itself is an attractive tool for doing velocity analysis because of its high sensitivity to the velocity model. Two approaches to migration velocity analysis have become prominent: depth-focusing analysis (DFA) and residual-curvature analysis (RCA). So far, the formulas used in both approaches for updating velocity are derived under the assumptions of horizontal reflectors, lateral velocity homogeneity, or small offset. Therefore, those conventional approaches lack sufficient computational efficiency and accuracy when a velocity distribution has strong, lateral variations.

This thesis addresses the development of a general, quantitative representation between the imaged depths and migration velocity. Based on ray theory, I have found that the migration process can be described by using the so-called imaging equations. From this viewpoint, I have studied relationships between the residual moveout and the error of migration velocity in a general context. For a medium with weak lateral velocity variations, I have proved that the residual velocity can be estimated by hyperbolic residual moveout and no iteration is required. To handle lateral velocity variations, I used a perturbation method to derive an analytical formula to iteratively update the velocity from residual moveout. In my derivation, I impose no limitation on offset, dip, or velocity distribution as long as the velocity perturbation is sufficiently

small. My formula estimates the update in velocity by computing a derivative function of imaged depths with respect to velocity in a general background medium context. This formula is more accurate than conventional formulas based on hyperbolic residual moveout when the medium has strongly lateral velocity variations; therefore, it is a major contribution of this thesis. Based on this formula, I revise the RCA method for doing velocity analysis in complex structural media. In addition, with help of the imaging equations, I analyse properties in a common image gather (CIG), discuss the sensitivity of migration-based velocity analysis, and show what factors affect the sensitivity.

The theory and formulas developed here are available both for the 2-D case and for the 3-D case. For converted waves and anisotropic media, I also offer some suggestions on how to develop corresponding formulas.

The theory and methodology in this thesis have been tested on synthetic data (including the Marmousi data) and on physical-tank data that are recorded in a scaled earth model.

TABLE OF CONTENTS

ABSTRACT		iii
LIST OF FIGURES		vii
ACKNOWLEDGMENTS		x
Chapter 1 INTRODUCTION		1
1.1 Paper Review		1
1.1.1 Depth-focusing analysis		2
1.1.2 Residual-curvature analysis		4
1.1.3 Comparison with reflection tomography		6
1.2 Limitations in Conventional Approaches		8
1.3 Technical Work in this Thesis		10
Chapter 2 IMAGING EQUATIONS		12
2.1 Mathematical Derivation		13
2.2 Solutions for Constant Velocity		16
2.3 3-D Case		17
2.4 Summary		19
Chapter 3 IMAGE ANALYSIS IN A CIG		20
3.1 Common-shot Case		22
3.2 Common-offset Case		24
3.3 Multiple-layer Case		26
Chapter 4 HYPERBOLIC RESIDUAL MOVEOUT		30
4.1 Residual Moveout Representations		31
4.1.1 Constant velocity and horizontal reflector		32
4.1.2 General case		32
4.2 Velocity Estimates for Constant Migration Velocity		36
4.2.1 Constant medium velocity		37
4.2.2 Laterally invariant medium velocity		38
4.2.3 Higher residual terms		41

4.2.4	Lateral velocity anomaly	43
4.3	Some Extensions	45
4.3.1	Common shot case	45
4.3.2	3-D case	46
4.4	Limitation on a Two-layer Model	49
4.5	Computer Implementation	50
4.6	Summary	51
Chapter 5	ITERATIVE APPROACH: METHODOLOGY	57
5.1	Velocity Analysis by Perturbation	58
5.1.1	Mathematical derivation	58
5.1.2	Computational techniques	64
5.2	Sensitivity of Migration Velocity Analysis	68
5.3	Simple-Iteration Approach	72
5.4	Some Extensions	73
5.4.1	3-D case	73
5.4.2	Converted waves	74
5.5	Summary	75
Chapter 6	ITERATIVE APPROACH: COMPUTER IMPLEMENTATION	77
6.1	Synthetic Data	78
6.2	Physical-tank Data	81
6.3	Marmousi Data	83
6.4	Summary	85
Chapter 7	CONCLUSIONS	102
	REFERENCES	105
Appendix A	DEPTH VARIATION TO VELOCITY	107
Appendix B	RMO VELOCITY REPRESENTATION FOR $V(Z)$	110
Appendix C	LATERAL VELOCITY ANOMALY	111
Appendix D	EQUATION SYSTEM FOR PERTURBATION	117
Appendix E	DERIVATIVE FUNCTIONS IN SIMPLE CASES	119

LIST OF FIGURES

2.1	Reflection geometry for the 2-D case.	13
3.1	Sketch of ray paths. ϕ is the dipping angle of the reflector, and θ is half the angle between the source and receiver ray paths.	21
3.2	Two-layer model. c_1 and c_2 are layer velocities, d_1 and d_2 are layer thicknesses, and θ_1 and θ_2 are angles of raypath from the vertical.	26
4.1	A Sketch for Common Image Gather.	31
4.2	Two-layer model.	49
4.3	Subsurface model used to generate synthetic seismic traces.	53
4.4	The contours of relative error between the RMO velocity and the rms velocity. The error increases with depth and dip.	53
4.5	The migrated data with the constant velocity. The offset is 100 meters.	54
4.6	One of the common image gathers from data migrated with the constant velocity. The traces are located at 1.4 km in Figure 4.5.	54
4.7	Velocity spectrum for the CIG in Figure 4.6.	55
4.8	Residual moveout correction for the CIG in Figure 4.6.	55
4.9	Stacking for the partially migrated data of the ten offsets.	56
4.10	Poststack residual time migration of the data in Figure 4.7.	56
5.1	Macro model.	66
5.2	Layer model. The gray shading denotes the target layer for velocity analysis.	69
6.1	The true velocity model. The velocity unit is m/s.	85
6.2	Synthetic data: (a) with offset of 100 meters and (b) with offset of 900 meters.	86

6.3	Prestack migration with the initial constant velocity. The offset is 100 meters.	87
6.4	Two common-image gathers from the migrated data with the initial velocity.	87
6.5	Four common-image gathers from the migrated data with the initial velocity. The numbers 1, 2, 3, etc, correspond to outputs of different CIGs.	88
6.6	Final estimated model from velocity analysis.	88
6.7	Common image gathers from the migrated data with the velocity in Figure 5.6.	89
6.8	Migration with the estimated velocity model in Figure 6.6.	89
6.9	Migration with true velocity model in Figure 6.1.	90
6.10	Measured velocity model.	90
6.11	Physical-tank data: (a) with offset of 268.2 meters and (b) with offset of 1243.6 meters.	91
6.12	Velocity analysis on the physical-tank data. The measured velocities: $c_1 = 3581$, $c_2 = 4801$, $c_3 = 6831$, $c_4 = 4801$	92
6.13	Estimated velocity model from velocity analysis.	93
6.14	Five-offset stacked migration output for the physical-tank data, AGC applied to the stack. The input velocity model is shown in Figure 6.13.	93
6.15	Five-offset stacked inversion output for the physical-tank data, AGC applied to the stack. The input velocity model is shown in Figure 6.1.	94
6.16	Estimated velocity model from velocity analysis by perturbation.	94
6.17	Five-offset stacked migration output for the physical-tank data. The input velocity model is in Figure 6.16.	95
6.18	The Marmousi velocity model. The darker shading denotes higher velocity.	96
6.19	The minimum-offset Marmousi data. The offset is 200 meters.	96
6.20	The estimated velocity model using the first-arrival operator.	97

6.21	The updated velocity model using the paraxial ray tracer.	97
6.22	Comparison of the true velocity model to the estimated one. The dark curve denotes the true velocity and the gray denotes the estimated velocity. The top figure is at location $x=8$ km; the middle, at location $x=6$ km; the bottom, at location $x=4$ km.	98
6.23	19-offset stacked migration output for the Marmousi data. The input velocity is one in Figure 6.21.	99
6.24	19-offset stacked migration output for the Marmousi data. The true velocity is used.	99
6.25	Ten common image gathers. 19 offsets in each CIG. The image location ranges from 4 km to 4.25 km.	100
6.26	Ten common image gathers. 19 offsets in each CIG. The image location ranges from 6 km to 6.25 km.	100
6.27	Ten common image gathers. 19 offsets in each CIG. The image location ranges from 8 km to 8.25 km.	101
6.28	Ten common image gathers from migrated data using the true velocity. The image location ranges from 6 km to 6.25 km.	101

ACKNOWLEDGMENTS

I would deeply thank Prof. Norman Bleistein for his encouragement, advice and support. I am grateful to Prof. David Olson, Jack Cohen, Steven Pruess and Dr. Dave Hale for their comments and helpful discussions. This research was supported by the Office of Naval Research, Mathematics Division, and members of the Consortium Projection on Seismic Inverse Methods for Complex Structures at the Center for Wave Phenomena, Colorado School of Mines.

Chapter 1

INTRODUCTION

Structural imaging is an essential process in seismic exploration. A successful implementation of this process relies on knowledge of background parameters for propagation of data into the earth. Among these parameters, velocity is a critical one because of its coherent relation with the dynamic characteristics of reflection signals. Therefore, velocity estimation has become one of the most important tasks in exploration seismology. Velocity analysis is the process of estimating background velocities from measurements of moveout or stacking power. In general, there are three ways for doing velocity analysis: normal moveout, dip moveout and prestack migration.

Normal moveout (NMO) is the most basic method for determining velocities from seismic data. However, this method assumes horizontal reflectors and lateral velocity homogeneity. Dip-moveout (DMO) improves on NMO processing by properly accommodating dipping reflectors, but still cannot accommodate lateral velocity variations. Compared to these two methods, prestack migration provides a powerful tool for doing velocity analysis because of its high sensitivity to the velocity error and its ability to handle both reflector dips and lateral velocity variations.

1.1 Paper Review

Two approaches to migration velocity analysis have been developed: depth-focusing analysis (DFA) and residual-curvature analysis (RCA). Depth-focusing anal-

ysis is based on using stacking power to measure velocity error. Residual-curvature analysis is based on using residual moveout to measure velocity error. Here, I will give an overview on papers of these two approaches. Moreover, I will make a brief comparison between migration-based analysis and the reflection tomography approach.

1.1.1 Depth-focusing analysis

The idea of velocity analysis based on differential solutions of the scalar wave equation was first introduced by Doherty and Claerbout (1974). They used the 15-degree finite-difference migration algorithm and worked with single CMP gathers to carry out velocity estimation from unstacked seismic data. Yilmaz and Chambers (1984) extended the migration-based approach to include more than one CMP gather in each analysis. This extension allows proper treatment of dipping events and yields velocity information that is more appropriate for use in migration. The migration process was implemented by using downward extrapolation in the Fourier transform domain. Jeanot et al. (1986) then generalized the method to prestack depth migration in the form of depth-focusing analysis by determining the focused depth in the process of downward continuation. Subsequently, MacKay and Abma (1989) showed how the DFA data volume could be used to form a well-focused seismic section. The new section, the focal-surface image, estimates the results of prestack depth migration using the updated velocities.

The DFA approach is based on these principles: (1) when the migration velocities are exact, the two imaging conditions, zero time and zero offset, yield a focused image during downward continuation; (2) when the migration velocities are in error, reflected energy collapses to zero offset at depths that are inconsistent with the zero-time imaging condition; (3) by interpreting the nonzero times at which focusing actually

occurs, the migration velocities can be updated iteratively.

A simple formula is used to update velocity in the DFA method:

$$V_r = V_m \frac{Z_m + \delta}{Z_m}, \quad (1.1)$$

where Z_m is the migration depth, V_m is the migration velocity, δ is half the depth-difference between the focusing and migration depth, and V_r is the updated velocity. The formula (1.1) is strictly valid for horizontal reflectors, small offset angles, and constant velocities. For a depth-variable velocity, V_r and V_m are viewed as the rms velocities. If the effect of steep dip is included, the modified formula (MacKay, 1991) is

$$V_r = V_m \frac{Z_m + \delta}{Z_m} \left(\frac{\cos \theta_m}{\cos \theta_r} \right)^3, \quad (1.2)$$

where θ_m is the migrated dip and θ_r is the real structural dip. Unfortunately, this formula cannot be used to update velocities because θ_r is not known.

MacKay and Abma (1992) discussed how to avoid divergence in the velocity-updating procedure, when reflector dips and lateral velocity variations exist. They applied a damping factor to the interpreted depth errors. In addition, the interpretation of the focusing depth is frequently affected by seismic energy from dipping interfaces, diffractions, and noise. To reduce possible ambiguity in the DFA interpretation process, MacKay and Abma (1993) introduced a new attribute for determining focusing based on estimates of the radius of wavefront curvature.

The large amount of the ion required for downward continuation may limit use of the DFA approach for routine processing. Kim and Gonzalez (1991) presented the Kirchhoff integral approach to the downward continuation. The flexibility of the Kirchhoff integral allows one to compute only the zero-offset trace at each depth point

and to avoid most of computation for the downward continuation of unstacked data.

1.1.2 Residual-curvature analysis

The formula for updating velocity in the DFA approach is dip-limited, so repeated prestack migration is required even for a constant-velocity medium. In comparison, residual-curvature analysis (RCA) is an alternative to migration velocity analysis that is able to overcome the dip limitations of DFA.

In the RCA method, the migrated prestack data are sorted into common-image gathers (CIGs). They have also been called common-receiver gathers (CRGs) or common-reflection point gathers (CRPs). In each common-image gather, the migrated data have the same imaged horizontal location. Residual-curvature analysis is based on this principle; after prestack migration with the correct velocity, the imaged depths in a CIG must be the same regardless of offset; otherwise, after prestack migration with an erroneous velocity, the imaged depths in a CIG from different offsets will differ from each other; the differences of imaged depth in CIGs provide information for updating the velocity iteratively.

Al-Yahya (1989) discussed residual-curvature analysis by iterative shot profile migration. He measured the velocity errors by estimating the curvature of residual moveout. The residual moveout in a CIG in his paper is represented by

$$z_m^2 = \gamma^2 z^2 + (\gamma^2 - 1)a^2, \quad (1.3)$$

where a is the offset between the shot and the imaged location, z_m is the imaged depth, z is the actual depth, and γ is the ratio of the true rms slowness to the migration rms slowness. The derivation of equation (1.3) is based on small offset, horizontal reflectors, and laterally invariant velocity. Later, Lee and Zhang (1992) generalized

the condition of horizontal reflector into small-angle dip by using the dip-corrected residual moveout equation, from which equation (1.3) is modified by

$$z_m^2 = \gamma^2 z^2 + (\gamma^2 - 1)(a_0^2 + (a - a_0)^2), \quad (1.4)$$

where a_0 is a quantity related to the reflector dip. With the help of this more accurate equation, one can implement residual migration to avoid remigration, or reduce the number of the number of iterations required to produce a satisfactory image. However, Lee and Zhang's approach involves two unknown parameters—the true velocity and the reflector dip, at each imaged location, which makes this approach less convenient than the determination of one single parameter.

Residual moveout in common offset migration is relatively independent of reflector dip, so common offset migration provides a better approach in residual-velocity analysis than common shot migration. Deregowski (1990) realized this advantage of common offset migration over other migration techniques and developed a velocity analysis method by using common-offset depth migration. In his approach, the velocity is updated iteratively by using the residual-moveout correction. Liu and Bleistein (1992) derived a general residual-moveout representation under the assumption of small offset and proved that residual moveout in common offset migration is insensitive to reflector dip for a depth-dependent velocity. This conclusion implies the velocity can be corrected without a further iteration for a laterally invariant velocity. To handle complex structures, Lanford and Levander (1993) proposed an RCA method that is based on a layer-stripping Kirchhoff algorithm with geometrical ray tracing in heterogeneous media. They assumed that the medium is composed of constant-velocity layers and updated velocity along the ray path in a way similar to tomographic reconstruction. By using perturbation theory, Liu and Bleistein (1994)

developed an analytical formulation for residual moveout that is valid for any velocity distribution and any subsurface structure. This formulation can also be used to analyze the sensitivity of migration velocity analysis.

1.1.3 Comparison with reflection tomography

As an alternative to migration velocity analysis, reflection tomography is an important approach to velocity analysis that handles lateral velocity variations for velocity estimation. Therefore, it is essential to make a comparison between migration velocity analysis and reflection tomography.

The tomography technique (refraction tomography) has been widely used in Borehole Geophysics and Vertical Seismic Profile (VSP) to estimate medium velocity based on information of the first arrival traveltimes. It is called reflection tomography when this technique is applied to surface seismic reflection data. In the tomographic approach to the inverse problem, the medium velocity is determined by minimizing a misfit function that represents the deviation of traveltimes. The formulation in the tomographic approach is set up analytically, so one can analyse some aspects of velocity inversion, such as stability, resolution and computational efficiency.

However, there are some difficulties in the present reflection tomographic approach. First, picking reflected events from seismic signals in reflection tomography is much more difficult than picking the first arrivals in refraction tomography. The events in the unmigrated data are frequently distorted by correlated noise. This problem can be improved by picking reflectors in the postmigrated domain (Stork, 1992). Secondly, the inversion problem in reflection tomography is very ill-posed. Compared to refraction tomography, the raypath coverage in reflection tomography is more sparse and, therefore, uniqueness is an issue, with multiple solutions being a

possibility. Finally, the construction of raypaths (actually, specular raypaths) strongly relies on the reflector position, both on depths and on slopes. Although the depths can be included in the inverse problem as a parameter to be determined (Stork and Clayton, 1991), generally it is difficult to determine the slopes accurately.

In contrast, migration velocity analysis can use the semblance method to measure residual moveouts and pick reflectors in the stacked, migrated domain. In this way, migration velocity analysis will give more reliable information for picking. Furthermore, with the help of the macro model concept, migration velocity analysis can apply a recursive procedure to estimate interval velocities. Thus, the computation can be made more stable by applying the method to only a few unknowns at each recursion. Finally, formulation in migration velocity analysis can be set up analytically by using perturbation theory which is similar to the analysis done in tomography (Liu and Bleistein, 1994). The estimate of velocities in this formulation also depends on specular raypaths, as in reflection tomography. In contrast, Liu and Bleistein's approach selects the specular raypaths, based on the stationary-phase principle that produces the migration imaging, instead of on the measurement of reflector slopes. Therefore, this approach is more stable and less computationally costly than reflection tomography.

In summary, both migration velocity analysis and reflection tomography are important methods for handling lateral velocity variation in velocity estimation. The similarity between these two methods allows them to "learn" from each other in order to solve the problem of velocity estimation in complex structures. For instance, Liu and Bleistein (1994) derived an analytical formula to describe the relation between residual moveout and residual velocity, the idea for which was suggested by tomography. On the other hand, reflection tomography may improve stability by using the

macro model concept.

1.2 Limitations in Conventional Approaches

Migration velocity analysis must address two issues to succeed: (1) how to establish a criterion for knowing if a migration velocity is acceptable; (2) how to update the velocity, if it is unacceptable. In DFA, a migration velocity is acceptable if the difference between migration depth and focusing depth is zero. In RCA, a migration velocity is acceptable if the difference between imaged depths from different offsets is zero. Quantitatively, these differences can be used to update the velocity in a routine way. To date, a variety of updating formulas have been developed. These formulas degrade with increasing complexity of media (lateral velocity variation and reflector dip), because of rough approximations used to estimate velocity. Although iteration generally is helpful in obtaining a more accurate velocity, a good approximation not only reduces the number of iterations but also guarantees the convergence. The conventional formulas for updating velocity were derived under one or more assumptions as follows:

- (i) lateral velocity homogeneity;
- (ii) small offset;
- (iii) horizontal reflector.

In MacKay and Abma's DFA approach (1992), all three assumptions are used. In RCA, the assumptions vary with migration types. For common-shot migration or common-receiver migration, Al-Yahya's formula (1989) used all three assumptions. Lee and Zhang (1992) derived a formula that replaces assumption (iii) by the assumption of small dip. For common-offset migration, Deregowski's formula (1990) used the first two assumptions. [This statement was verified by Liu and Bleistein

(1992).] Both DFA and RCA use assumptions (i) and (ii). Under the assumption of a small offset, the residual moveout can be approximated by a hyperbola or a parabola. However, this approximation is poor when the velocity has an obvious lateral variation.

Conventional approaches for updating the velocity inspect information at each midpoint individually. This information is not reliable when conflicting events exist because velocity estimation will depend on which event is used. Furthermore, the conventional approaches update the average velocities that are assumed to be equal to the rms velocities and then convert rms velocities into interval velocities by the Dix equation or other methods. Unfortunately, when the velocity has a lateral anomaly, this kind of average velocity may differ significantly from the rms velocity (Lynn and Claerbout, 1982; Toldi, 1989), which may cause divergence in the velocity-updating procedure.

Because of such limitations, conventional approaches to velocity analysis encounter difficulties in handling complex structures (such as the Marmousi model). To overcome these limitations, some geophysicists used a macro-model (layer-stripping) method for estimating the interval velocity directly. A macro-model consists of velocities and velocity interfaces (subsurfaces). The model is determined by layer-stripping, in a top down procedure; the velocity of each layer is updated iteratively by using depth-focusing analysis or residual-curvature analysis; the velocity interface is imaged by using the corrected velocity. The whole process may be accomplished with interpretation based on geological knowledge. So far, the present macro-model method has two significant drawbacks. First, the velocity distribution is assumed to be constant in layers. In fact, velocity may vary within a layer. Secondly, there has not been an efficient formula for updating velocity, which results in inaccuracy and inefficiency in

velocity estimates.

In summary, prestack depth migration is sensitive to the velocity model. Residual curvatures in migrated data provide information indicating if the migration velocity is correct or not. However, there exist drawbacks in the present formulas for updating velocity due to rough approximations used. Therefore, the derivation of a more accurate formula is required to handle complex structures.

1.3 Technical Work in this Thesis

Migration imaging depends on what velocity is used and, on the other hand, migration imaging determines what velocity should be used. Therefore, it is essential to give a quantitative description to the relationship between migration imaging and migration velocity, especially to the relationship between residual moveout and residual velocity.

In Chapter 2, I set up the imaging equations which are a kinematic representation of migration processes. I address the equivalency of the imaging equations to Snell's Law, so these equations also can be applied to converted waves and anisotropic media. The imaging equations are the foundation of the velocity analysis formulas derived in Chapter 4 and Chapter 5.

In Chapter 3, I analyze image properties at a common image gather based on the imaging equations. For constant layered velocity, I derive formulas for the sensitivity of velocity analysis and show what factors affect the accuracy of migration velocity analysis.

In Chapter 4, I derive the residual moveout representations under the assumption of small offset. Based on these representations, I define the residual moveout (RMO) velocity and show how the RMO velocity is related to the rms velocity. I prove that

the RMO velocity can be estimated by hyperbolic residual moveout without iteration and it is a good approximation of the rms velocity for a medium with weakly lateral velocity variations. In addition, I show a failure example on a simple two-layer model where the lateral variation is no longer small.

In Chapter 5, I develop iterative approaches to handle lateral velocity variations. Based on the perturbation method, I derive an analytical relationship between the residual moveout and residual velocity and discuss some computational techniques for estimating velocity by using this relationship. My formula estimates the update in velocity by computing a derivative function of imaged depths with respect to velocity in a general background medium context. This formula is more accurate than conventional ones based on hyperbolic residual moveout when the medium has strongly lateral velocity variations. In addition, I propose a simple-iteration algorithm as a supplement to the perturbation approach. Furthermore, I derive more formulas for the sensitivity of migration velocity analysis, which are a development of the formulas in Chapter 3.

In Chapter 6, I show the application of the iterative method in Chapter 5. The computer implementations include simple synthetic data, physical-tank data, and the Marmousi data.

The formulas of velocity analysis in this thesis are derived for 2-D acoustic media as those in the papers Liu and Bleistein (1992), Liu and Bleistein (1994), Liu and Bleistein (1995). Here, I have partially extended these results to 3-D and I also present suggestions on how to extend to converted waves and anisotropic media.

Chapter 2

IMAGING EQUATIONS

Let us assume that seismic waves are generated and recorded in response to a near-surface source. The recorded signals will provide information about the underground-velocity distribution and reflector geometry. That information is contained in amplitude and phase of seismic waves. Under the assumption of high frequency, phase information is simplified to travelttime (the WKBJ approximation). Compared to amplitude, travelttime information in seismic waves is more reliable. For example, the amplitude in a P-P reflection is greatly affected by the existence of shear waves, but the travelttime is much less affected. Consequently, studying methods based on travelttime is essential in exploration seismology. The theory that deals with wave propagation for very high-frequency signals is called geometrical optics. Using this tool, Hubral and Krey (1980) did fundamental work for measuring travelttime and estimating the stacking velocity. In this thesis, I am also going to utilize this tool for measuring residual moveout and estimating the migration velocity.

Given a reflector and a medium velocity, one can obtain a space-time curve in the recorded signals by ray theory. This process is *forward modeling*. Conversely, given a time-space curve and a velocity, one can determine a reflector that generates this space-time curve. This process is *migration imaging*. Furthermore, if there are multichannel seismic data, velocity itself also can be determined from the relationship between the subsurface imaging and the migration velocity. This process is *velocity analysis*.

In this chapter, equations for describing migration imaging will be set up based on Snell's Law. These equations are the kinematical representations of the migration processes.

2.1 Mathematical Derivation

Consider the two dimensional situation. I denote by \mathbf{x} a 2-D vector, $\mathbf{x} = (x, z)$. Let $\mathbf{x}_s = (x_s(\xi), z_s(\xi))$ be source positions and $\mathbf{x}_r = (x_r(\xi), z_r(\xi))$ be receiver positions located on the datum surface (not necessarily flat), where ξ is a position parameter on the surface. For example, in common offset, ξ would be the midpoint of a source/receiver pair; in common shot, ξ would be a coordinate labeling the receiver location, that is, representing the offset from the fixed source. For any point below the surface, $\tau_s(\mathbf{x}_s, \mathbf{x})$ denotes traveltime for a downgoing wave from \mathbf{x}_s to \mathbf{x} , and $\tau_r(\mathbf{x}, \mathbf{x}_r)$, denotes traveltime for an upgoing wave from \mathbf{x} to \mathbf{x}_r . (See Figure 2.1.)

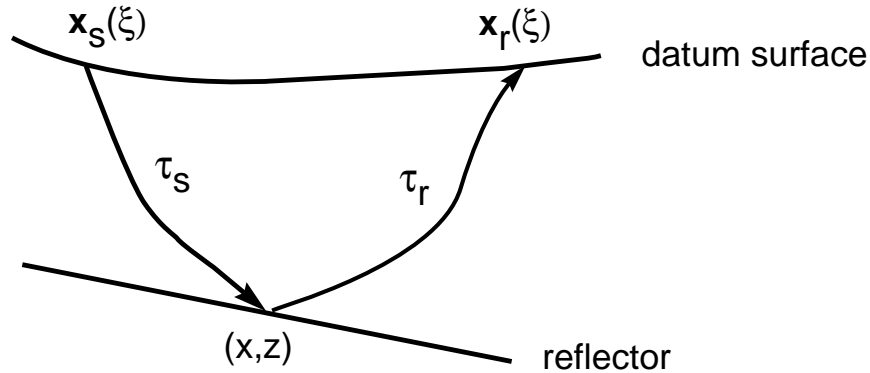


FIG. 2.1. Reflection geometry for the 2-D case.

Given a reflector, one can compute the total reflection traveltime $t(\xi)$ by using

$$\tau_s(\mathbf{x}_s, \mathbf{x}) + \tau_r(\mathbf{x}, \mathbf{x}_r) = t(\xi), \quad (2.1)$$

where the reflection point \mathbf{x} satisfies Snell's Law,

$$[\nabla_{\mathbf{x}} \tau_s(\mathbf{x}_s, \mathbf{x}) + \nabla_{\mathbf{x}} \tau_r(\mathbf{x}, \mathbf{x}_r)] \cdot \frac{d\mathbf{x}}{d\xi} = 0. \quad (2.2)$$

Equations (2.1) and (2.2) describe the forward modeling process for a given reflector, so they are called the *modeling equations*. On the other hand, the total reflection travelttime function $t(\xi)$ also can be used to determine the reflector position. Notice that the reflection point $\mathbf{x} = (x, z)$ is dependent on the position ξ on the surface. By differentiating equation (2.1) with respect to ξ , I obtain

$$\frac{\partial \tau_s}{\partial \xi} + \frac{\partial \tau_r}{\partial \xi} + [\nabla_{\mathbf{x}} (\tau_s + \tau_r)] \cdot \frac{d\mathbf{x}}{d\xi} = \frac{dt}{d\xi}. \quad (2.3)$$

Using equation (2.2) to eliminate the third term on the left side of equation (2.3), one obtains

$$\frac{\partial \tau_s(\mathbf{x}_s, \mathbf{x})}{\partial \xi} + \frac{\partial \tau_r(\mathbf{x}, \mathbf{x}_r)}{\partial \xi} = \frac{dt}{d\xi}. \quad (2.4)$$

Thus, each point $\mathbf{x} = (x, z)$ of the reflector (therefore, the reflector itself) is determined by the simultaneous solution of equations (2.1) and (2.4); i.e., \mathbf{x} will satisfy

$$\tau_s(\mathbf{x}_s, \mathbf{x}) + \tau_r(\mathbf{x}, \mathbf{x}_r) = t(\xi), \quad (2.5)$$

$$\frac{\partial \tau_s(\mathbf{x}_s, \mathbf{x})}{\partial \xi} + \frac{\partial \tau_r(\mathbf{x}, \mathbf{x}_r)}{\partial \xi} = \frac{dt}{d\xi}. \quad (2.6)$$

Geometrically, equation (2.6) shows that the reflector is just the envelope of the wavefronts from source/receiver pairs. Therefore, I will call equation (2.6) the *envelope condition*. This condition also can be derived by using the stationary-phase method in the asymptotic expansion of the Kirchhoff migration operator to reflection data under the assumption of high frequency. However, the derivation here is more direct.

Equations (2.5) and (2.6) are the dual of equations (2.1) and (2.2). They describe the migration imaging process for a given space-time curve, so I call them the *imaging equations*. These two equations hold for any kind of seismic acquisition geometry. Specifically, let us consider the common offset case with a flat datum surface.

With no loss of generality, Let $z_s = z_r = 0$. The source and receiver positions can be described by the horizontal coordinates x_s and x_r only. Let y denote the midpoint and h the half-offset:

$$x_s = y - h, \quad x_r = y + h. \quad (2.7)$$

Then, since $\xi = y$, equations (2.5) and (2.6) become

$$\tau_s(x_s, \mathbf{x}) + \tau_r(\mathbf{x}, x_r) = t(y, h), \quad (2.8)$$

$$\frac{\partial \tau_s}{\partial y} + \frac{\partial \tau_r}{\partial y} = \frac{\partial t}{\partial y}. \quad (2.9)$$

Equations (2.8) and (2.9) show that if the offset-traveltime curve $t(y, h)$ (therefore, $\partial t / \partial y$) is known for given h , one can compute an imaged depth z at each location x . Furthermore, if a migration velocity equals the true velocity, then the imaged depth z must be independent of the offset h ; otherwise, for a wrong migration velocity, z will vary with the offset h . Consequently, the imaged depths of different offsets provide information for determining the velocity, i.e., for *velocity analysis*.

Similarly, in the common-shot case, equations (2.5) and (2.6) become

$$\tau_s(\mathbf{x}_s, \mathbf{x}) + \tau_r(\mathbf{x}, \mathbf{x}_r) = t(\xi), \quad (2.10)$$

$$\frac{\partial \tau_r}{\partial \xi} = \frac{\partial t}{\partial \xi}. \quad (2.11)$$

2.2 Solutions for Constant Velocity

In particular, suppose that the migration velocity is a constant, c , and the datum surface is the x -axis, that is, $\mathbf{x}_s = (x_s, 0)$ and $\mathbf{x}_r = (x_r, 0)$. Then

$$\tau_s(\mathbf{x}_s, \mathbf{x}) = \rho_s/c, \quad \tau_r(\mathbf{x}, \mathbf{x}_r) = \rho_r/c, \quad (2.12)$$

where

$$\rho_s = \sqrt{(x_s - x)^2 + z^2}, \quad \rho_r = \sqrt{(x_r - x)^2 + z^2}.$$

For this case, equation (2.5) and (2.6) become

$$\rho_s + \rho_r = ct(\xi), \quad (2.13)$$

$$\frac{\partial \rho_s}{\partial \xi} + \frac{\partial \rho_r}{\partial \xi} = c \frac{dt}{d\xi}. \quad (2.14)$$

For the common-offset case, $\xi = y$. Then differentiating here with respect to y and using equation (2.7) yields

$$\frac{\partial \rho_s}{\partial y} = \frac{x_s - x}{\rho_s}, \quad \frac{\partial \rho_r}{\partial y} = \frac{x_r - x}{\rho_r}.$$

Thus, equations (2.8) and (2.9) are simplified to algebraic forms:

$$\rho_s + \rho_r = ct(y, h), \quad (2.15)$$

$$\frac{x_s - x}{\rho_s} + \frac{x_r - x}{\rho_r} = c \frac{\partial t}{\partial y}. \quad (2.16)$$

Although the above equations are still not easy to solve, there is an explicit solution for the zero offset. In fact, $h = 0$ implies that $x_s = x_r = y$ and $\rho_s = \rho_r =$

$\sqrt{(y-x)^2 + z^2}$. Therefore, equations (2.15) and (2.16) are further simplified to

$$\sqrt{(y-x)^2 + z^2} = \frac{c}{2}t(y), \quad (2.17)$$

$$\frac{y-x}{\sqrt{(y-x)^2 + z^2}} = \frac{c}{2} \frac{\partial t}{\partial y}. \quad (2.18)$$

These two equations yield the solution

$$x = y - \frac{c^2}{4}t(y) \frac{\partial t}{\partial y},$$

and

$$z = \frac{c}{2}t(y) \sqrt{1 - \frac{c^2}{4} \left(\frac{\partial t}{\partial y} \right)^2}.$$

In general, equations (2.8) and (2.9) cannot be solved explicitly. However, these two equations represent a general, quantitative relationship between migration imaging and velocity distribution. This relationship will be helpful to derive formulas for velocity estimation.

2.3 3-D Case

For the 3-D case, the derivations and formulas are completely analogous to the 2-D case, so I omit a detailed derivation and just list the main results.

In the 3-D case, two parameters are required to describe the datum surface: $\boldsymbol{\xi} = (\xi_1, \xi_2)$, ξ_1 —in-line direction and ξ_2 —cross-line direction. Parallel to the definitions in the 2-D case, I define

$$\boldsymbol{x} = (x_1, x_2, z),$$

$$\boldsymbol{x}_s = (x_{1s}(\boldsymbol{\xi}), x_{2s}(\boldsymbol{\xi}), z_s(\boldsymbol{\xi})),$$

$$\mathbf{x}_r = (x_{1r}(\boldsymbol{\xi}), x_{2r}(\boldsymbol{\xi}), z_r(\boldsymbol{\xi})).$$

Unless specified otherwise, symbols with index 1 denote the variables along the in-line direction and symbols with index 2 denote the variables along the cross-line direction. Snell's law is stated as

$$[\nabla_{\mathbf{x}} \tau_s(\mathbf{x}_s, \mathbf{x}) + \nabla_{\mathbf{x}} \tau_r(\mathbf{x}, \mathbf{x}_r)] \cdot \frac{\partial \mathbf{x}}{\partial \xi_i} = 0, \quad i = 1, 2. \quad (2.19)$$

Now, the imaging equations become

$$\tau_s(\mathbf{x}_s, \mathbf{x}) + \tau_r(\mathbf{x}, \mathbf{x}_r) = t(\boldsymbol{\xi}), \quad (2.20)$$

$$\frac{\partial \tau_s(\mathbf{x}_s, \mathbf{x})}{\partial \xi_i} + \frac{\partial \tau_r(\mathbf{x}, \mathbf{x}_r)}{\partial \xi_i} = \frac{\partial t}{\partial \xi_i}, \quad i = 1, 2. \quad (2.21)$$

Let $\mathbf{h} = (h_1, h_2)$ denote the offset vector and $\mathbf{y} = (y_1, y_2)$ denote the midpoint vector. In the common-offset case, the imaging equations are

$$\tau_s(\mathbf{x}_s, \mathbf{x}) + \tau_r(\mathbf{x}, \mathbf{x}_r) = t(\mathbf{y}, \mathbf{h}), \quad (2.22)$$

$$\frac{\partial \tau_s}{\partial y_i} + \frac{\partial \tau_r}{\partial y_i} = \frac{\partial t}{\partial y_i}, \quad i = 1, 2. \quad (2.23)$$

For the zero offset and a constant velocity, c , there is an explicit solution for the above equations:

$$\mathbf{x} = \mathbf{y} - \frac{c^2}{4} t(\mathbf{y}) \nabla_{\mathbf{y}} t(\mathbf{y}),$$

and

$$z = \frac{c}{2} t(\mathbf{y}) \sqrt{1 - \frac{c^2}{4} |\nabla_{\mathbf{y}} t(\mathbf{y})|^2}.$$

2.4 Summary

The imaging equations provide a general kinematic representation of migration processes. Some applications of these equations to residual migration have been addressed in the literature (Etgen, 1989; Zhang, 1991). In this thesis, I use these equations to formulate algorithms for migration velocity analysis. From the derivation of these equations, it is clear and meaningful that the envelope condition (2.6) and Snell's law (2.2) are equivalent. Because Snell's law is a general statement in reflection seismology, it is concluded that the imaging equations hold for converted waves in isotropic or anisotropic media, as well. That means, velocity analysis algorithms derived from the imaging equations in acoustic media can be generalized to converted waves and anisotropic media.

Chapter 3

IMAGE ANALYSIS IN A CIG

Velocity analysis must be done on multichannel data. After prestack migration, the imaged traces are sorted into common image gathers (CIGs). The imaged depths in CIGs provide information on migration velocity. In this chapter, I am going to quantify the relationship between the imaged depths and the velocity, based on the imaging equations. For simplicity, suppose that the migration velocity is a constant, c , and the datum surface is the x -axis.

By the definition of a CIG, to study images in a CIG, one should fix the horizontal coordinate, x , of the reflection point. Then, both the imaged depth z and the source-receiver position parameter ξ can be considered to be functions of the velocity c . That is, when the velocity changes, the migration image at a particular trace location changes in the vertical direction. Therefore, z is a function of c . Similarly, when one keeps x unchanged, the image at x will come from different source-receiver pairs for different choices of c . This fact implies, ξ is a function of c , too. Differentiating equation (2.13) with respect to c ,

$$\left[\frac{\partial \rho_s}{\partial z} + \frac{\partial \rho_r}{\partial z} \right] \frac{dz}{dc} + \left[\frac{\partial \rho_s}{\partial \xi} + \frac{\partial \rho_r}{\partial \xi} \right] \frac{d\xi}{dc} = c \frac{dt}{d\xi} \frac{d\xi}{dc} + t(\xi). \quad (3.1)$$

Now, by using equation (2.14) to eliminate $\partial \rho_s / \partial \xi$ and $\partial \rho_r / \partial \xi$, and using

$$\frac{\partial \rho_s}{\partial z} = \frac{z}{\rho_s}, \quad \frac{\partial \rho_r}{\partial z} = \frac{z}{\rho_r}, \quad (3.2)$$

I obtain

$$(z/\rho_s + z/\rho_r) \frac{dz}{dc} = t(\xi) = (\rho_s + \rho_r)/c. \quad (3.3)$$

Solving for dz/dc , then,

$$\frac{dz}{dc} = \frac{\rho_s \rho_r}{c z} > 0. \quad (3.4)$$

Introduce angles θ and ϕ as in Figure 3.1. Then,

$$\rho_s = \frac{z}{\cos(\theta - \phi)}, \quad \rho_r = \frac{z}{\cos(\theta + \phi)}, \quad (3.5)$$

$$\frac{dz}{dc} = \frac{z}{c \cos(\theta - \phi) \cos(\theta + \phi)}. \quad (3.6)$$

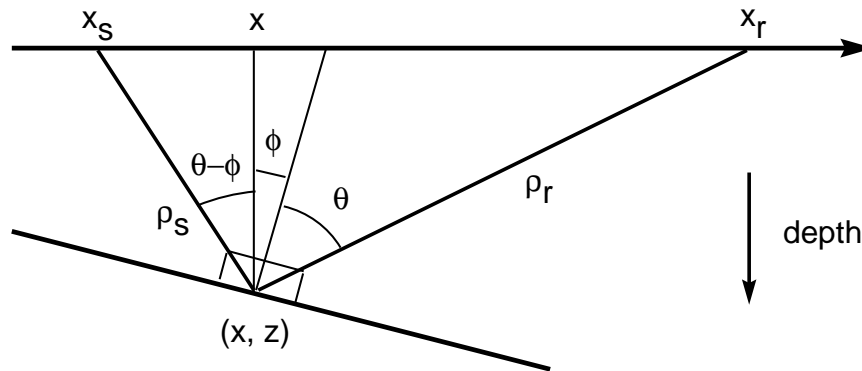


FIG. 3.1. Sketch of ray paths. ϕ is the dipping angle of the reflector, and θ is half the angle between the source and receiver ray paths.

Equation (3.4) shows that the imaged depth increases with the migration velocity for fixed x , no matter what the true medium velocity is. This conclusion is true even for a general migration velocity. Further discussion can be found in Appendix A, where I will show this result for downward propagating waves and also show that the sign is opposite for upgoing waves. Moreover, equation (3.4) allows us to do

quantitative analysis, so one may find how the degree of the image distortion depends on the magnitude of the velocity error and on the reflection geometry.

Suppose that there are multichannel data. For a given migration velocity, c , common image gathers are sorted from the migrated data. Let c^* denote the true medium velocity. At $c = c^*$, the imaged depths in a CIG must be the same, i.e., z is independent of pairs of $\{x_s, x_r\}$ for a fixed x . With no loss of generality, I suppose that the source is to the left of the receiver, that is, $\theta > 0$.

3.1 Common-shot Case

In the common-shot case, different imaged traces in a CIG correspond to different shot positions at a fixed trace location. Thus, our objective here is to describe the sensitivity of the velocity analysis technique to changes in shot location over the gather of shots that image a particular reflector at the given trace location. From Figure 3.1, I have

$$x_s - x = -z \tan(\theta - \phi). \quad (3.7)$$

As in the discussion above, at $c = c^*$, the true velocity, the imaged depth in a CIG is independent of shot position; that is,

$$\left. \frac{\partial z}{\partial x_s} \right|_{c=c^*} = 0. \quad (3.8)$$

If one moves from one shot position to another, i.e., differentiating with respect to x_s in equation (3.7) and evaluating the result at $c = c^*$ yields

$$1 = \left. \frac{-z}{\cos^2(\theta - \phi)} \frac{d\theta}{dx_s} \right|_{c=c^*}, \quad (3.9)$$

or

$$\frac{d\theta}{dx_s} = -\left. \frac{\cos^2(\theta - \phi)}{z} \right|_{c=c^*}. \quad (3.10)$$

By differentiating equation (3.6) with respect to x_s and using equations (3.8) and (3.10)

I find that

$$\frac{\partial^2 z}{\partial x_s \partial c} \Big|_{c=c^*} = -\frac{\sin 2\theta}{c \cos^2(\theta + \phi)} < 0. \quad (3.11)$$

This tells us that the depth deviation *decreases* as the source moves right ($\Delta x_s > 0$).

Now I use (3.11) to obtain error estimates in velocity analysis. From Figure 3.1

I find that

$$\frac{\sin 2\theta}{x_r - x_s} = \frac{\cos(\theta + \phi)}{\rho_s}, \quad \cos(\theta + \phi) = \frac{z}{\rho_r}. \quad (3.12)$$

The first equation here is a result of the law of sines; the second arises from the trigonometry of the right triangle. Furthermore, x_r is the specular receiver position corresponding to the shot x_s and, hence is a function of x_s in the CIG. Now equation (3.11) becomes

$$\frac{\partial^2 z}{\partial x_s \partial c} \Big|_{c=c^*} = \frac{(x_s - x_r) \rho_r}{c^* z \rho_s}. \quad (3.13)$$

This result and (3.8) can now be used to obtain an approximation for the slope of the image position with respect to changes in x_s for c near c^* . The result is

$$\frac{\partial z}{\partial x_s} \approx \frac{\partial z}{\partial x_s} \Big|_{c=c^*} + \frac{\partial^2 z}{\partial x_s \partial c} \Big|_{c=c^*} (c - c^*) = \frac{(x_s - x_r) \rho_r (c - c^*)}{c^* z \rho_s}. \quad (3.14)$$

Suppose that there are two shots, x_{s_1}, x_{s_2} , and $x_{s_1} < x_{s_2}$. Then the difference in imaged depths between these two shots in a CIG can be approximated by

$$z(x_{s_2}) - z(x_{s_1}) \approx \frac{\partial z(x_{s_0})}{\partial x_s} (x_{s_2} - x_{s_1}) \approx (x_{s_0} - x_{r_0}) (x_{s_2} - x_{s_1}) \frac{(c - c^*) \rho_r}{c^* z \rho_s}. \quad (3.15)$$

In this equation, $x_{s_0} = (x_{s_2} + x_{s_1})/2$ and x_{r_0} is the corresponding receiver position producing the specular image of interest on the trace at x . Thus, solving for the relative velocity error, I find that

$$\frac{(c - c^*)}{c^*} \approx \frac{(z(x_{s_2}) - z(x_{s_1})) z}{(x_{s_0} - x_{r_0})(x_{s_2} - x_{s_1})} \frac{\rho_s}{\rho_r} = \frac{\Delta z z}{\Delta x_s (x_{s_0} - x_{r_0})} \frac{\rho_s}{\rho_r}. \quad (3.16)$$

Here, $\Delta z = z(x_{s_2}) - z(x_{s_1})$ and $\Delta x_s = x_{s_2} - x_{s_1}$. This relationship is valid when c approximates c^* and the two shots are close for each other. The quotient ρ_s/ρ_r is greater than one for the negative dip angle, and less than one for the positive dip angle.

In equation (3.16) one see the factors that govern the accuracy of velocity analysis, $(c - c^*)/c^*$, under the assumption that the medium velocity is constant. *The accuracy of velocity analysis for a CIG of common shot images is best for large source-to-receiver offsets, well-separated shot points, and shallower targets, which is well-known but not previously quantified. Interestingly, it is also better for reflectors with positive dip (i.e., receivers located in the down-dip direction relative to the shot point).*

3.2 Common-offset Case

In the common-offset case, different imaged traces in a CIG correspond to different offsets. Thus, I seek a description of the dependence of the image depth z on the half-offset h at a fixed trace location, x . From Figure 3.1,

$$2h = x_r - x_s = z(\tan(\theta - \phi) + \tan(\theta + \phi)). \quad (3.17)$$

Similar to the derivation of (3.11), I find that

$$\left. \frac{\partial^2 z}{\partial h \partial c} \right|_{c=c^*} = \frac{2 \sin 2\theta}{c (\cos^2(\theta + \phi) + \cos^2(\theta - \phi))} > 0. \quad (3.18)$$

This result tells us that the depth deviation *increases* as the offset increases ($\Delta h > 0$).

By using the relations in equation (3.12), equation (3.18) becomes

$$\left. \frac{\partial^2 z}{\partial h \partial c} \right|_{c=c^*} = \frac{2 h}{c z} \frac{2 \rho_s \rho_r}{\rho_s^2 + \rho_r^2}, \quad (3.19)$$

and

$$\frac{\partial z}{\partial h} \approx \frac{2 h}{c^* z} \frac{2 \rho_s \rho_r}{\rho_s^2 + \rho_r^2} (c - c^*). \quad (3.20)$$

Suppose that there are two offsets h_1 , h_2 and $h_1 < h_2$. Then the difference in imaged depths for the two offsets in a CIG is given by the approximation

$$z(h_2) - z(h_1) \approx \frac{\partial z(h_0)}{\partial h} (h_2 - h_1) \approx 2 h_0 (h_2 - h_1) \frac{(c - c^*)}{c^* z} \frac{2 \rho_s \rho_r}{\rho_s^2 + \rho_r^2}, \quad (3.21)$$

where $h_0 = (h_2 + h_1)/2$. Thus,

$$\frac{(c - c^*)}{c^*} \approx \frac{(z(h_2) - z(h_1)) z}{2 h_0 (h_2 - h_1)} \frac{\rho_s^2 + \rho_r^2}{2 \rho_s \rho_r} = \frac{\Delta z z}{2 \Delta h h_0} \frac{\rho_s^2 + \rho_r^2}{2 \rho_s \rho_r}, \quad (3.22)$$

where $\Delta z = z(h_2) - z(h_1)$ and $\Delta h = h_2 - h_1$. This relationship is valid when c approximates c^* and the two offsets are close for each other. The quotient $(\rho_s^2 + \rho_r^2)/2\rho_s\rho_r$ equals one for a horizontal reflector and is greater than one for any given dip angle.

The relationship (3.22) shows us that *the accuracy of velocity analysis for a CIG of common offset images is best when the two offsets are large and greatly different*

from one another, and shallower targets, which, again, is well-known but not previously quantified. Interestingly, *this accuracy deteriorates with increasing dip.*

Note. From the result (3.22), one can conclude that any error of velocity and the difference of the offsets results in a nonzero deviation Δz . More precisely,

$$\Delta z \approx (c - c^*)(h_2 - h_1) \left. \frac{\partial^2 z(h_0)}{\partial h \partial c} \right|_{c=c^*}.$$

Therefore, I define the quantity $\partial^2 z / \partial h \partial c$ as *the sensitivity to the velocity error* for common offset images. Similarly, the quantity $\partial^2 z / \partial x_s \partial c$ can be defined as *the sensitivity to the velocity error* for common shot images.

3.3 Multiple-layer Case

If the medium is made up of more than one layer, the expression for the error estimate should be modified. Let us consider only a simple model that consists of two horizontal layers, in the common-offset situation as in Figure 3.2. Differentiating

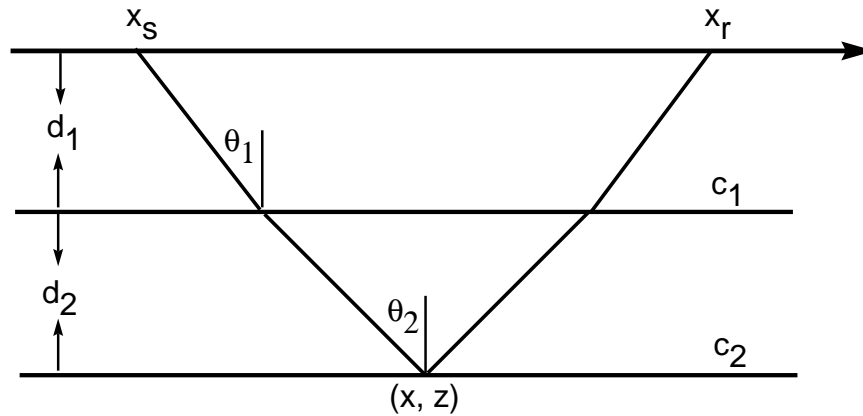


FIG. 3.2. Two-layer model. c_1 and c_2 are layer velocities, d_1 and d_2 are layer thicknesses, and θ_1 and θ_2 are angles of raypath from the vertical.

equation (2.1) with respect to c_2 , and using equation (2.2) yield

$$\left[\frac{\partial \tau_s(\mathbf{x}_s, \mathbf{x})}{\partial z} + \frac{\partial \tau_r(\mathbf{x}, \mathbf{x}_r)}{\partial z} \right] \frac{dz}{dc_2} = - \left[\frac{\partial \tau_s(\mathbf{x}_s, \mathbf{x})}{\partial c_2} + \frac{\partial \tau_r(\mathbf{x}, \mathbf{x}_r)}{\partial c_2} \right]. \quad (3.23)$$

By using the notations shown in Figure 3.2, the traveltimes are represented by

$$\tau_s(\mathbf{x}_s, \mathbf{x}) = \tau_r(\mathbf{x}, \mathbf{x}_r) = \frac{d_1}{c_1 \cos \theta_1} + \frac{d_2}{c_2 \cos \theta_2}. \quad (3.24)$$

Although θ_1 and θ_2 are functions of c_2 , two variations from θ_1 and θ_2 will be balanced to each other from Fermat's principle. Therefore, differentiating equation (3.24) with respect to c_2 will yield

$$\frac{\partial \tau_s}{\partial c_2} = \frac{\partial \tau_r}{\partial c_2} = -\frac{d_2}{c_2^2 \cos \theta_2}. \quad (3.25)$$

Substituting this result and

$$\frac{\partial \tau_s}{\partial z} = \frac{\partial \tau_r}{\partial z} = \frac{\cos \theta_2}{c_2}, \quad (3.26)$$

into equation (3.23), I obtain

$$\frac{dz}{dc_2} = \frac{d_2}{c_2 \cos^2 \theta_2}. \quad (3.27)$$

Now I want to derive a formula for the sensitivity $\partial^2 z / \partial c_2 \partial h$. Firstly, I evaluate c_2 at the true velocity of the second layer, so that the imaged depth z and d_2 will be independent of offset. Introduce the horizontal-slowness parameter

$$p = \frac{\sin \theta_1}{c_1} = \frac{\sin \theta_2}{c_2}. \quad (3.28)$$

Then

$$\cos \theta_1 = \sqrt{1 - c_1^2 p^2}, \quad \cos \theta_2 = \sqrt{1 - c_2^2 p^2}, \quad (3.29)$$

$$h = \frac{d_1 c_1 p}{\sqrt{1 - c_1^2 p^2}} + \frac{d_2 c_2 p}{\sqrt{1 - c_2^2 p^2}}, \quad (3.30)$$

$$\frac{dh}{dp} = \frac{d_1 c_1}{(1 - c_1^2 p^2)^{3/2}} + \frac{d_2 c_2}{(1 - c_2^2 p^2)^{3/2}}. \quad (3.31)$$

From equations (3.27) and (3.29), I have

$$\frac{\partial^2 z}{\partial h \partial c_2} = \frac{d_2}{c_2} \frac{\partial}{\partial h} \left(\frac{1}{\cos^2 \theta_2} \right) = \frac{d_2}{c_2} \frac{\partial}{\partial p} \left(\frac{1}{1 - c_2^2 p^2} \right) \frac{dp}{dh} = \frac{2d_2 c_2 p}{(1 - c_2^2 p^2)^2} \frac{dp}{dh}. \quad (3.32)$$

By using equation (3.31), the above equation becomes

$$\frac{\partial^2 z}{\partial h \partial c_2} = \frac{2d_2 c_2 p}{(1 - c_2^2 p^2)^2} \left[\frac{d_1 c_1}{(1 - c_1^2 p^2)^{3/2}} + \frac{d_2 c_2}{(1 - c_2^2 p^2)^{3/2}} \right]^{-1}. \quad (3.33)$$

When $c_2 \approx c_1$, equation (3.33) is simplified to

$$\left. \frac{\partial^2 z}{\partial h \partial c_2} \right|_{c_2=c_1} = \frac{d_2}{d_1 + d_2} \frac{2 \tan \theta_1}{c_1}. \quad (3.34)$$

Compared to equation (3.18) (let $\phi = 0$), equation (3.34) shows us that for multiple layers, *the sensitivity to the velocity error in a thin layer is reduced by the ratio of the layer thickness to the reflector depth.*

To go a further, I introduce the ratio of the layer velocities, $\eta = c_2/c_1$, then equation (3.33) becomes

$$\frac{\partial^2 z}{\partial h \partial c_2} = \frac{2d_2 \eta p}{(1 - \eta^2 c_1^2 p^2)^2} \left[\frac{d_1}{(1 - c_1^2 p^2)^{3/2}} + \frac{d_2 \eta}{(1 - \eta^2 c_1^2 p^2)^{3/2}} \right]^{-1}. \quad (3.35)$$

When η is small, the above equation can be approximated by

$$\frac{\partial^2 z}{\partial h \partial c_2} \approx 2\eta p \cos^3 \theta_1 \frac{d_2}{d_1}. \quad (3.36)$$

Equation (3.36) quantifies how *the sensitivity to the velocity error deteriorates for a low-velocity zone of the target layer.*

Moreover, for n horizontal layers, equation (3.33) can be generalized to

$$\frac{\partial^2 z}{\partial h \partial c_n} = \frac{2d_n c_n p}{(1 - c_n^2 p^2)^2} \left[\sum_{i=1}^n \frac{d_i c_i}{(1 - c_i^2 p^2)^{3/2}} \right]^{-1}, \quad (3.37)$$

where c_i is the i -th layer velocity and d_i is the thickness of the i -th layer.

For a more complex velocity model, the formula for the sensitivity of velocity analysis could not be so explicit, but it is still computable. The detailed discussion will be seen in Section 5.2.

Chapter 4

HYPERBOLIC RESIDUAL MOVEOUT

When an incorrect velocity is used to migrate multichannel data, the imaged depths in a CIG will differ from each other. In this situation, residual moveout (RMO) is observed in migrated data. Like normal moveout, residual moveout contains information from which one can estimate the medium velocity. Some geophysicists have applied this technique to migration velocity analysis. They assume a hyperbola for residual moveout and estimate an average velocity, then convert this average velocity into the interval velocity. In this chapter, I develop a theoretical basis for this kind of application. Under the assumption of small offsets, I derive general representations for residual moveout by using the imaging equations introduced in Chapter 2. Based on these formulas, I define RMO velocity and show that residual moveout is dominated by the difference between the RMO velocity and migration velocity. For a laterally invariant velocity, I prove that the RMO velocity is a good approximation to the rms velocity, so one can directly estimate velocity by residual-moveout correction. In this way, velocity analysis requires only a single prestack migration, so one can avoid relatively costly remigrations. When the velocity has a weak lateral anomaly and the reflector is horizontal, I develop a formula to calculate the interval velocity from the RMO velocity. For a complex structure, I also show the limitation of this approach for velocity estimation.

4.1 Residual Moveout Representations

Consider the 2-D, common offset case. All notations have the same meaning as those in Chapter 2. Suppose that prestack migration is implemented on a multi-offset data set by using an initial velocity. The migrated data is sorted into CIGs. At each CIG, the imaged depth is a function of offset. i.e., $z = z(h)$ (see Figure 4.1). When the migration velocity is correct, $z(h) = z(0)$ for all offsets. Otherwise, for a wrong velocity, one should expect that $z(h) \neq z(0)$. It is desirable to know the relationship between residual moveout, $z(h) - z(0)$, and the error in velocity. Below, I derive this relationship for the simplest case and then generalize that result.

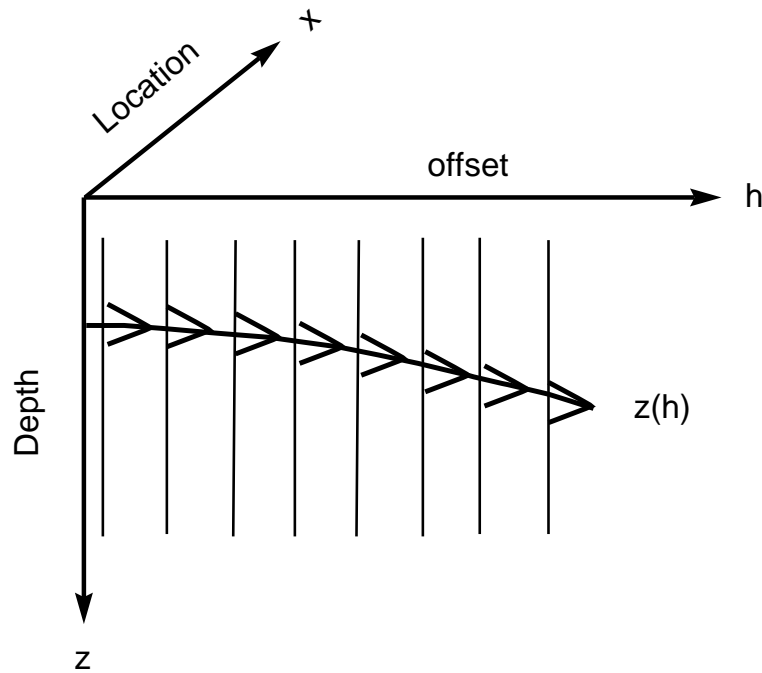


FIG. 4.1. A Sketch for Common Image Gather.

4.1.1 Constant velocity and horizontal reflector

Suppose that the medium velocity is a constant v , migration velocity is a constant c , and the reflector is horizontal. Then the recorded traveltime is given by

$$t^2(y, h) = t^2(y, 0) + \frac{4h^2}{v^2}, \quad (4.1)$$

while the traveltime to the migration image is given by

$$t(y, h) = \frac{2\rho_s}{c} = \frac{2\rho_r}{c} = \frac{2}{c}\sqrt{z^2 + h^2}. \quad (4.2)$$

Solving here for the image depth z as a function of offset yields

$$z^2(h) = \frac{c^2}{4}t^2(y, h) - h^2 = \frac{c^2}{4}t^2(y, 0) + \left(\frac{c^2}{v^2} - 1\right)h^2 = z^2(0) + \left(\frac{c^2}{v^2} - 1\right)h^2. \quad (4.3)$$

That is, the moveout is a hyperbola for $c > v$ or an ellipse for $c < v$:

$$z^2(h) = z^2(0) + \left(\frac{c^2}{v^2} - 1\right)h^2. \quad (4.4)$$

Equation (4.4) shows that the residual moveout is the exact hyperbola or ellipse for constant velocities v and c , and horizontal reflector. This result is parallel to that of moveout in unmigrated data.

4.1.2 General case

For a general velocity or an arbitrary reflector, one should not expect a simple expression such as (4.4). However, the more general result can be approximately derived by considering an asymptotic expansion for small offset. Thus, I seek a

Taylor series for z as a function of h .

First, because z is a symmetric function of h , I obtain

$$\left. \frac{dz}{dh} \right|_{h=0} = 0, \quad \left. \frac{d^3 z}{dh^3} \right|_{h=0} = 0, \quad \text{etc.} \quad (4.5)$$

This result implies the Taylor series expansion

$$z^2(h) = z^2(0) + \left. \frac{1}{2} \frac{d^2 z^2}{dh^2} \right|_{h=0} h^2 + O(h^4). \quad (4.6)$$

Now let us try to estimate the second derivative term.

For fixed x , the midpoint y and the imaged depth z are functions of offset h .

Differentiating equation (2.8) with respect to h , yields

$$\left[\frac{\partial \tau_s}{\partial y} + \frac{\partial \tau_r}{\partial y} \right] \frac{dy}{dh} + \left[\frac{\partial \tau_s}{\partial h} + \frac{\partial \tau_r}{\partial h} \right] + \left[\frac{\partial \tau_s}{\partial z} + \frac{\partial \tau_r}{\partial z} \right] \frac{dz}{dh} = \frac{\partial t}{\partial y} \frac{dy}{dh} + \frac{\partial t}{\partial h}. \quad (4.7)$$

Using equation (2.9) to cancel the first terms on left and right, I obtain

$$\left[\frac{\partial \tau_s}{\partial z} + \frac{\partial \tau_r}{\partial z} \right] \frac{dz}{dh} = \frac{\partial t}{\partial h} - \left[\frac{\partial \tau_s}{\partial h} + \frac{\partial \tau_r}{\partial h} \right]. \quad (4.8)$$

Notice that y is symmetric in h , so

$$\left. \frac{dy}{dh} \right|_{h=0} = 0. \quad (4.9)$$

Using equations (4.5) and (4.9), I find the derivatives of both sides in equation (4.8), with respect to h at $h = 0$, are given by

$$\left. \frac{d}{dh} \left[\frac{\partial t}{\partial h} - \left(\frac{\partial \tau_s}{\partial h} + \frac{\partial \tau_r}{\partial h} \right) \right] \right|_{h=0} = \left. \frac{\partial^2 t}{\partial h^2} \right|_{h=0} - \left[\frac{\partial^2 \tau_s}{\partial h^2} + \frac{\partial^2 \tau_r}{\partial h^2} \right]_{h=0}, \quad (4.10)$$

and

$$\frac{d}{dh} \left[\left(\frac{\partial \tau_s}{\partial z} + \frac{\partial \tau_r}{\partial z} \right) \frac{dz}{dh} \right]_{h=0} = \left[\left(\frac{\partial \tau_s}{\partial z} + \frac{\partial \tau_r}{\partial z} \right) \frac{d^2 z}{dh^2} \right]_{h=0}. \quad (4.11)$$

Differentiating equation (4.8) with respect to h , and using (4.10) and (4.11), I set up the following equation for $d^2 z/dh^2 |_{h=0}$:

$$\left[\left(\frac{\partial \tau_s}{\partial z} + \frac{\partial \tau_r}{\partial z} \right) \frac{d^2 z}{dh^2} \right]_{h=0} = \frac{\partial^2 t}{\partial h^2} \Big|_{h=0} - \left[\frac{\partial^2 \tau_s}{\partial h^2} + \frac{\partial^2 \tau_r}{\partial h^2} \right]_{h=0}. \quad (4.12)$$

Equation (4.12) holds for any medium velocity function, any migration velocity, and an arbitrary reflector. Now I will simplify this equation for the case of constant migration velocity.

Suppose the migration velocity is a constant, c ; then

$$\tau_s = \sqrt{z^2 + (x - y + h)^2}/c, \quad \tau_r = \sqrt{z^2 + (x - y - h)^2}/c, \quad (4.13)$$

and,

$$\frac{\partial \tau_s}{\partial z} \Big|_{h=0} = \frac{\partial \tau_r}{\partial z} \Big|_{h=0} = \frac{z}{c\rho}, \quad (4.14)$$

$$\frac{\partial^2 \tau_s}{\partial h^2} \Big|_{h=0} = \frac{\partial^2 \tau_r}{\partial h^2} \Big|_{h=0} = \frac{1}{c\rho} - \frac{(x - y)^2}{c\rho^3}, \quad (4.15)$$

where

$$\rho = \sqrt{z^2 + (x - y)^2}. \quad (4.16)$$

Equations (4.15) and (4.16) yield

$$\left[\frac{\partial \tau_s}{\partial z} + \frac{\partial \tau_r}{\partial z} \right]_{h=0} = \frac{2z}{c\rho}, \quad (4.17)$$

$$\left[\frac{\partial^2 \tau_s}{\partial h^2} + \frac{\partial^2 \tau_r}{\partial h^2} \right]_{h=0} = \frac{2}{c\rho} - \frac{2(x - y)^2}{c\rho^3}. \quad (4.18)$$

Using these results, equation (4.12) is simplified by

$$\left[\frac{2z}{c\rho} \frac{d^2 z}{dh^2} \right]_{h=0} = \frac{\partial^2 t}{\partial h^2} \Big|_{h=0} + \frac{2(x-y)^2}{c\rho^3} - \frac{2}{c\rho}. \quad (4.19)$$

Furthermore,

$$\left[2z \frac{d^2 z}{dh^2} \right]_{h=0} = \frac{d^2 z^2}{dh^2} \Big|_{h=0}, \quad (4.20)$$

$$\rho = \frac{c}{2} t \Big|_{h=0}, \quad (4.21)$$

$$\frac{(y-x)}{\rho} = \frac{c}{2} \frac{\partial t}{\partial y} \Big|_{h=0}. \quad (4.22)$$

Thus, I obtain the result

$$\frac{d^2 z^2}{dh^2} \Big|_{h=0} = \frac{c^2}{2} \left[t \frac{\partial^2 t}{\partial h^2} + \left(\frac{\partial t}{\partial y} \right)^2 \right]_{h=0} - 2, \quad (4.23)$$

or

$$\frac{d^2 \tau_m^2}{dh^2} \Big|_{h=0} = 2 \left[t \frac{\partial^2 t}{\partial h^2} + \left(\frac{\partial t}{\partial y} \right)^2 \right]_{h=0} - \frac{8}{c^2}, \quad (4.24)$$

where τ_m is the migration time defined by

$$\tau_m = \frac{2z}{c}. \quad (4.25)$$

From equation (4.23), it is concluded that after migration, the the main part of the residual moveout is determined by the migration velocity c , curvature of the unmigrated data $t\partial^2 t/\partial h^2$, and slope of the unmigrated data $\partial t/\partial y$. This statement is true for a constant migration velocity, any medium velocity distribution, and an arbitrary reflector. Based on equation (4.23), I define a residual-moveout velocity

(RMO velocity) by

$$\frac{1}{[v_{rmo}]^2} = \frac{1}{4} \left[t \frac{\partial^2 t}{\partial h^2} + \left(\frac{\partial t}{\partial y} \right)^2 \right]_{h=0}. \quad (4.26)$$

By using the RMO velocity, the residual moveout is written as

$$\tau_m^2(h) = \tau_m^2(0) + \left(\frac{1}{v_{rmo}^2} - \frac{1}{c^2} \right) 4h^2 + O(h^4). \quad (4.27)$$

Equation (4.27) shows the RMO velocity can be directly estimated from the residual moveout. Compared to NMO velocity, a new term, $\partial t / \partial y$, is involved in the definition of RMO velocity, and these two velocities will be equal if and only if $\partial t / \partial y = 0$. In the following examples, it is seen that this term removes the dip effect in RMO velocity analysis and makes the RMO velocity approximately equal to rms velocity under the condition of lateral velocity homogeneity. In addition, the RMO velocity analysis based on equation (4.27) is actually composed of an inverse NMO with velocity c and an NMO velocity analysis. Therefore, all programs for NMO velocity analysis can be used to do RMO velocity analysis. This technique was applied by Deregowsky (1990). In his paper, Deregowsky used an iterative algorithm in RMO velocity analysis to handle lateral velocity variation. However, this iteration may fail as I will show later.

4.2 Velocity Estimates for Constant Migration Velocity

For arbitrary migration velocity, the residual moveout representation (4.12) will be too complex to yield a quantitative formula for velocity estimates. In contrast, when migration velocity is a constant, the residual moveout representation is a more explicit function of the velocity error, which allows velocity estimates to be done without iteration. Furthermore, prestack migration with a constant velocity is most efficient.

In addition to the normal moveout formula (4.4), I will compute residual moveout by the formula (4.23) and (4.24) for several special cases. These results are similar to normal moveout, except that velocity estimates by the former are insensitive to reflector dips.

4.2.1 Constant medium velocity

Dipping reflector

Suppose that the medium velocity is a constant v , and the reflector dip is θ . In this case,

$$t^2(y, h) = 4y^2 \sin^2 \theta / v^2 + 4h^2 \cos^2 \theta / v^2. \quad (4.28)$$

Therefore,

$$\left[t \frac{\partial^2 t}{\partial h^2} \right]_{h=0} = 4 \cos^2 \theta / v^2, \quad (4.29)$$

$$\left. \frac{\partial t}{\partial y} \right|_{h=0} = 2 \sin \theta / v. \quad (4.30)$$

From equation (4.23), I obtain

$$\left. \frac{d^2 z^2}{dh^2} \right|_{h=0} = 2(c^2/v^2 - 1). \quad (4.31)$$

$$z^2(h) = z^2(0) + (c^2/v^2 - 1) h^2 + O(h^4). \quad (4.32)$$

or

$$\tau_m^2(h) = \tau_m^2(0) + (1/v^2 - 1/c^2) 4h^2 + O(h^4). \quad (4.33)$$

Equation (4.33) shows that for a constant medium velocity and a dipping reflector, the residual moveout is independent of the reflector dip and the RMO velocity equals the medium velocity.

Diffraction from a scattering point

Suppose that the medium velocity is a constant v , and a scatterer is located at the point (x^*, z^*) . In this case,

$$t(y, h) = \left[\sqrt{(y - h - x^*)^2 + (z^*)^2} + \sqrt{(y + h - x^*)^2 + (z^*)^2} \right] / v, \quad (4.34)$$

$$\left[t \frac{\partial^2 t}{\partial h^2} \right]_{h=0} = \frac{4}{v^2} \frac{(z^*)^2}{(y - x^*)^2 + (z^*)^2}, \quad (4.35)$$

$$\left(\frac{\partial t}{\partial y} \right)_{h=0}^2 = \frac{4}{v^2} \frac{(y - x^*)^2}{(y - x^*)^2 + (z^*)^2}. \quad (4.36)$$

Therefore, from equation (4.23),

$$\left. \frac{d^2 z^2}{dh^2} \right|_{h=0} = 2(c^2/v^2 - 1); \quad (4.37)$$

$$z^2(h) = z^2(0) + (c^2/v^2 - 1) h^2 + O(h^4), \quad (4.38)$$

or

$$\tau_m^2(h) = \tau_m^2(0) + (1/v^2 - 1/c^2) 4h^2 + O(h^4). \quad (4.39)$$

Again, equation (4.39) shows that the residual moveout is independent of the lateral offset from the point scatterer and the RMO velocity equals the medium velocity, when the medium velocity is a constant.

4.2.2 Laterally invariant medium velocity

Horizontal reflector

Suppose that the medium velocity is a laterally invariant function $v(z)$, and the

reflector is horizontal with depth z^* . In this case,

$$t^2(y, h) = t^2(y, 0) + 4h^2/v_{rms}^2(z^*) + O(h^4), \quad (4.40)$$

Where v_{rms} is the rms velocity of v . Differentiation of the above equation yields

$$\left[t \frac{\partial^2 t}{\partial h^2} \right]_{h=0} = 4/v_{rms}^2(z^*), \quad (4.41)$$

$$\left. \frac{\partial t}{\partial y} \right|_{h=0} = 0. \quad (4.42)$$

Therefore, from equation (4.23),

$$\left. \frac{d^2 z^2}{dh^2} \right|_{h=0} = \frac{2c^2}{v_{rms}^2(z^*)} - 2. \quad (4.43)$$

$$z^2(h) = z^2(0) + \left(\frac{c^2}{v_{rms}^2(z^*)} - 1 \right) h^2 + O(h^4), \quad (4.44)$$

and

$$v_{rms}(z(0)) = v_{rms}(z^*). \quad (4.45)$$

Notice that $z(0) \neq z^*$. That is, in depth migration, the imaged depth is inconsistent with the desired point at which the rms velocity is determined from the residual moveout. However, if let

$$\tau^* = 2 \int_0^{z^*} \frac{ds}{v(s)}, \quad (4.46)$$

then

$$\tau_m^2(h) = \tau_m^2(0) + \left(\frac{1}{v_{rms}^2(\tau^*)} - \frac{1}{c^2} \right) 4h^2 + O(h^4), \quad (4.47)$$

and $\tau_m(0) = \tau^*$. Therefore, time migration can give us the correct location at which

the rms velocity is determined by the residual moveout.

Equation (4.47) shows that when the true velocity is laterally invariant, the RMO velocity equals rms velocity at the migration time.

Dipping reflector

Suppose that the medium velocity is a laterally invariant function $v(\tau)$, and the reflector angle is θ . In this case,

$$t(y, 0) = \int_0^{\tau^*} (1 - p^2 v^2(\sigma))^{-1/2} d\sigma, \quad (4.48)$$

$$\left. \frac{\partial^2 t}{\partial h^2} \right|_{h=0} = \frac{4}{\int_0^{\tau^*} v^2 (1 - p^2 v^2)^{-3/2} d\sigma}, \quad (4.49)$$

$$\left. \frac{\partial t}{\partial y} \right|_{h=0} = 2p, \quad (4.50)$$

where τ^* is the vertical time at the reflection point and p is the horizontal slowness, i.e.,

$$p = \frac{\sin \theta}{v(\tau^*)}. \quad (4.51)$$

Therefore,

$$\left[t \frac{\partial^2 t}{\partial h^2} + \left(\frac{\partial t}{\partial y} \right)^2 \right]_{h=0} = 4 \frac{\int_0^{\tau^*} (1 - p^2 v^2)^{-3/2} d\sigma}{\int_0^{\tau^*} v^2 (1 - p^2 v^2)^{-3/2} d\sigma}, \quad (4.52)$$

and

$$v_{rmo}^2 = \frac{\int_0^{\tau^*} v^2(\sigma) (1 - p^2 v^2(\sigma))^{-3/2} d\sigma}{\int_0^{\tau^*} (1 - p^2 v^2(\sigma))^{-3/2} d\sigma}. \quad (4.53)$$

Notice that v_{rmo} does not equal the rms velocity v_2 that is defined by

$$v_2^2(\tau^*) = \frac{1}{\tau^*} \int_0^{\tau^*} v^2(\sigma) d\sigma. \quad (4.54)$$

In fact, from the Taylor series expansion, derived in Appendix A,

$$v_{rmo}^2 = v_2^2 + \frac{3}{2}(v_4^4 - v_2^4)p^2 + O(p^4), \quad (4.55)$$

where

$$v_4^4 = \frac{1}{\tau^*} \int_0^{\tau^*} v^4(s) ds. \quad (4.56)$$

v_4 is always greater than v_2 and they are equal only if $v(z)$ is a constant. Moreover, v_{rmo} is close to $v_2(\tau^*)$ for small p or a small gradient of $v(z)$. When v_{rmo} is estimated from the residual moveout formula (4.27), v_{rmo} is measured at the migration time, $\tau_m(0)$ instead of τ^* . That means, it is desirable if

$$v_{rmo} \approx v_2(\tau_m(0)). \quad (4.57)$$

Fortunately, v_{rmo} is a better approximation of $v_2(\tau_m(0))$ than $v_2(\tau^*)$. In fact, if v_2^2 is a linear function of migration time, one can prove that v_{rmo} is exactly equal to $v_2(\tau_m(0))$ for the choice $c = v_2(0)$, no matter what dip the reflector.

It is concluded that for choosing $c = v_2(0)$, the RMO velocity is a good approximation of the rms velocity at the migration time as long as the velocity varies mildly.

4.2.3 Higher residual terms

The residual moveout is hyperbola-like only for small offset. In fact, offsets should not be too small so that resolution in velocity analysis is not too low (See Chapter 3). Therefore, one should consider the error due to truncating the higher residual terms. This work is partially implemented in Mathematica.

Using the rule of differentiation for a compound function in equation (4.12) and

setting c constant, the fourth order derivative of z with respect to h satisfies

$$\begin{aligned} \left[\frac{\partial(\rho_s + \rho_r)}{\partial z} \frac{d^4 z}{dh^4} \right]_{h=0} &= c \left[\frac{\partial^4 t}{\partial h^4} + 3 \frac{d^2 y}{dh^2} \frac{\partial^3 t}{\partial h^2 \partial y} \right]_{h=0} - \frac{\partial^4(\rho_s + \rho_r)}{\partial h^4} \Big|_{h=0} \\ &- 6 \left[\frac{d^2 z}{dh^2} \frac{\partial^3(\rho_s + \rho_r)}{\partial h^2 \partial z} \right]_{h=0} - 3 \left[\frac{d^2 y}{dh^2} \frac{\partial^3(\rho_s + \rho_r)}{\partial h^2 \partial y} \right]_{h=0}. \end{aligned} \quad (4.58)$$

For a constant velocity v and a dipping reflector with angle θ , equation (4.58) is simplified to

$$\frac{d^4 \tau_m^2}{dh^4} \Big|_{h=0} = - \frac{24(1/v^2 - 1/c^2) \sin^2 2\theta}{(z^*)^2}, \quad (4.59)$$

where τ_m is the migration time and z^* is the depth of the reflection point. Therefore, from (4.59) and (4.33), a more accurate expression for the residual moveout is

$$\tau_m^2(h) = \tau_m^2(0) + 4 \left(\frac{1}{v^2} - \frac{1}{c^2} \right) h^2 - \frac{(1/v^2 - 1/c^2) \sin^2 2\theta}{(z^*)^2} h^4 + O(h^6). \quad (4.60)$$

For a constant velocity v and a scattering point at (x^*, z^*) , again

$$\frac{d^4 \tau_m^2}{dh^4} \Big|_{h=0} = - \frac{24(1/v^2 - 1/c^2) \sin^2 2\theta}{(z^*)^2}, \quad (4.61)$$

except that now

$$\theta = \arctan \frac{y - x^*}{z^*}.$$

In comparison, for the unmigrated data, the higher residual term is

$$\frac{\partial^4 t^2}{\partial h^4} \Big|_{h=0} = \frac{24 \sin^2 2\theta \cos^2 \theta}{v^2 (z^*)^2}. \quad (4.62)$$

Equations (4.59) and (4.61) show that when the true velocity is a constant, small higher-residual terms of moveout are obtained for a close background velocity, small offset, small ratio of offset to the imaged depth, and the dipping angle that is near 0

or 90 degrees.

For a laterally invariant velocity and a horizontal reflector at the zero-offset time t_0 ,

$$\left. \frac{d^4 \tau_m^2}{dh^4} \right|_{h=0} = \frac{24(v_2^4 - v_4^4)}{t_0^2 v_2^8}, \quad (4.63)$$

where v_2 and v_4 are defined in equations (4.53) and (4.55).

Equation (4.63) shows that when the medium velocity is laterally invariant, a small higher-residual term is obtained for small gradient of the velocity.

4.2.4 Lateral velocity anomaly

RMO velocity can be estimated from residual moveout. If the medium velocity is laterally invariant, the RMO velocity approximates the rms velocity. However, when the velocity has a lateral anomaly, this conclusion fails so that one cannot calculate directly the interval velocity from the RMO velocity by Dix equation or other algorithms. Now I will develop an equation to solve for the laterally variant interval velocity. This equation holds for a small lateral velocity variation and a horizontal reflector. For horizontal reflectors, the RMO velocity is the same as the asymptotic stacking velocity in normal moveout.

Suppose the true slowness $w(x, z)$ can be written as

$$w(x, z) = \bar{w}(z) (1 + \alpha(x, z)), \quad (4.64)$$

where $\bar{w}(z)$ is a reference slowness and $\alpha(x, z)$ is a small perturbation. The slowness $w(x, z)$ and horizontal reflectors will generate a two-way travelttime map, $t(y, h)$. After prestack migration with an initial migration velocity, a RMO velocity (therefore,

slowness) can be calculated from residual moveouts. Let $w_s(x, z)$ denote this RMO slowness, $\bar{w}_s(z)$ denote the average of $w_s(x, z)$ over the x -direction; then an equation for $\alpha(x, z)$ is obtained in Appendix B:

$$\frac{w_s^2(x, z)}{\bar{w}_s^2(z)} - 1 = \frac{2}{\bar{t}_0} \int_0^z \left[\frac{\partial^2 \alpha}{\partial x^2} \left(\frac{\int_\sigma^z \bar{v} ds}{\bar{v}_s(z)} \right)^2 + \alpha(x, \sigma) \left(1 + \frac{\bar{v}^2(\sigma)}{\bar{v}_s^2(z)} \right) \right] \frac{d\sigma}{\bar{v}(\sigma)}, \quad (4.65)$$

where $\bar{v}_s = 1/\bar{w}_s$, \bar{t}_0 is the two-way zero-offset time, and \bar{v} be the solution of

$$\bar{v}_s^2(z) = \frac{1}{\bar{t}_0} \int_0^z \bar{v}(\sigma) d\sigma. \quad (4.66)$$

When α and \bar{w} are independent of depth, the result in equation (4.65) is the same as that of Lynn and Claerbout (1982). Equation (4.65) shows that the second derivative of α determines the anomaly of the RMO velocity; the anomaly of the RMO velocity at a depth results from the anomaly of the interval velocity above this depth. Furthermore, $\int_\sigma^z \bar{v} ds$ increases as σ decreases, so the anomaly of the interval velocity near the surface has the largest effect.

Applying the Fourier transform, with respect to x , to equation (4.65), I obtain

$$g(k_x, z) = \frac{2}{\bar{t}_0} \int_0^z \alpha(k_x, \sigma) \left[-k_x^2 \left(\frac{\int_\sigma^z \bar{v} ds}{\bar{v}_s(z)} \right)^2 + 1 + \frac{\bar{v}^2(\sigma)}{\bar{v}_s^2(z)} \right] \frac{d\sigma}{\bar{v}(\sigma)}, \quad (4.67)$$

where k_x is the wavenumber and g is the Fourier transform of $w_s^2/\bar{w}_s^2 - 1$. Equation (4.67) is a First-kind Volterra integral equation that is ill-posed. Therefore, the recursive algorithm for equation (4.67) is unstable. To obtain a stable solution, one may apply the damped least-squares method to this equation.

4.3 Some Extensions

The previous discussion in this chapter focused on the common offset case in 2-D. Now I will discuss some extensions to common shot and 3-D situations.

4.3.1 Common shot case

Although common offset migration and common shot migration are stated in different forms, they should represent the same physical process and produce the same images, if the same multichannel data are used. Particularly, for a constant migration, the residual moveout in common shot should have the same representation as equation (4.27)

$$\tau_m^2(h) = \tau_m^2(0) + \left(\frac{1}{v_{rmo}^2} - \frac{1}{c^2} \right) 4h^2 + O(h^4). \quad (4.68)$$

The problem is: for common shot, migrated data in a CIG are sorted according to shot positions instead of the shot-receiver offsets. That means, one does not directly know what offset values the migrated traces in a CIG have, unless the reflector is horizontal. In order to overcome this difficulty, the offsets must be calculated for the traces in a CIG. Lee and Zhang (1991) proposed a formula to implement this work. However, Lee and Zhang's formula requires information of reflector dip and holds for small-dip reflector and constant medium velocity. Therefore, the application of this formula is limited.

Another way to calculate the offset is by using the Kirchhoff integral. In the Kirchhoff summation, one calculate two inversion outputs which have two different amplitudes. One is the original amplitude; the other is the original one multiplied by offset h . Thus, the ratio of the amplitudes of the two outputs will give the offset

value at the specular source-receiver position. In this way, a mapping between shot position and offset is obtained. The same technique was used to determine the angle of reflection in Kirchhoff inversion. [See Bleistein et al. (1987).]

4.3.2 3-D case

Consider the 3-D common offset case. The imaging equations are stated in equations (2.22) and (2.23). The Taylor series of the imaged depth is expanded into

$$z^2(\mathbf{h}) = z^2(\mathbf{0}) + \frac{1}{2} \frac{\partial^2 z^2}{\partial h_1^2} \Big|_{\mathbf{h}=\mathbf{0}} h_1^2 + \frac{\partial^2 z^2}{\partial h_1 \partial h_2} \Big|_{\mathbf{h}=\mathbf{0}} h_1 h_2 + \frac{1}{2} \frac{\partial^2 z^2}{\partial h_2^2} \Big|_{\mathbf{h}=\mathbf{0}} h_2^2 + O(|\mathbf{h}|^4), \quad (4.69)$$

where the odd-order derivatives are eliminated because of the symmetric condition

$$z(\mathbf{h}) = z(-\mathbf{h}). \quad (4.70)$$

Similar to the derivation of equation (4.12), each of the second derivatives in equation (4.69) will individually satisfy

$$\left[\left(\frac{\partial \tau_s}{\partial z} + \frac{\partial \tau_r}{\partial z} \right) \frac{\partial^2 z}{\partial h_i \partial h_j} \right]_{\mathbf{h}=\mathbf{0}} = \frac{\partial^2 t}{\partial h_i \partial h_j} \Big|_{\mathbf{h}=\mathbf{0}} - \left[\frac{\partial^2 \tau_s}{\partial h_i \partial h_j} + \frac{\partial^2 \tau_r}{\partial h_i \partial h_j} \right]_{\mathbf{h}=\mathbf{0}}, \quad (4.71)$$

where the indices, i and j , take the integer value 1 or 2. Equation (4.71) is valid for any velocity distribution and an arbitrary reflector.

Suppose that the migration velocity is a constant, c ; then

$$\tau_s = \sqrt{z^2 + |\mathbf{x} - \mathbf{y} + \mathbf{h}|^2}/c, \quad \tau_r = \sqrt{z^2 + |\mathbf{x} - \mathbf{y} - \mathbf{h}|^2}/c. \quad (4.72)$$

So,

$$\left[\frac{\partial \tau_s}{\partial z} + \frac{\partial \tau_r}{\partial z} \right]_{\mathbf{h}=\mathbf{0}} = \frac{2z}{c\rho}, \quad (4.73)$$

and

$$\left[\frac{\partial^2 \tau_s}{\partial h_i \partial h_j} + \frac{\partial^2 \tau_r}{\partial h_i \partial h_j} \right]_{\mathbf{h}=\mathbf{0}} = \frac{2}{c\rho} \delta_{ij} - \frac{2(x_i - y_i)(x_j - y_j)}{c\rho^3}, \quad (4.74)$$

where δ_{ij} is the Kronecker delta (1 if $i = j$ and 0 if $i \neq j$), and

$$\rho = \sqrt{z^2 + |\mathbf{x} - \mathbf{y}|^2}. \quad (4.75)$$

Let $t_0(\mathbf{y}) = t(\mathbf{y}, \mathbf{0})$; then

$$\rho = \frac{c}{2} t_0, \quad (4.76)$$

and

$$\frac{(y_i - x_i)}{\rho} = \frac{c}{2} \frac{\partial t_0}{\partial y_i}, \quad i = 1, 2. \quad (4.77)$$

By using relations (4.76) and (4.77), equation (4.74) is rewritten as

$$\left[\frac{\partial^2 \tau_s}{\partial h_i \partial h_j} + \frac{\partial^2 \tau_r}{\partial h_i \partial h_j} \right]_{\mathbf{h}=\mathbf{0}} = \frac{4}{c^2 t_0} \delta_{ij} - \frac{1}{t_0} \frac{\partial t_0}{\partial y_i} \frac{\partial t_0}{\partial y_j}. \quad (4.78)$$

Furthermore, suppose that the medium velocity is a constant, v . If $c = v$, all the derivatives in the left of equation (4.71) will be zero because the imaged depth z is independent of offset for a correct migration velocity. That is,

$$\left. \frac{\partial^2 t}{\partial h_i \partial h_j} \right|_{\mathbf{h}=\mathbf{0}} = \left[\frac{\partial^2 \tau_s}{\partial h_i \partial h_j} + \frac{\partial^2 \tau_r}{\partial h_i \partial h_j} \right]_{\mathbf{h}=\mathbf{0}, c=v}. \quad (4.79)$$

Using equation (4.78), and setting $c = v$, I rewrite equation (4.79) as

$$\left. \frac{\partial^2 t}{\partial h_i \partial h_j} \right|_{\mathbf{h}=\mathbf{\emptyset}} = \frac{4}{v^2 t_0} \delta_{ij} - \frac{1}{t_0} \frac{\partial t_0}{\partial y_i} \frac{\partial t_0}{\partial y_j}. \quad (4.80)$$

Since t is just the recorded travelttime, the above expression must be independent of the migration velocity c . Subtracting equation (4.78) from equation (4.80), yields

$$\left. \frac{\partial^2 t}{\partial h_i \partial h_j} \right|_{\mathbf{h}=\mathbf{\emptyset}} - \left[\left. \frac{\partial^2 \tau_s}{\partial h_i \partial h_j} + \frac{\partial^2 \tau_r}{\partial h_i \partial h_j} \right]_{\mathbf{h}=\mathbf{\emptyset}} = \frac{4}{t_0} \left(\frac{1}{v^2} - \frac{1}{c^2} \right) \delta_{ij}. \quad (4.81)$$

Substituting equations (4.81), (4.73) and (4.76) into (4.71), and using

$$\left. \frac{\partial^2 z^2}{\partial h_i \partial h_j} \right|_{\mathbf{h}=\mathbf{\emptyset}} = \left[2z \frac{\partial^2 z}{\partial h_i \partial h_j} \right]_{\mathbf{h}=\mathbf{\emptyset}}, \quad (4.82)$$

I obtain

$$\left. \frac{\partial^2 z^2}{\partial h_i \partial h_j} \right|_{\mathbf{h}=\mathbf{\emptyset}} = 2 \left(\frac{c^2}{v^2} - 1 \right) \delta_{ij}. \quad (4.83)$$

Finally, by using the above equation, the residual moveout (4.69) is simplified to

$$z^2(\mathbf{h}) = z^2(\mathbf{\emptyset}) + \left(\frac{c^2}{v^2} - 1 \right) |\mathbf{h}|^2 + O(|\mathbf{h}|^4), \quad (4.84)$$

or

$$\tau_m^2(\mathbf{h}) = \tau_m^2(\mathbf{\emptyset}) + 4 \left(\frac{1}{v^2} - \frac{1}{c^2} \right) |\mathbf{h}|^2 + O(|\mathbf{h}|^4), \quad (4.85)$$

where τ_m is the migration time. Equation (4.85) holds for constant velocities and an arbitrary reflector, and shows that the residual term in the the migrated data is independent of both reflector dip and the source-receiver azimuth.

When the medium velocity is varied, one should replace v by v_{rms} , although this statement is precise. Therefore, equation (4.85) offers a theoretical basis for

estimating the rms velocity from the 3-D residual moveout.

4.4 Limitation on a Two-layer Model

Now, I design a test to show the limitation of a velocity estimation that uses the hyperbolic residual moveout (4.27). The model, shown in Figure 4.2 consists of two constant velocity layers, v_1 and v_2 , and two flat interfaces. The ray starts vertically from the midpoint y on the surface and intersects the first interface with the angle α_1 from the normal; then transmits to the second layer with the angle β_1 from the normal and intersects vertically the second interface at the reflection point (x, z) .

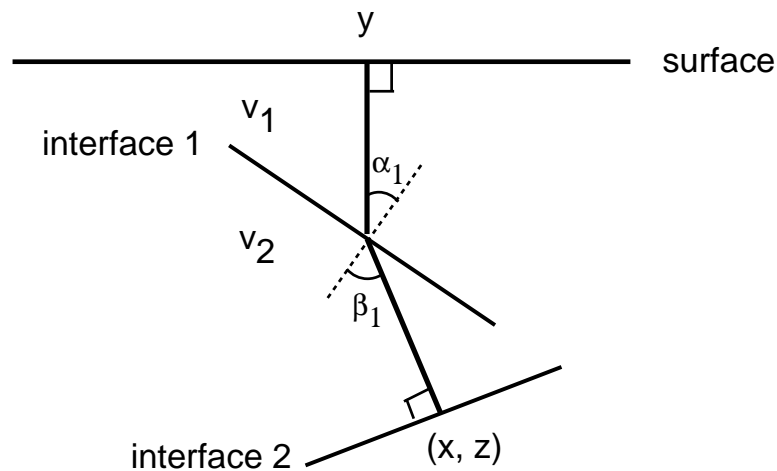


FIG. 4.2. Two-layer model.

The ray is perpendicular to the surface, so $\partial t/\partial y = 0$. This fact means $v_{rmo} = v_{nmo}$. From Hubral and Krey's formula (1980), I have

$$v_{rmo}^2 = v_{nmo}^2 = \frac{1}{\Delta t_1 + \Delta t_2} \left(v_1^2 \Delta t_1 + v_2^2 \Delta t_2 \frac{\cos^2 \alpha_1}{\cos^2 \beta_1} \right), \quad (4.86)$$

where Δt_1 and Δt_2 are the one-way time along the ray in the first and the second

layer respectively. Suppose that v_2 is 10 percent greater than v_1 , i.e., $v_2 = 1.1v_1$. Also, I specify, $\Delta t_1 = \Delta t_2$ and $\alpha_1 = 60^\circ$. After calculations, I find $\beta_1 = 72.3^\circ$ and $v_{rmo} = 1.46v_1$. From the Dix equation, the estimated interval velocity is obtained,

$$\tilde{v}_2 = 1.81v_1 = 1.64v_2.$$

That is, if the error in initial velocity is 10 percent, then the error in the updated velocity may be magnified to 64 percent.

This example shows the limitation of velocity analysis by hyperbolic residual moveout: when the velocity distribution contains a strong lateral variation, velocity updating may fail to improve the initial value.

4.5 Computer Implementation

Parallel to NMO velocity analysis, one can use a semblance and velocity scans to do RMO velocity analysis. Therefore, the program for RMO velocity analysis is similar to the existing program for NMO velocity analysis, except in the residual term. A suggested data processing technique based on this approach is composed of prestack migration with a constant velocity, velocity analysis, residual moveout, stacking, and poststack residual migration.

To demonstrate the processing procedure, I applied this method to synthetic seismograms computed for a subsurface model in which velocity increases linearly with depth z , according to $v(z) = 1.5 + 0.8z$ km/s. The model, shown in Figure 4.3, consists of five reflectors, each with a dipping and horizontal segment. Dips for the dipping segments range from 30 to 90 degrees in 15-degree increments. The seismograms contain 10 offsets, ranging from 100 to 1900 meters in 200 meter increments. Because of the dipping reflectors and the depth dependent velocity, the RMO velocity in

equation (4.53) and the rms velocity are not the same but close each other. The relative error between the two, shown in Figure 4.4, increases with depth and dip. The maximal error is about two percent.

After prestack migration with the constant velocity, $c = 1.5$ km/s, the dipping events are not migrated to correct positions, except for the 30-degree dip (see Figure 4.5). One of the common image gathers is plotted in Figure 4.6. Because the migration velocity is lower than the true velocity, the imaged depths increase with offset. The velocity spectra for this CIG is shown in Figure 4.7. Unlike the velocity spectrums in NMO, the velocity peaks here are insensitive to reflector dips and, therefore, single-valued. The RMO velocities are picked from these peaks. After residual moveout correction, all events in the CIG are corrected to horizontal ones, shown in Figure 4.8. Stacking the data, having residual moveout corrected, yields a result shown in Figure 4.9, which is equivalent to the zero-offset migration with the constant velocity c . By using the interval velocity converted from the RMO velocity, poststack residual migration gives the corrected reflector positions shown in Figure 4.10. Notice that the bottom of the vertical event is not migrated completely, which is due to some errors involved in the RMO velocity estimates and that these errors are enlarged in the conversion of the interval velocity. For example, the relative error between the true interval velocity at 2 seconds and the computed one is 4 percent.

4.6 Summary

Under the assumption of small offset, residual moveout representations are obtained in this chapter. Using these relationships, one can estimate directly the medium velocities from residual moveouts without iteration when the medium has weak lateral velocity variations. For complex structures, this approach does not offer

an accurate enough velocity estimation, even with iteration.

For converted waves or anisotropic media, seismic data are not symmetric to offset generally. Thus, the residual moveout representations will be dip-dependent and, therefore, be less useful in velocity estimation. However, these representations may allow us to make a qualitative analysis of the relationship between the imaged depth and migration velocity.

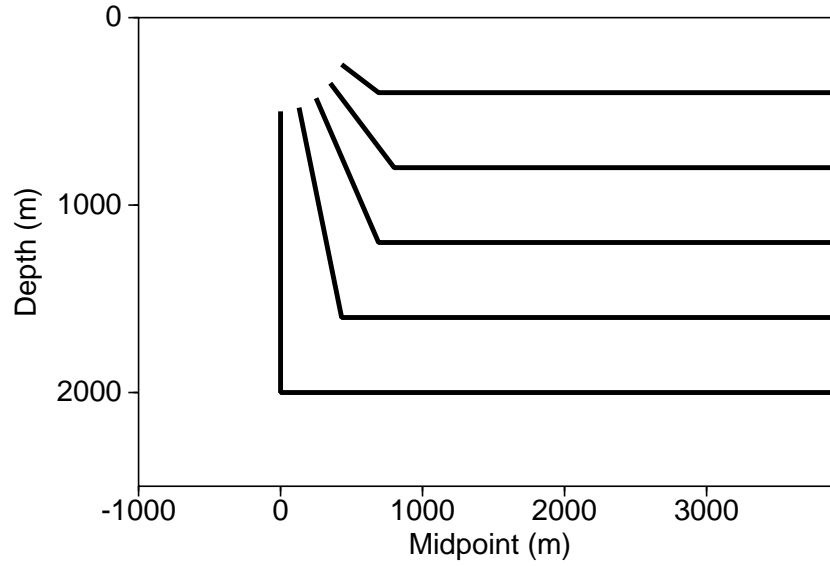


FIG. 4.3. Subsurface model used to generate synthetic seismic traces.

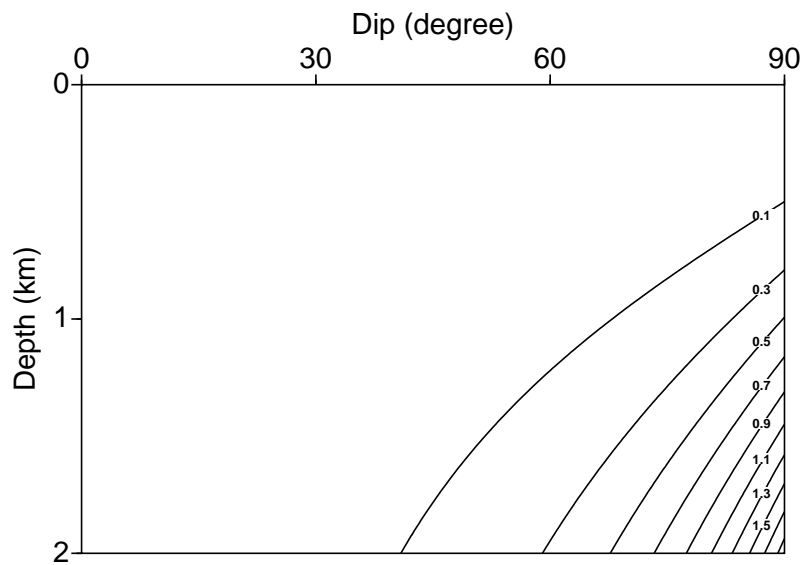


FIG. 4.4. The contours of relative error between the RMO velocity and the rms velocity. The error increases with depth and dip.

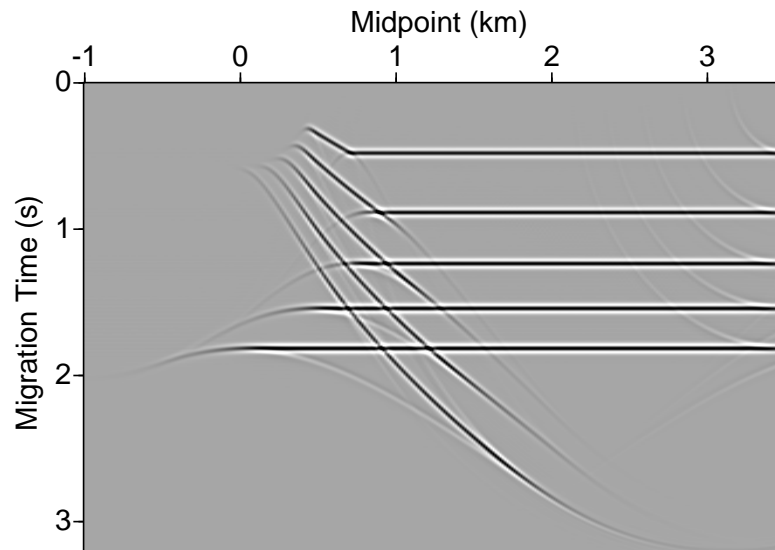


FIG. 4.5. The migrated data with the constant velocity. The offset is 100 meters.

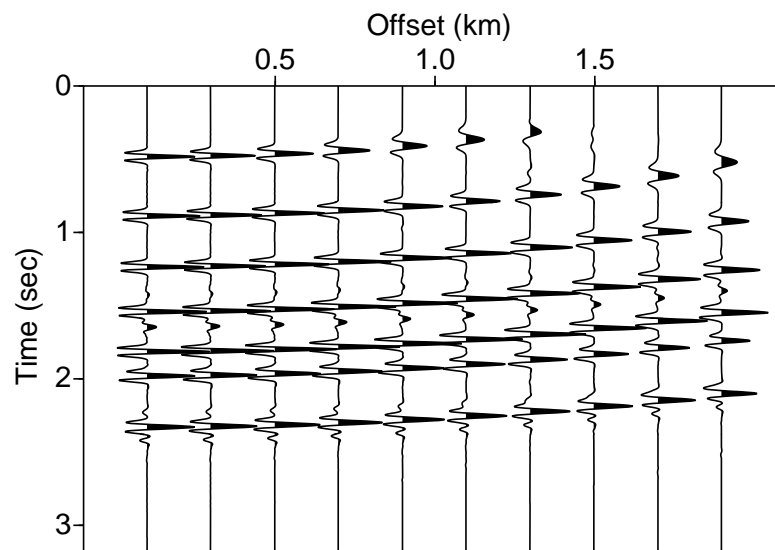


FIG. 4.6. One of the common image gathers from data migrated with the constant velocity. The traces are located at 1.4 km in Figure 4.5.

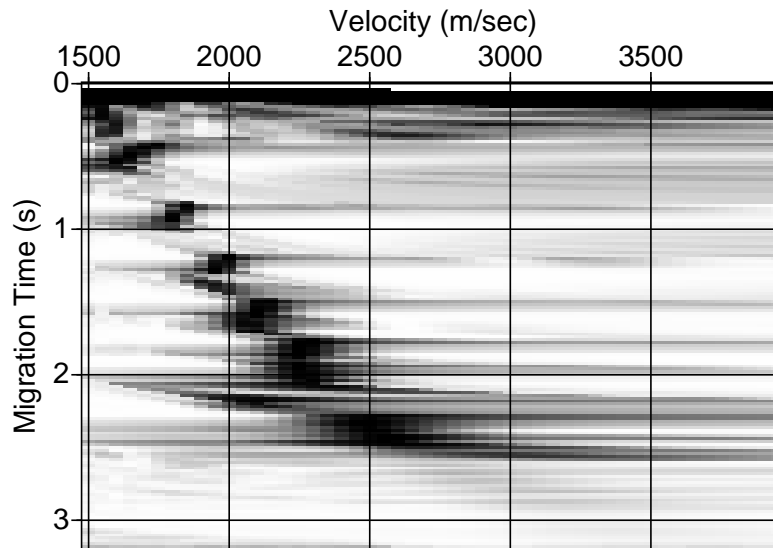


FIG. 4.7. Velocity spectrum for the CIG in Figure 4.6.

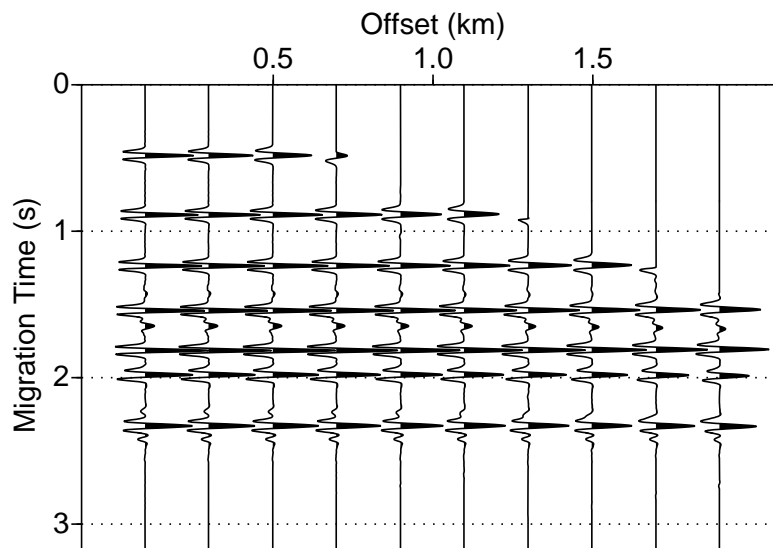


FIG. 4.8. Residual moveout correction for the CIG in Figure 4.6.

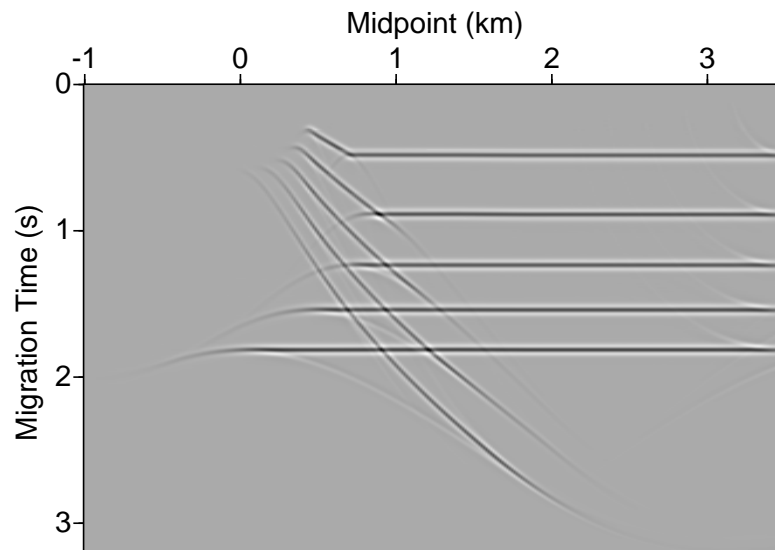


FIG. 4.9. Stacking for the partially migrated data of the ten offsets.

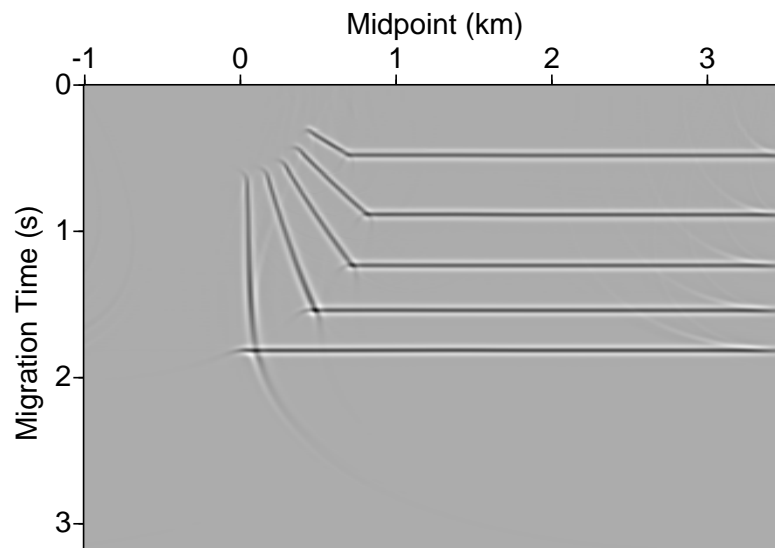


FIG. 4.10. Poststack residual time migration of the data in Figure 4.7.

Chapter 5

ITERATIVE APPROACH: METHODOLOGY

When velocity has lateral variations, the residual moveout cannot be approximated by a hyperbola and the RMO velocity may be quite different from the rms velocity. Therefore, the velocity estimate cannot be simply done by using residual moveout correction. In this situation, iterative approaches are required to update velocity. However, iterative formulas used in conventional approaches are derived under assumptions such as small offset, small dip, and lateral velocity homogeneity. Although iteration generally is helpful in obtaining a more accurate velocity, too coarse an approximate formula for updating velocity not only increases the number of iteration steps but may result in divergence. Thus, applications of those approaches to velocity analysis are limited when there are complex structures. In Chapter 4, I have shown a counter example for iteration when the hyperbolic residual moveout method is applied to a simple two-layer model.

In this chapter, I will present an iterative approach to migration velocity analysis. Using perturbation theory, I derive a formula for updating velocity from residual moveout by computing a derivative function of imaged depths with respect to velocity. Significantly here, this formula has no limitations on offset, reflector dip, or velocity distribution if the velocity perturbation is sufficiently small. Therefore, this formula gives a general description of the relationship between residual moveout and residual velocity. Based on this formula, I revise the residual-curvature-analysis method for velocity estimation. In addition, this formula provides both sensitivity and error

estimation for migration-based velocity analysis, which is helpful in explaining the reliability of the estimated velocity. Moreover, this velocity analysis approach can be extended to the 3-D case and to converted waves.

5.1 Velocity Analysis by Perturbation

In Chapter 4, the residual moveout representations are obtained under the small-offset assumption. However, this assumption is violated for a lateral velocity variation. Here, I will derive a residual moveout representation by using a perturbation. This idea is suggested by tomography approaches to velocity estimation. Under the assumption of small velocity perturbation, there is a linear relationship between the residual traveltimes and the residual velocity. In the tomographic approach, raypaths are required to construct the equation system for velocity estimation. However, ray-path construction seems more difficult in reflection tomography than in refraction tomography. Raypaths strongly depend on the reflector position (especially the slope) in reflection tomography and the reflector cannot be determined accurately. In contrast, here I will use the stationary-phase principle to determine raypaths, without requiring knowledge of an accurate reflector position. My derivation will be based on the imaging equations in Chapter 2.

5.1.1 Mathematical derivation

Consider the 2-D common offset case. All notations have the same meaning as those in Chapter 2. The imaging equations (2.8) and (2.9) are repeated

$$\tau_s(x_s, \mathbf{x}) + \tau_r(\mathbf{x}, x_r) = t(y, h), \quad (5.1)$$

$$\frac{\partial \tau_s}{\partial y} + \frac{\partial \tau_r}{\partial y} = \frac{\partial t}{\partial y}. \quad (5.2)$$

At a common image gather, the imaged depth z can be determined as a function of h . If the migration velocity equals the true velocity, then the imaged depth z will be independent of offset h ; otherwise—for incorrect velocity— z varies with offset h . Consequently, the imaged depths in CIGs provide information on velocity distribution.

Equations (5.1) and (5.2) display a general relationship between the imaged depth and migration velocity. However, this equation system is nonlinear, making it very difficult to directly solve for velocity. Here, I use a mathematical tool—perturbation—to linearize this equation system.

Suppose that the velocity distribution v is characterized by a parameter or a family of parameters, λ ,

$$v = v(\mathbf{x}; \lambda).$$

For example, when $v(\mathbf{x}; \lambda) = v_0 + ax + bz$, λ is any set of one to three parameters chosen from v_0 , a , and b . Thus, the problem of velocity estimation becomes parameter estimation. To simplify the derivation, I suppose that λ is just a single parameter at first.

For a fixed image location x , I differentiate equation (5.1) with respect to λ . Noticing that y and z are functions of λ ; then

$$\left[\frac{\partial \tau_s}{\partial y} + \frac{\partial \tau_r}{\partial y} \right] \frac{dy}{d\lambda} + \left[\frac{\partial \tau_s}{\partial \lambda} + \frac{\partial \tau_r}{\partial \lambda} \right] + \left[\frac{\partial \tau_s}{\partial z} + \frac{\partial \tau_r}{\partial z} \right] \frac{dz}{d\lambda} = \frac{\partial t}{\partial y} \frac{dy}{d\lambda}. \quad (5.3)$$

By using equation (5.2), the first term of the left side in equation (5.3) is balanced

by the right-hand term. Therefore,

$$\left[\frac{\partial \tau_s}{\partial z} + \frac{\partial \tau_r}{\partial z} \right] \frac{dz}{d\lambda} = -\frac{\partial \tau_s}{\partial \lambda} - \frac{\partial \tau_r}{\partial \lambda}. \quad (5.4)$$

Let θ_s or θ_r be the angle between the raypath from the source or the receiver, and the vertical at \mathbf{x} ; then

$$\frac{\partial \tau_s}{\partial z} = \frac{\cos \theta_s}{v(\mathbf{x}; \lambda)}, \quad \frac{\partial \tau_r}{\partial z} = \frac{\cos \theta_r}{v(\mathbf{x}; \lambda)}, \quad (5.5)$$

By using the above equation, equation (5.4) is rewritten as

$$\frac{\cos \theta_s + \cos \theta_r}{v(\mathbf{x}; \lambda)} \frac{dz}{d\lambda} = -\frac{\partial \tau_s}{\partial \lambda} - \frac{\partial \tau_r}{\partial \lambda}. \quad (5.6)$$

Thus the derivative of imaged depth with respect to λ is found,

$$\frac{dz}{d\lambda} = g(x, h), \quad (5.7)$$

where

$$g(x, h) = - \left[\frac{\partial \tau_s}{\partial \lambda} + \frac{\partial \tau_r}{\partial \lambda} \right] \frac{v(\mathbf{x}; \lambda)}{\cos \theta_s + \cos \theta_r}. \quad (5.8)$$

The function g characterizes the relationship between the imaged depth and the migration velocity in a general medium context. The computation of this function will result in a new migration velocity analysis method, compared to conventional ones based on hyperbolic residual moveout.

Suppose that the true parameter is λ^* and the true reflection depth is z^* . If there is a small perturbation $\delta\lambda = \lambda^* - \lambda$ between the true parameter and the parameter

used in migration, then the imaged depth will have a corresponding perturbation

$$\delta z(x, h) \equiv z^* - z(x, h) \approx \frac{dz}{d\lambda} \delta \lambda.$$

By using equation (5.7), a linearized equation is set for $\delta \lambda$:

$$\delta z = g(x, h) \delta \lambda. \quad (5.9)$$

Equation (5.9) is valid for an arbitrary velocity distribution, arbitrary reflector dips, and any offset, as long as the velocity perturbation is sufficiently small, which is significantly different from the limited result of conventional RCA.

Remark. When the velocity distribution is constant in layers, one can take λ as velocity v itself, in the target layer. In this situation,

$$\frac{\partial \tau_s}{\partial \lambda} + \frac{\partial \tau_r}{\partial \lambda} = -\frac{t_s + t_r}{v}, \quad (5.10)$$

where t_s (or t_r) is a partial travelt ime of τ_s (or τ_r) within this layer. Thus, the derivative function g is simplified to

$$g(x, h) = \frac{t_s + t_r}{\cos \theta_s + \cos \theta_r}. \quad (5.11)$$

This typical result was obtained by Lafond and Levander (1993).

When the velocity distribution is characterized by multiple parameters, $\hat{\lambda} = (\lambda_1, \lambda_2, \dots, \lambda_n)^T$, the imaged-depth perturbation will depend on the perturbations of all these parameters. Therefore, equation (5.9) will be modified by

$$\delta z(x, h) = \sum_{i=1}^n \frac{\partial z}{\partial \lambda_i} \delta \lambda_i = \sum_{i=1}^n g_i(x, h) \delta \lambda_i, \quad (5.12)$$

where each derivative function is calculated by

$$g_i(x, h) = - \left[\frac{\partial \tau_s}{\partial \lambda_i} + \frac{\partial \tau_r}{\partial \lambda_i} \right] \frac{v(\mathbf{x}; \hat{\lambda})}{\cos \theta_s + \cos \theta_r}. \quad (5.13)$$

If one could solve for $\delta \hat{\lambda}$, the true parameters can be estimated by

$$\hat{\lambda}^* = \hat{\lambda} + \delta \hat{\lambda}. \quad (5.14)$$

Notice that the left side of equation (5.12) involves the true depth z^* that is unknown. Conventional methods deal with this problem by using the concept of the reference depth (Lafond and Levander, 1993) or adding z^* as a new unknown (Stork, 1991). Here, I use a technique to remove z^* directly in equation (5.12). The true depth can be approximately replaced by the corrected imaged depth $z + \delta z$,

$$z^* \approx z(x, h) + \delta z(x, h) = z(x, h) + \sum_{i=1}^n g_i(x, h) \delta \lambda_i. \quad (5.15)$$

The true reflection depth z^* , is independent of offset. Therefore, the corrected imaged-depths from different offsets should be close to each other. Mathematically, this statement means that the covariance of these depths is a minimum. Suppose that there are offsets h_1, h_2, \dots, h_m , and image locations x_1, x_2, \dots, x_K , then

$$z_j^{(k)} + \delta \hat{z}^{(k)} = z_j^{(k)} + \sum_{i=1}^n g_{ij}^{(k)} \delta \lambda_i, \quad (5.16)$$

where

$$z_j^{(k)} = z(x_k, h_j),$$

$$\delta \hat{z}^{(k)} = \delta z(x_k, h_j),$$

$$g_{ij}^{(k)} = g_i(x_k, h_j).$$

I seek $\delta\lambda_i$'s such that the corrected imaged depths have the minimum variance; i.e.,

$$\sum_{k=1}^K \sum_{j=1}^m \left(z_j^{(k)} + \delta z_j^{(k)} - \overline{\hat{z}^{(k)} + \delta \hat{z}^{(k)}} \right)^2 = \min, \quad (5.17)$$

where

$$\hat{z}^{(k)} = (z_1^{(k)}, z_2^{(k)}, \dots, z_m^{(k)})^T,$$

$$\delta \hat{z}^{(k)} = (\delta z_1^{(k)}, \delta z_2^{(k)}, \dots, \delta z_m^{(k)})^T.$$

Here I use the overline to denote the mean value of a vector over the offset index. For example,

$$\overline{\hat{z}^{(k)}} = \frac{1}{m} \sum_{j=1}^m z_j^{(k)}.$$

Introduce the matrix and vector,

$$A^{(k)} \equiv [a_{il}^{(k)}]_{n \times n}, \quad \hat{b}^{(k)} \equiv (b_1^{(k)}, b_2^{(k)}, \dots, b_n^{(k)})^T, \quad (5.18)$$

where

$$a_{il}^{(k)} = \sum_{j=1}^m \left(g_{ij}^{(k)} - \overline{\hat{g}_i^{(k)}} \right) \left(g_{lj}^{(k)} - \overline{\hat{g}_l^{(k)}} \right),$$

$$b_i^{(k)} = \sum_{j=1}^m \left(g_{ij}^{(k)} - \overline{\hat{g}_i^{(k)}} \right) \left(z_j^{(k)} - \overline{\hat{z}^{(k)}} \right),$$

$$\hat{g}_i^{(k)} = (g_{i1}^{(k)}, g_{i2}^{(k)}, \dots, g_{in}^{(k)})^T;$$

then, as shown in Appendix A, the solution of equation (5.17) must satisfy the linear equation,

$$\left[\sum_{k=1}^K A^{(k)} \right] \delta \hat{\lambda} = - \sum_{k=1}^K \hat{b}^{(k)}. \quad (5.19)$$

Specifically, if there is only one parameter to be determined, i.e $n = 1$, then equation (5.19) will have an explicit solution

$$\delta\lambda = -\frac{\sum_{k=1}^K \sum_{j=1}^m (g_j^{(k)} - \hat{g}^{(k)}) (z_j^{(k)} - \hat{z}^{(k)})}{\sum_{k=1}^K \sum_{j=1}^m (g_j^{(k)} - \hat{g}^{(k)})^2}, \quad (5.20)$$

where

$$g_j^{(k)} = g(x_k, h_j),$$

and

$$\hat{g}^{(k)} = (g_1^{(k)}, g_2^{(k)}, \dots, g_m^{(k)})^T.$$

If the corrected imaged-depths are not close enough to each other, I implement iteration to obtain more accurate parameters. The iteration stops where the variance (5.17) achieves a given sufficiently small value.

5.1.2 Computational techniques

Calculation of the derivative function

The function $g(x, h)$ involves the derivatives of traveltimes with respect to the parameter λ . In the eikonal equation,

$$\left(\frac{\partial\tau}{\partial x}\right)^2 + \left(\frac{\partial\tau}{\partial z}\right)^2 = \frac{1}{v^2(\mathbf{x}; \lambda)}, \quad (5.21)$$

Differentiating here with respect λ yields

$$\frac{\partial\mu}{\partial x} \frac{\partial\tau}{\partial x} + \frac{\partial\mu}{\partial z} \frac{\partial\tau}{\partial z} = \frac{1}{2} \frac{\partial}{\partial\lambda} \left(\frac{1}{v^2(\mathbf{x}; \lambda)} \right), \quad (5.22)$$

where

$$\mu = \frac{\partial \tau}{\partial \lambda}.$$

The integral solution of equation (5.22) is

$$\mu = \int_L \frac{\partial}{\partial \lambda} \left(\frac{1}{v(\mathbf{x}; \lambda)} \right) dL, \quad (5.23)$$

where L is the raypath from the source (or receiver) to the image point \mathbf{x} .

For each source or receiver, $\partial \tau / \partial \lambda$ can be determined from equation (5.22) or (5.23). Therefore, given an image point \mathbf{x} and a specular source-receiver pair x_s and x_r , one can calculate g from formula (5.8). However, there is not an explicit formula to represent the specular source-receiver pair from the image point for a complex medium. To solve this problem, here, I use the Kirchhoff integral to calculate g . In the Kirchhoff summation, I calculate two migration outputs which have the same phase but different amplitudes. One uses the original amplitude; the other one uses the original amplitude multiplied by the quantity g . Thus, the ratio of the amplitudes of these two outputs will evaluate g at the specular source-receiver position according to the stationary-phase principle, without requiring knowledge of the specular source-receiver pair. This technique is the same as was used to determine the angle of reflection in Kirchhoff inversion (Bleistein et al., 1987).

This approach to calculate the derivative function g depends the S/N ratio in seismic data and the power of stationary phase method. The stationary phase method works well if the dominant seismic wavenumber is large compared to the length scale of the velocity variation. In this sense, a smooth velocity is required in Kirchhoff migration for velocity estimates by perturbation.

Parameterization of velocity distribution

Although equation (5.19) holds for any velocity distribution, the solution will be underdetermined and unstable if too many unknown parameters are involved. Consequently, it is essential to characterize the velocity distribution by choosing appropriate parameters. Conventionally, one assumes that a velocity model consists of the construction of the macro-model (constant velocities and velocity interfaces). The interfaces divide the whole model into a number of blocks (shown in Figure 5.1). Here, I replace constant velocity in one block by a linear function that is characterized

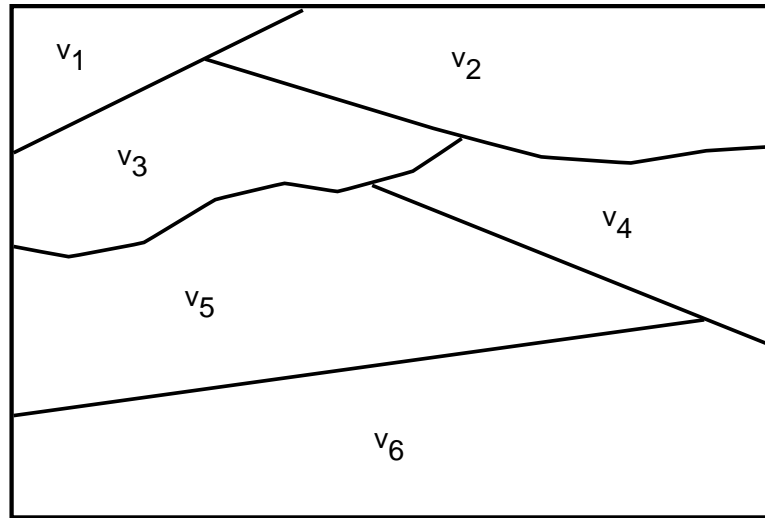


FIG. 5.1. Macro model.

by three parameters:

$$\lambda_1 + \lambda_2(z - z_0) + \lambda_3(x - x_0),$$

where (x_0, z_0) is a reference point. Thus, the velocity distribution is written in a form

$$v(x, z) = v_0(x, z) + \lambda_1 + \lambda_2(z - z_0) + \lambda_3(x - x_0), \quad (5.24)$$

where v_0 is a background velocity.

An imaged depth only depends on the velocity above it, except for turning rays. Therefore, use of a recursive algorithm (layer stripping) is possible to determine velocity in an individual block. I start from the block nearest surface. For example, I choose the top left block in Figure 5.1. In each block, iteration is used to calculate velocity parameters. Given an initial guess for λ_i 's, common-offset depth migration is implemented to obtain imaged depths and $g_i(x, h)$ in equation (5.13) for common image gathers. Equation (5.19) will give a correction of the parameters. Then by using the updated parameters as an initial guess, I correct the velocity again until convergence is achieved. After velocity analysis in one block, I migrate data with the corrected velocity, and pick the velocity interface from the imaged structure. When I finish determining velocity and velocity interface in one block, I will repeat the same procedure to the next block that is located below the finished block.

An alternative choice of perturbation approach

Perturbation methods are used to gain good linear approximations to nonlinear functions. However, in some cases, one should exercise caution in choosing the variable in which an expression is perturbed. For example, in acoustic media, z^2 as a linear function of the square of migration velocity is more likely than z as a linear function of the migration velocity itself. For example, for a constant velocity medium and a horizontal reflector, equation (4.3) shows that z^2 is the exact linear function of the square of migration velocity. Therefore, instead of equation (5.7), I may use

$$\frac{dz^2}{d\lambda} = g(x, h), \quad (5.25)$$

where

$$g(x, h) = - \left[\frac{\partial \tau_s}{\partial \lambda} + \frac{\partial \tau_r}{\partial \lambda} \right] \frac{2z v(\mathbf{x}; \lambda)}{\cos \theta_s + \cos \theta_r}. \quad (5.26)$$

Thus, the linear parameterization of velocity distribution may be chosen as

$$v^2(x, z) = v_0^2(x, z) + \lambda_1 + \lambda_2(z - z_0) + \lambda_3(x - x_0). \quad (5.27)$$

5.2 Sensitivity of Migration Velocity Analysis

Velocity analysis by prestack migration uses the difference between the imaged depths from different offsets to correct the velocities, which is represented by equation (5.19). If the variance defined by equation (5.17) is zero, one can conclude that the velocity is correct. However, it is impractical to obtain an exact zero variance. There are many factors against achieving this goal: noise in the input data, non-acoustic properties, inaccurate description of velocity distribution, and so on. Even while an apparent zero variance is obtained, the actual one may not be zero because of the errors involved in picking the imaged depths. The imaged depths in the variance are picked on the migration output, so that the position error in imaged depths is controlled by the resolution of the migration output, which, in turn, depends on wavelength, among other things.

Quantitatively, the matrices in equation (5.19) that depend on the functions g_i , can be used to describe the sensitivity of the velocity error $\delta\lambda$, to the variance of residual-moveout error. Here, I will derive analytical representations for the simplest cases.

Suppose that the velocity $v(x, z)$ consists of a constant background velocity v_0 and a perturbation that is a linear function of depth in one block. Moreover, I assume that the upper boundary of the block is a horizontal line, $z = d$, and the reflector,

located at $z = z^*$, is the bottom boundary of this block. The velocity function can be represented by

$$v(x, z) = v_0 + \alpha(\lambda_1 + \lambda_2(z - z_0)), \quad (5.28)$$

where $\alpha = 0$ for $z < d$, $\alpha = 1$ for $z > d$, and z_0 is a reference depth (not necessarily in the block). A sketch for this block is shown in Figure 5.2.

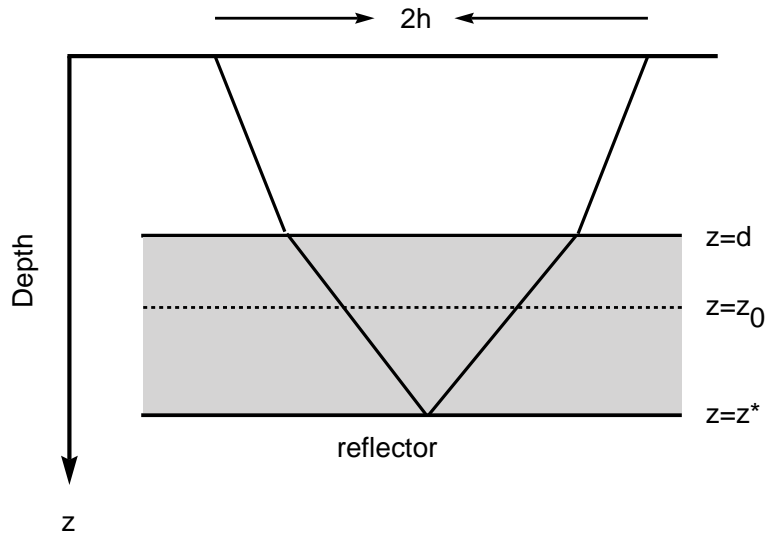


FIG. 5.2. Layer model. The gray shading denotes the target layer for velocity analysis.

The initial guesses are set to

$$\lambda_1 = \lambda_2 = 0.$$

As shown in Appendix B, I obtain the following representations for the g_i 's that is defined in equation (5.13),

$$g_1(x, h) = \frac{h^2 + z^2}{z^2} \frac{z - d}{v_0}, \quad (5.29)$$

$$g_2(x, h) = \frac{h^2 + z^2}{z^2} \frac{(z - z_0)^2 - (d - z_0)^2}{2v_0}. \quad (5.30)$$

From the above two equations, I have

$$g_2(x, h) = \frac{(z - z_0)^2 - (d - z_0)^2}{2(z - d)} g_1(x, h). \quad (5.31)$$

This means that the coefficients in equation (5.12) are proportional for all image locations and all offsets, so that I cannot solve for λ_1 and λ_2 independently. Thus, I have the following conclusion: *The parameters λ_1 and λ_2 cannot be determined simultaneously if only one reflector segment is used in the velocity-analysis process.*

This conclusion shows that one should avoid solving for λ_1 and λ_2 at the same time unless well-separated reflector segments are used for velocity analysis.

If the parameter λ_2 is given (i.e., $\delta\lambda_2 = 0$), then equation (5.13) is simplified to

$$\delta z(x, h) = \left(\frac{h^2}{z^2} + 1 \right) \frac{z - d}{v_0} \delta\lambda_1. \quad (5.32)$$

When $\delta\lambda_1$ is small, $z(x, h) \approx z^*$. Therefore, for given two offsets h_2 and h_1 ($h_2 > h_1$), the difference of imaged depths from these two offsets is

$$z(x, h_2) - z(x, h_1) = \left[\frac{h_2^2}{(z^*)^2} - \frac{h_1^2}{(z^*)^2} \right] \frac{z^* - d}{v_0} \delta\lambda_1. \quad (5.33)$$

i.e.,

$$\Delta z \equiv z(x, h_2) - z(x, h_1) = \frac{(h_2^2 - h_1^2)(z^* - d)}{(z^*)^2 v_0} \delta\lambda_1. \quad (5.34)$$

The above equation shows that *the error in λ_1 is proportional to the thickness of the block layer*, which is consistent with results of equation (3.34). When there is a thin layer, the velocity estimation for this layer is often unreliable, so I conclude that

migration-based velocity analysis cannot handle thin layers.

Similarly, if the parameter λ_1 is given (i.e., $\delta\lambda_1 = 0$), then

$$\Delta z = \frac{(h_2^2 - h_1^2)(z^* - d)(z^* + d - 2z_0)}{2(z^*)^2 v_0} \delta\lambda_2. \quad (5.35)$$

The above equation shows that *the error in λ_2 is determined not only by the thickness of the block layer but by $(z^* + d)/2 - z_0$ —the difference between the central depth of the block layer and the reference depth z_0 .*

There are two kinds of depth errors: δz and Δz . δz is the difference between the true depth and the imaged depth, which reflects migration error due to the velocity error; Δz is the difference between the imaged depths from different offsets, i.e., residual moveout. The ratio of these two depth errors is given by equations (5.32) and (5.34),

$$\gamma \equiv \frac{\delta z}{\Delta z} = \frac{h^2 + (z^*)^2}{(h_2^2 - h_1^2)}. \quad (5.36)$$

The ratio γ indicates the depth error of migration due to the error in migration residual moveout. The bigger the value of γ is, the larger error of migration may result from the error in residual moveout. Equation (5.36) shows that increasing the ratio of offset to reflection depth will be helpful to reduce the migration error, although this is a well-known statement.

For a general case, it is difficult to obtain analytical representations for the g_i 's. However, I can calculate the g_i 's numerically, as described above, and use these values to estimate the velocity error. Specifically, if there is only one parameter, equation (5.20) gives a direct error estimation,

$$|\delta\lambda| \leq \left[\frac{\sum_{k=1}^K \sum_{j=1}^m (\hat{z}_j^{(k)} - \overline{\hat{z}}^{(k)})^2}{\sum_{k=1}^K \sum_{j=1}^m (g_j^{(k)} - \overline{g}^{(k)})^2} \right]^{1/2}, \quad (5.37)$$

where the Cauchy-Schwarz inequality has been used.

5.3 Simple-Iteration Approach

The velocity inversion essentially is a nonlinear process. By using the perturbation method, I obtain a linear equation (5.19) to update velocity iteratively. The efficiency of this linearized iteration depends on the initial guess of velocity and the stability of velocity updating. Actually, these problems, initial guess and stability, are related. The less the stability is, the better the initial guess that is required. The stability of equation (5.21) depends on the noise level in the data and the complexity of structures in the overburden. For example, equation (5.21) trends unstable when a thin layer structure exists. In order to obtain a convergent solution, I use the so-called simple-iteration algorithm described below as a supplement to the perturbation method. Here, I assume that the velocity is constant layered.

If I view residual moveout Δz , as a function of migration velocity v , then the true velocity v^* is the one for which

$$\Delta z(v) = 0. \quad (5.38)$$

Also, from equation (5.34), I conclude that Δz is positive when $v > v^*$ and Δz is negative when $v < v^*$. Based on this fact, one proceeds with the following simple-iteration algorithm to determine the true layer velocity as follows:

- (1) Choose two initial velocities v_1 and v_2 such that

$$\Delta z(v_1) < 0, \quad \Delta z(v_2) > 0.$$

(2) Compute a new velocity by weighting the initial velocities as follows:

$$v_3 = v_1 \frac{\Delta z(v_2)}{\Delta z(v_2) - \Delta z(v_1)} + v_2 \frac{\Delta z(v_1)}{\Delta z(v_1) - \Delta z(v_2)}. \quad (5.39)$$

(3) If $\Delta z(v_3) = 0$ (or smaller than a given precision), the iteration will stop, with v_3 the desired velocity. If $\Delta z(v_3) > 0$, v_3 replaces v_2 in step (1); otherwise, if $\Delta z(v_3) < 0$, v_3 replaces v_1 and go to step (2).

During the iteration, the true velocity v^* always is between v_1 and v_2 , and the deviation of v_1 and v_2 decreases monotonically, so the convergence of this iteration is guaranteed as long as the model is well approximated by constant-velocity layers.

5.4 Some Extensions

It is straightforward that formulas in section 4.1 are extended from the common offset case to the common shot case, because I did not use the special properties of common offset gather in my derivation. The only difference is, traces in a CIG for the common shot case are organized in accordance with shot positions instead of the source-receiver offsets. Now I will discuss the extension of these results to the 3-D case and converted waves.

5.4.1 3-D case

The derivation in 3-D is the same as that in section 4.1.1, except for replacing location scalars by location vectors and replacing offset scalars by offset vectors. For example, equation (5.8) will be rewritten as

$$g(\mathbf{x}, \mathbf{h}) = - \left[\frac{\partial \tau_s}{\partial \lambda} + \frac{\partial \tau_r}{\partial \lambda} \right] \frac{v(\mathbf{x}; \lambda)}{\cos \theta_s + \cos \theta_r}. \quad (5.40)$$

Here $\mathbf{x} = (x_1, x_2)$, and $\mathbf{h} = (h_1, h_2)$ have the same meaning as that in section 2.3. In addition, the linear velocity function will depend on four parameters:

$$v(x, z) = v_0(x, z) + \lambda_1 + \lambda_2(z - z_0) + \lambda_3(x_1 - x_{10}) + \lambda_4(x_2 - x_{20}), \quad (5.41)$$

where v_0 is a background velocity and (x_{10}, x_{20}, z_0) is a reference point.

Theoretically, the velocity analysis approach in this chapter will be suitable both to the 2-D and to the 3-D case. However, this approach certainly encounters more computational difficulties in the 3-D case. Two issues are (i) how one measures residual moveout efficiently, and (ii) how one picks the imaged interface in the migrated data for building a macro model. Hopefully, these difficulties will be solved with development of 3-D data processing and visualization.

5.4.2 Converted waves

With some work, the formulas in Section 4.1 can be extended to converted waves. In each expression, there is no difference between imaging equations for converted waves and those for non-converted waves. When the perturbation method is applied to converted waves, one should use different parameters to characterize P-wave velocity v_P , and S-wave velocity v_S , even within a same block.

With no loss generality, I consider a P-S refraction and show how to modify some formulas in section 4.1.1. Suppose that λ is a parameter to describe v_S ; then, compared to equation (5.5), I have

$$\frac{\partial \tau_s}{\partial z} = \frac{\cos \theta_s}{v_P(\mathbf{x}; \lambda)}, \quad \frac{\partial \tau_r}{\partial z} = \frac{\cos \theta_r}{v_S(\mathbf{x}; \lambda)}. \quad (5.42)$$

Therefore, compared to (5.8), the function g has a modified representation,

$$g(x, h) = -\frac{\partial\tau_r}{\partial\lambda} \left[\frac{\cos\theta_s}{v_P(\mathbf{x}; \lambda)} + \frac{\cos\theta_r}{v_S(\mathbf{x}; \lambda)} \right]^{-1}. \quad (5.43)$$

Here I use the fact that

$$\frac{\partial\tau_s}{\partial\lambda} = 0.$$

Parallel to equation (5.23), I have

$$\frac{\partial\tau_r}{\partial\lambda} = \int_L \frac{\partial}{\partial\lambda} \left(\frac{1}{v_S(\mathbf{x}; \lambda)} \right) dL, \quad (5.44)$$

where L is the raypath from the receiver to the image point \mathbf{x} .

5.5 Summary

Perturbation methods are general approaches to solving nonlinear mathematical problems. Based on perturbation methods and the imaging equations, I derived a relationship between residual moveout and residual velocity that has no limitations on reflector dip, offset or velocity distribution. The proposed algorithm estimates the update in velocity by computing a derivative function of imaged depths with respect to velocity in a general background medium context. This formula is more accurate than conventional formulas based on hyperbolic residual moveout when the medium has strongly lateral velocity variations. From this point I have revised the conventional RCA approaches. With a proper modification, the formulation here is also suitable to the 3-D case, converted waves, and even anisotropic media. However, for anisotropic media, one requires more parameters to describe a velocity distribution, so the equation corresponding to (5.19) will be underdetermined if only one compo-

ment of residual moveout is used. In any case, the methodology here provides a basis for developing computational techniques of velocity analysis in anisotropic media.

Chapter 6

ITERATIVE APPROACH: COMPUTER IMPLEMENTATION

To demonstrate the effectiveness and the efficiency of the velocity analysis techniques in Chapter 5, I present some numerical examples for common-offset experiments. The experiments include synthetic data, physical-tank data, and Marmousi data. For these experiments, I use the Kirchhoff integral to implement prestack depth migration (Liu, 1993). The layer-stripping procedure for velocity analysis can be stated as follows:

- begin from the first block
 1. estimate velocity parameters iteratively
 - (a) migrate with an initial guess of velocity;
 - (b) sort the migrated data into common image gathers;
 - (c) measure imaged depths and evaluate the derivative function;
 - (d) update velocity by using the perturbation formula;
 2. image velocity interface by using corrected velocity
- repeat step 1 and 2 for next block

When velocity and velocity gradients are estimated simultaneously in one block, the iteration tends to be unstable, as explained in the previous chapter. To overcome this difficulty, it is preferable to estimate velocity first. This estimation will yield an

averaged velocity and give a better initial guess for the velocity distribution in this block.

6.1 Synthetic Data

The first example is synthetic data generated by the Kirchhoff integral. The velocity model shown in Figure 6.1 consists of six blocks. The velocity function in each block is constant or linear. Synthetic seismic traces are generated from this model, with five offsets ranging from 100 meters to 900 meters. Two of the common offset gathers are shown in Figure 6.2.

The velocity analysis process is outlined as follows:

In the first layer, the initial guess of velocity is 1500 m/s, with an error of 30 percent. Structural images are distorted in the migrated data using this erroneous velocity, shown in Figure 6.3. Two common image gathers of the migrated data also indicate that the initial guess is incorrect, shown in Figure 6.4. The imaged depths are measured at these two image locations for velocity updating. After two iterations, the corrected velocity is 2004 m/s, while the true value is 2000 m/s.

In the second layer, there are two parameters used in the velocity distribution: a constant velocity and a vertical constant gradient. The initial guess takes 2004 m/s that is the estimated velocity in the first layer. Four common image gathers of the migrated data, shown in Figure 6.5 indicate that the first layer velocity in the initial guess is correct, but the deeper layer velocities are not. The imaged depths are measured at these four image locations for velocity updating. If this initial velocity is directly used to estimate the velocity constant and vertical gradient, the iteration will be divergent. Therefore, I only estimate the velocity constant in the first step. The updated velocity is 2420 m/s that gives a better approximation to the true

velocity. In the second iteration, the two parameters of velocity function are updated simultaneously. The corrected velocity function is

$$v(z) = 2490 + 1.01(z - 1000) = 1480 + 1.01z \text{ m/s.}$$

The true velocity function is $v(z) = 1500 + 1.0z$ m/s.

In the left third layer, there are three parameters used in velocity distribution. The initial guess is

$$1480 + 1.01z = 2490 + 1.01(z - 1000) \text{ m/s,}$$

which is the estimated velocity in the second layer. Three common image locations are used for updating velocity: 900, 1200 and 1500 m. After one iteration, the corrected velocity is

$$v(x, z) = 2490 + 1.57(z - 1000) - 0.15x = 920 + 1.57z - 0.15x \text{ m/s.}$$

The true velocity is $v(x, z) = 1000 + 1.5z - 0.2x$ m/s. Despite the error in the lateral gradient, the stopping criterion is met since the difference of the imaged depths is apparently zero. Therefore, iteration ceases.

In the right third layer, there are two parameters used in velocity distribution: constant velocity and constant vertical gradient. The initial guess takes

$$1480 + 1.01z = 2490 + 1.01(z - 1000) \text{ m/s,}$$

which is the estimated velocity in the second layer. Three common image locations are used for updating velocity: 2550, 2850 and 3150 m. After one iteration, the

corrected velocity is

$$v(x, z) = 2490 + 1.55(z - 1000) = 940 + 1.55z \text{ m/s.}$$

The true velocity is $v(z) = 1000 + 1.5z$ m/s.

In the fourth layer, the velocity is a constant. The initial guess is $v = 4000$ m/s. Five common image locations are used for updating velocity: 1500, 1800, 1950, 2100 and 2400 m. After two iterations, the corrected velocity is 3534 m/s, while the true velocity is $v = 3500$ m/s.

The final velocity model estimated through velocity analysis is shown in Figure 6.6. Flat residual moveouts at common image gathers, shown in Figure 6.7, indicate correctness of the estimated velocity. With this velocity model, migration is implemented and shown in Figure 6.8 which is close to the migration result with the true velocity, shown in Figure 6.9.

Table 6.1. Test for g_1 . The unit of offset and depth is m/s.

Offset	Imaged depth	Numerical g_1	True g_1
100	370	0.249	0.251
300	360	0.278	0.282
500	330	0.345	0.346
700	290	0.476	0.475
900	210	0.773	0.783

Also, I test the computation of g_1 in the first layer. The numerical g_1 is computed from the ratio of the amplitudes in the Kirchhoff migration outputs. Then I compare the numerical g_1 with the true value calculated in equation (5.29). In this test, $v_0 = 500$ m/s and $d = 0$. The result listed in Table (6.1) shows that the numerical

value of g_1 is accurate for all offsets. This validates the estimation technique based on the stationary phase principle.

6.2 Physical-tank Data

The input data is from a physical experiment on a tank model, provided to us by Marathon Oil Company. The real medium is three-dimensional, but can be approximated to a two-and-half dimensional model. Figure 6.10 shows one measured slice along the in-line direction. The data were 296 shots, each shot with 48 receivers. The shot point spacing is 24.38 m, and the receiver interval is 24.38 m. Five common-offset gathers are used for velocity analysis whose offsets are 268.2, 512.1, 755.9, 999.7, and 1243.6 meters. Two of them are shown in Figure 6.11. The first shot point is at $x = 0$. For each offset, there are 256 shots and receivers. The time sampling interval is 4 ms; the total time is 2 s. The inversion output spans the ranges x from 61 to 6949 m and z from 0 to 3658 m. In this example, the “true” velocities do not exist, since the model is not perfectly two-and-half dimensional. Migration velocities are sought such that residual moveout is minimized; i.e., migration velocities yield the best stacking effect for the migrated data. The property that the model consists of constant-layered velocities allows use of the simple-iteration method in section 5.3 to update velocity. Velocity analysis is done through the fifth layer, and the first four ones are shown in Figure 6.12. The results are as follows:

(1) In the first layer, the iterative values of c_1 are 2438, 3962, 3309, 3570; the measured value is 3581.

(2) In the second layer, the iterative values of c_2 are 3570, 5182, 4779; the measured value is 4801.

(3) In the third layer, the iterative values of c_3 are 4779, 7315, 6681; the mea-

sured value is 6831.

(4) In the fourth layer, the iterative values of c_4 are 6681, 3962, 4869; the measured value is 4801.

(5) In the fifth layer, the iterative values of c_5 are 4869, 9144, 5812, 6234; the measured value is 6066.

After velocity analysis, a velocity model is obtained that consists of constant velocity layers and interfaces, shown in Figure 6.13. The stacked migrated data using this estimated model is shown in Figure 6.14. One can see clearly the steep dip on the third interface, the saw-tooth reflector on the fourth interface and the flat bottom reflector in this figure. In contrast, the poorly stacked migration section, shown in Figure 6.15, is obtained with the measured velocity model shown in Figure 6.10. The structural images are obviously distorted. Although these two velocity models look similar, the migration sections show significant differences. This fact implies that prestack migration is very sensitive to the velocity model and migration velocity analysis is essential for imaging complex structures.

The velocity estimates by the simple-iteration use only one common image gather. In contrast, the perturbation method can use as many CIGs as possible for velocity estimation. Therefore, the perturbation method may give more accurate velocity estimates. Here, using the velocities estimated by the simple-iteration as an initial guess, I correct the velocity model in Figure 6.13 by the perturbation method. The updated velocity is shown Figure 6.16. The stacked migrated data using this velocity model, shown in Figure 6.17 gives slightly better images than the result in Figure 6.14.

6.3 Marmousi Data

The Marmousi data set is generated by using a two-dimensional acoustic finite-difference modeling program. The model contains many reflectors, steep dips, and strong velocity variations both in lateral and vertical directions (with a minimum velocity of 1500 m/s and a maximum velocity of 5500 m/s), shown in Figure 6.18. The data set consists of 240 shots with 96 traces per shot. The initial offset is 200 m; both the shot and the receiver spacings are 25 m. The first shot is at the lateral position 3000 m. Here 19 of common-offset data gathers are used for velocity analysis. The selected offsets range from 200 m to 2000 m with spacing 100 m. The minimum-offset gather is shown in Figure 6.19.

During the velocity analysis process, I assume that the velocity field is a macro model and that the velocity distribution is a linear function in each block. Velocity analysis results surely depend on what kind of migration algorithm is used. There are two commonly used approaches to calculate traveltimes in Kirchhoff migration: finite differencing and ray tracing. Compared to ray tracing, the finite differencing approach is easier to code and more efficient to implement, but fails to correctly image complicated structures when multiple arrivals exist (Geoltrain and Brac, 1993).

Here, the finite differencing is initially used in the migration implementation for velocity analysis in the area where the first arrivals carry the major energy. The estimated velocity model is shown in Figure 6.20. In the central bottom parts, a paraxial ray tracing algorithm is used to implement Kirchhoff migration. In this approach, the traveltimes corresponding to the major energy is chosen when multiple arrivals exist.

Using the Kirchhoff migration algorithm by paraxial ray tracing, velocity analysis is done through the central bottom parts of the Marmousi model. The updated

velocity model, shown in Figure 6.21, consists of 19 blocks. In each block, the velocity distribution is a constant or linear function of the depth. Comparison of the estimated velocity model to the true one at three lateral locations is shown Figure 6.22. One can see that the estimated velocity matches the true model well except for thin layers. In fact, from the sensitivity analysis in Chapter 5, velocities in these thin layers cannot be determined well. The stacked migration section using the velocity model in Figure 6.21 is shown in Figure 6.23. Compared to the migration result using the true velocity model, shown in Figure 6.24, Figure 6.23 gives an acceptable structural image even in the central bottom parts, which indicates the capability of this migration velocity analysis approach for handling complex structures. The subsurfaces are well imaged except for some detailed features in the central bottom parts. Some blurry image in the central bottom parts may be caused from missing high velocity zones. Figure 6.18 shows that the real velocity contains several small high-velocity zones in the central parts. These high-velocity zones do not appear in Figure 6.21 because of the limitations of velocity analysis and the resolution of migration imaging.

Selected common image gathers from migrated data using the estimated model are shown in Figures 6.25, 6.26 and 6.27 which represent the left, central and right parts of the model respectively. Flat residual moveouts in Figures 6.25, 6.27 and the upper part of Figure 6.26 indicate the correctness of the estimated velocity in these areas. The bottom part of Figure 6.26 shows incoherent signals that affect the accuracy of velocity estimation in this particular area. Notice that, at the same common image gathers (see Figure 6.28), migrated data using the true velocity also contain obvious incoherency in residual moveouts, although the stacked section shows a good image. This example demonstrates that for an extremely complex structure

it is very difficult to identify the correct velocity model based on the criterion of kinematic coherence.

6.4 Summary

Imaging complex structures (such as the Marmousi data) requires powerful prestack depth migration algorithms as well as advanced velocity analysis techniques. The perturbation method in this thesis provides a useful tool for updating a velocity model by matching a criterion based on prestack information, which is one of the key elements in velocity model determination (Versteeg, 1994). In order to obtain a more satisfactory velocity analysis result for a complicated model, as Versteeg concluded, one also needs related geologic information as constraints.

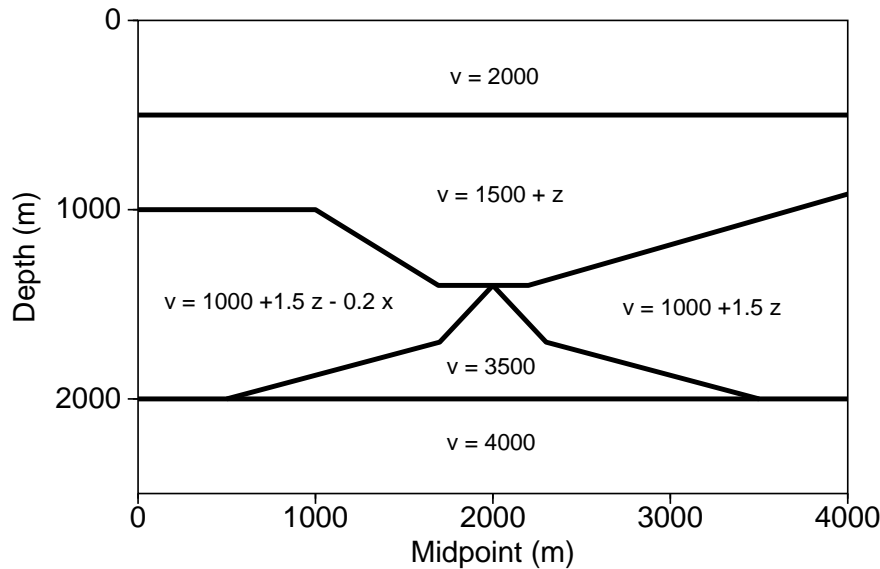


FIG. 6.1. The true velocity model. The velocity unit is m/s.

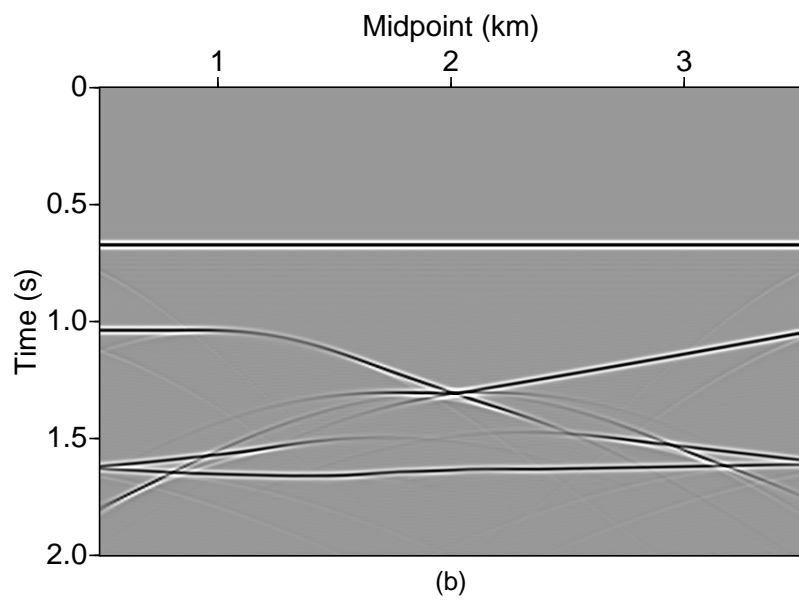
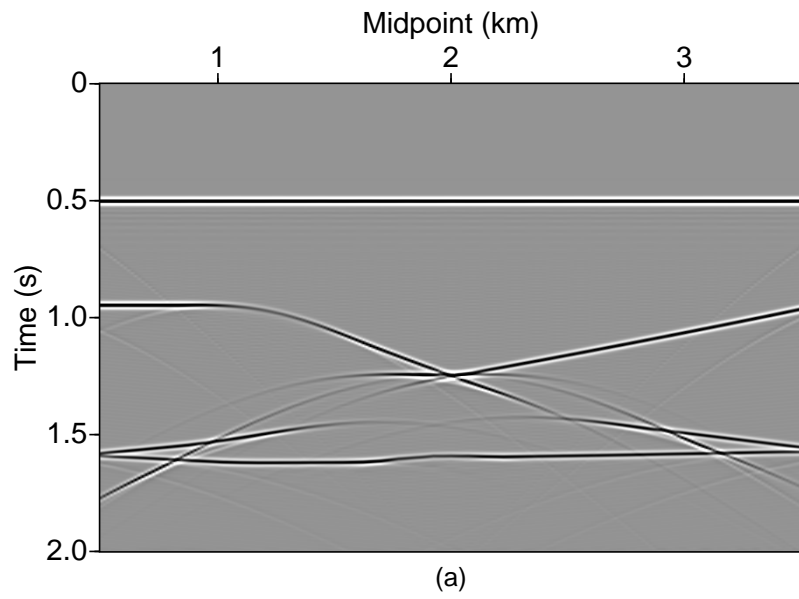


FIG. 6.2. Synthetic data: (a) with offset of 100 meters and (b) with offset of 900 meters.

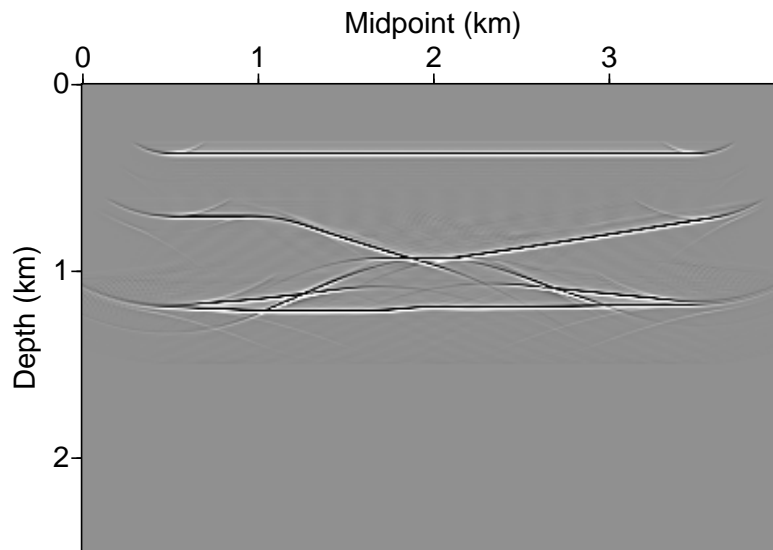


FIG. 6.3. Prestack migration with the initial constant velocity. The offset is 100 meters.

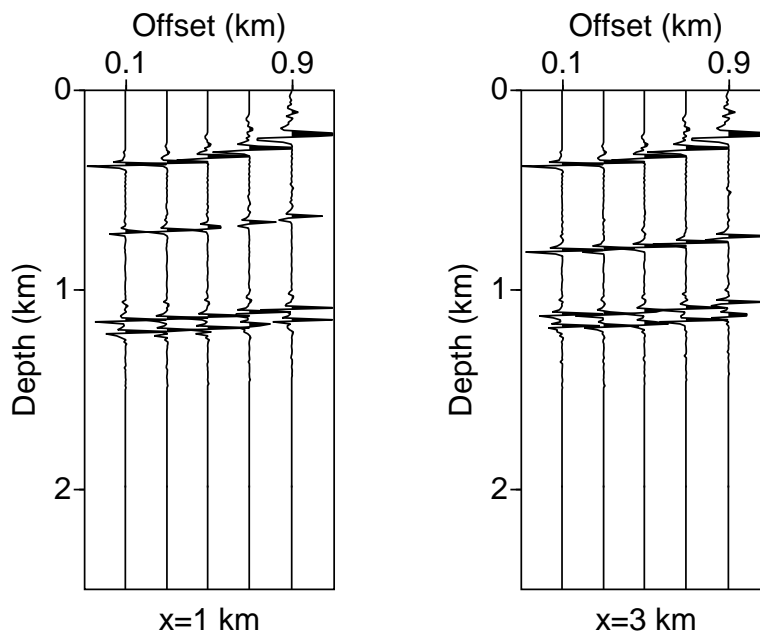


FIG. 6.4. Two common-image gathers from the migrated data with the initial velocity.

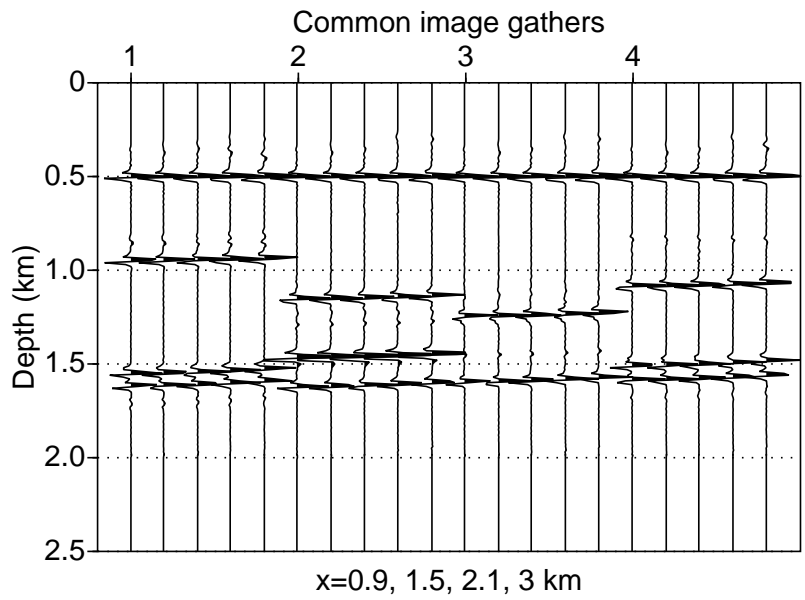


FIG. 6.5. Four common-image gathers from the migrated data with the initial velocity. The numbers 1, 2, 3, etc, correspond to outputs of different CIGs.

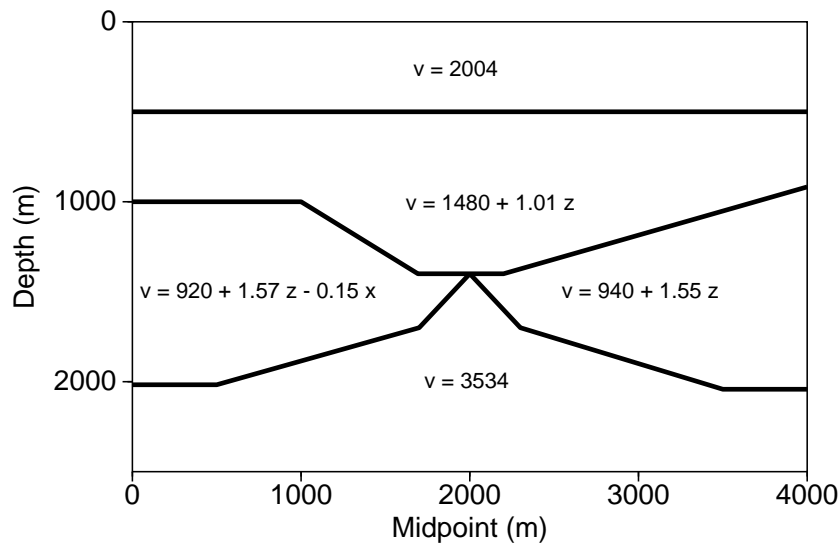


FIG. 6.6. Final estimated model from velocity analysis.

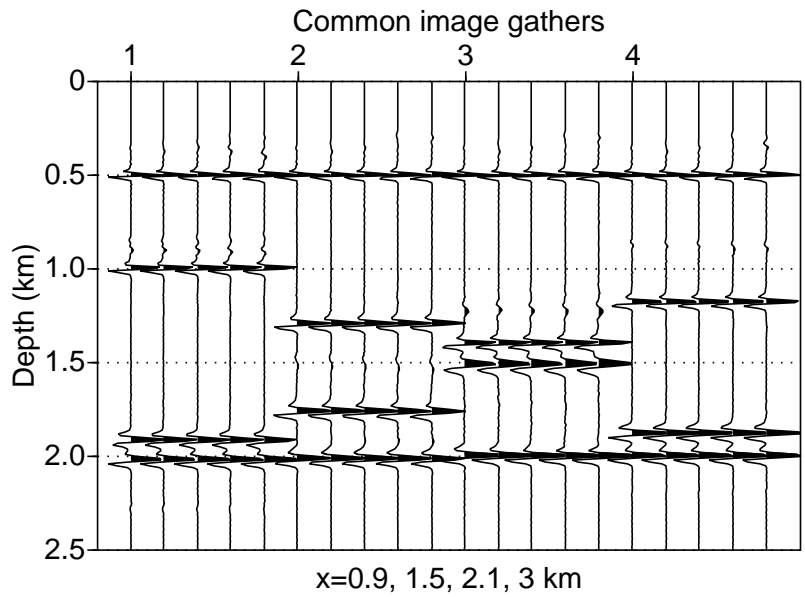


FIG. 6.7. Common image gathers from the migrated data with the velocity in Figure 5.6.

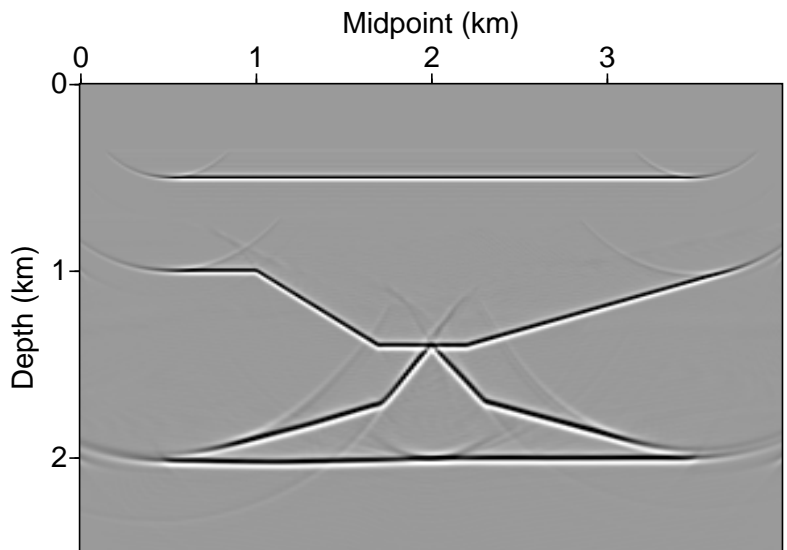


FIG. 6.8. Migration with the estimated velocity model in Figure 6.6.

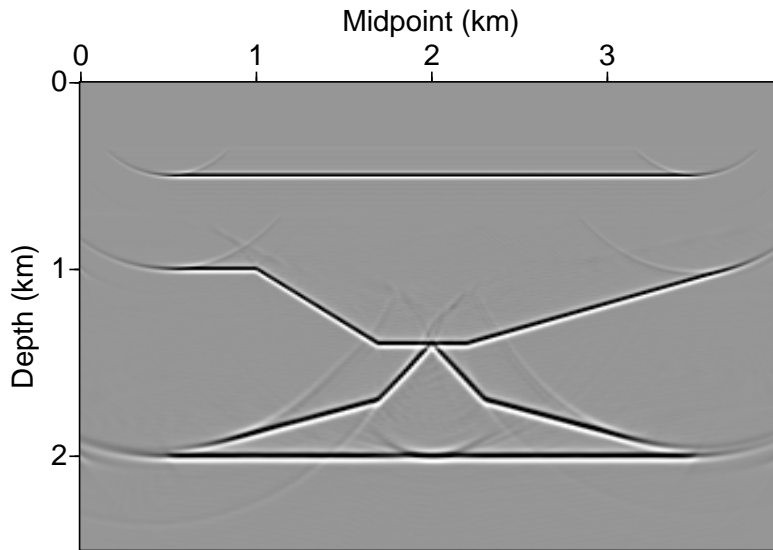


FIG. 6.9. Migration with true velocity model in Figure 6.1.

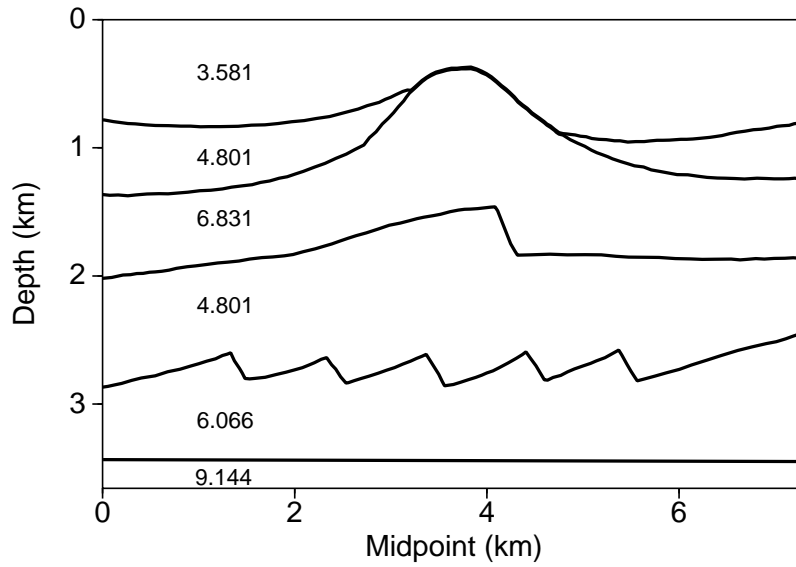


FIG. 6.10. Measured velocity model.

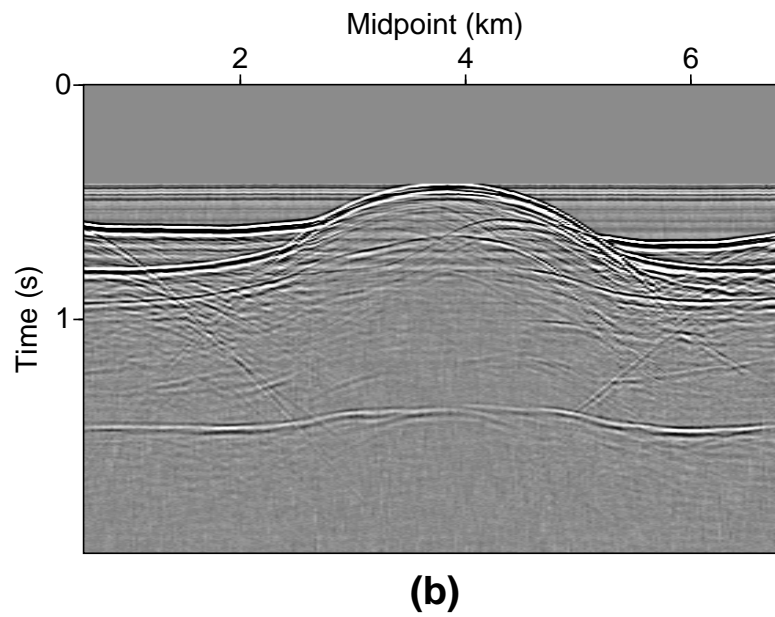
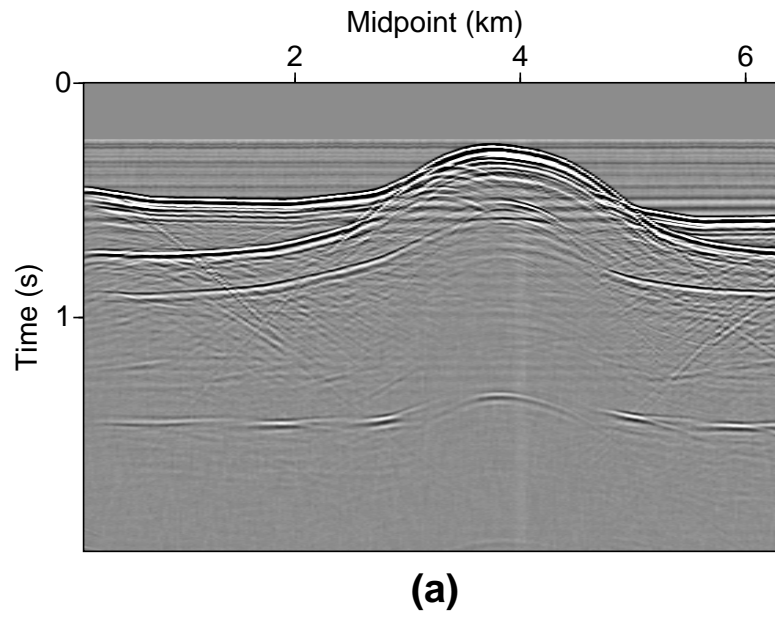


FIG. 6.11. Physical-tank data: (a) with offset of 268.2 meters and (b) with offset of 1243.6 meters.

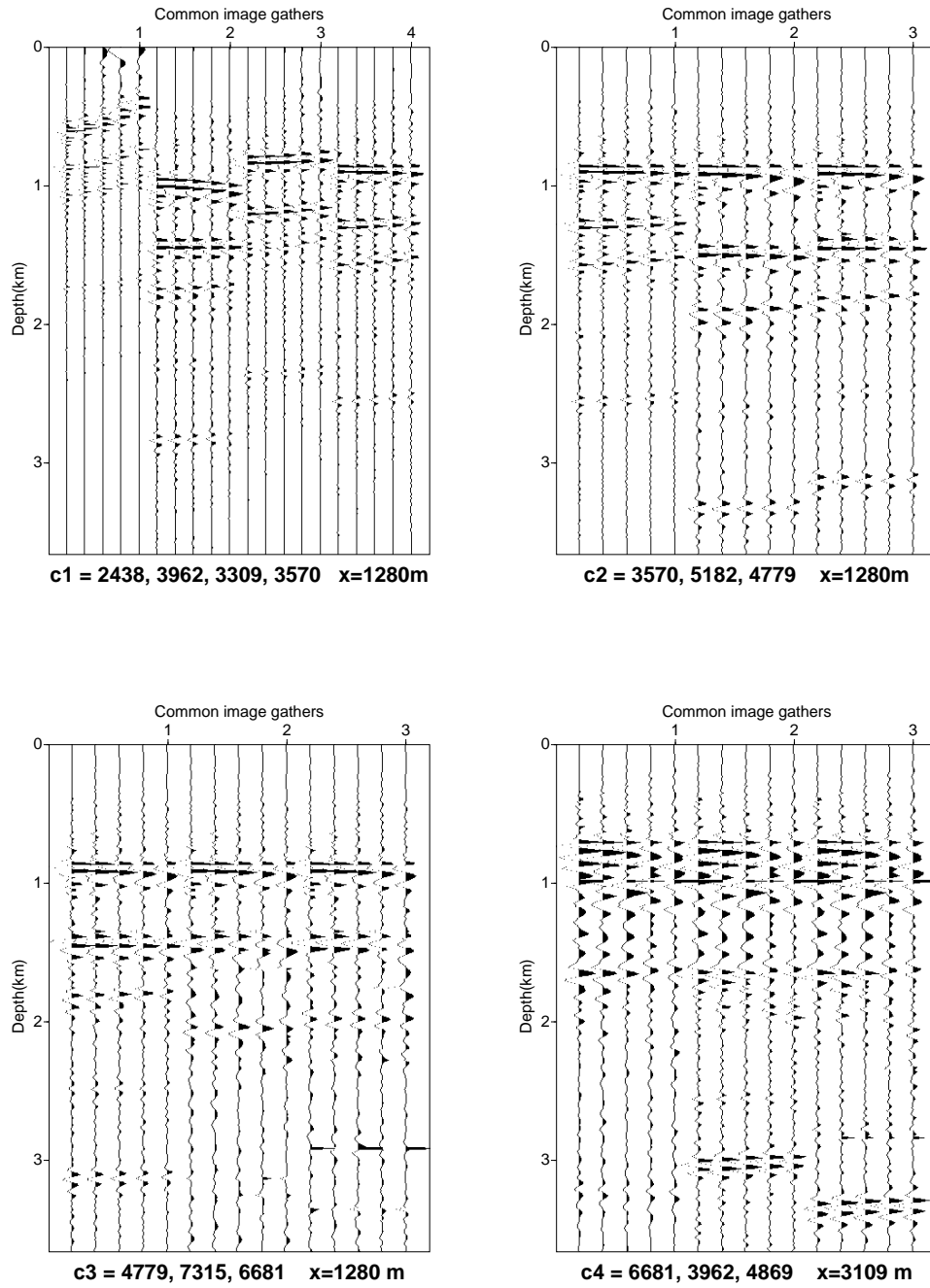


FIG. 6.12. Velocity analysis on the physical-tank data. The measured velocities:
 $c_1 = 3581, c_2 = 4801, c_3 = 6831, c_4 = 4801$.

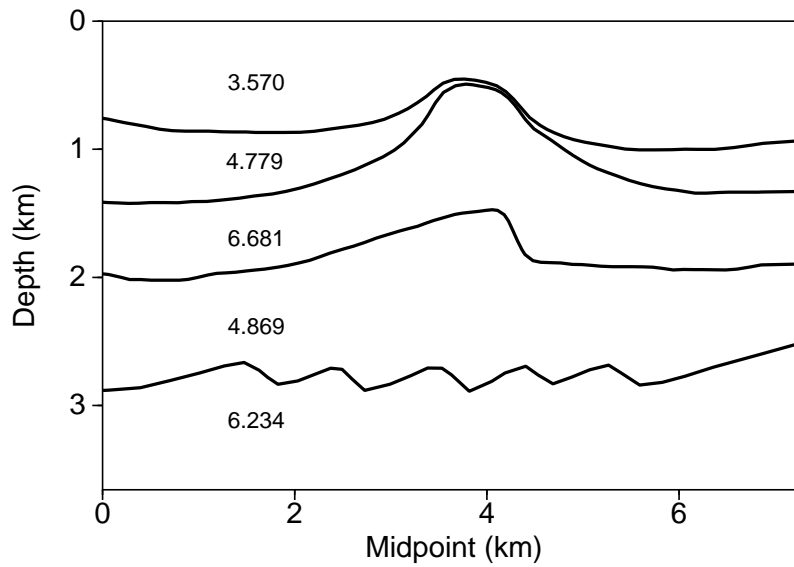


FIG. 6.13. Estimated velocity model from velocity analysis.

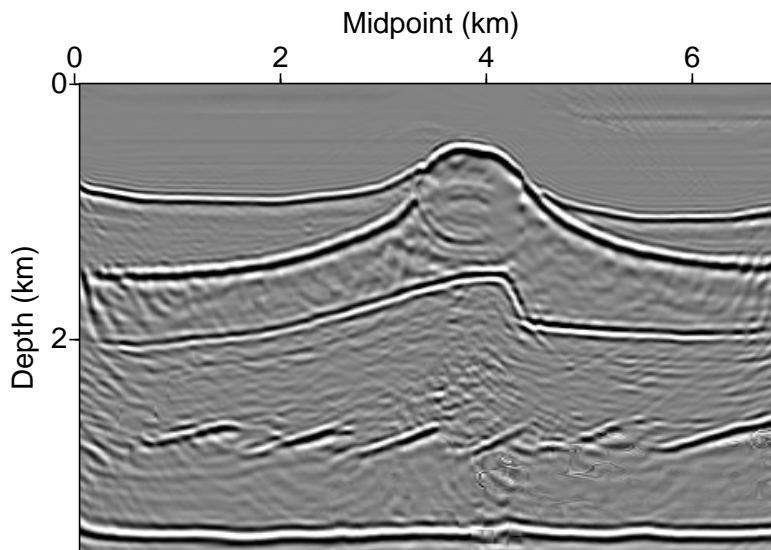


FIG. 6.14. Five-offset stacked migration output for the physical-tank data, AGC applied to the stack. The input velocity model is shown in Figure 6.13.

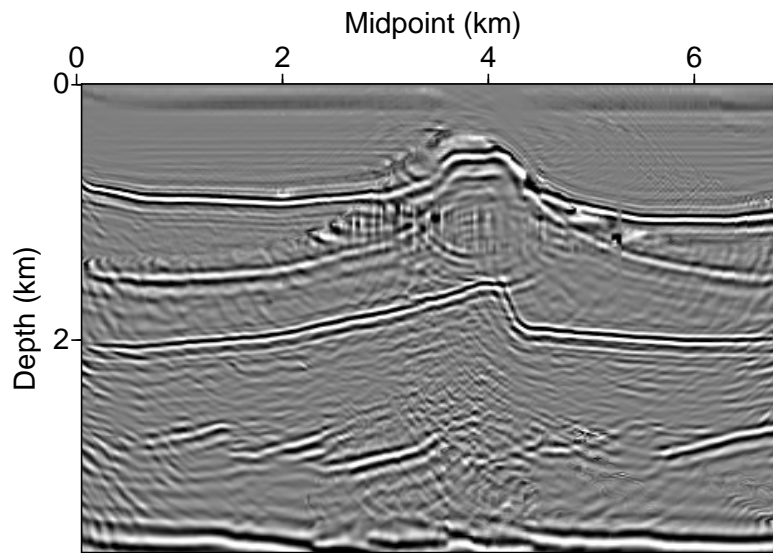


FIG. 6.15. Five-offset stacked inversion output for the physical-tank data, AGC applied to the stack. The input velocity model is shown in Figure 6.1.

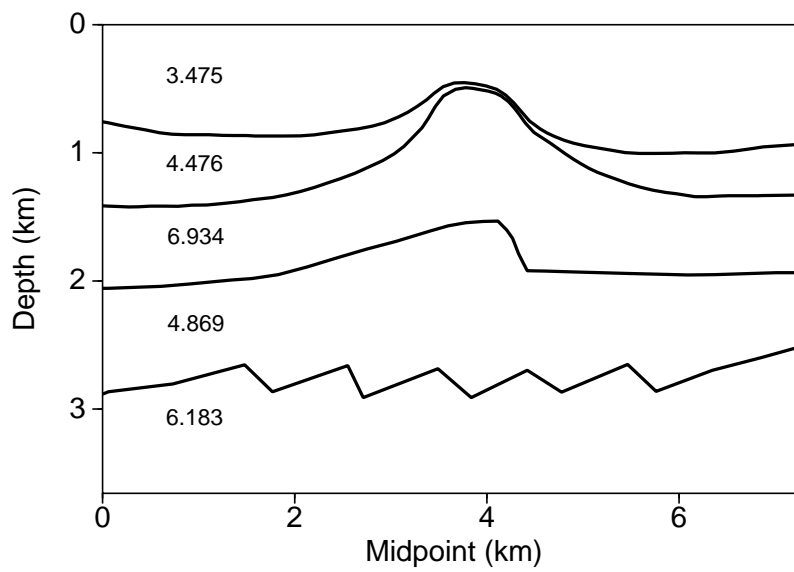


FIG. 6.16. Estimated velocity model from velocity analysis by perturbation.

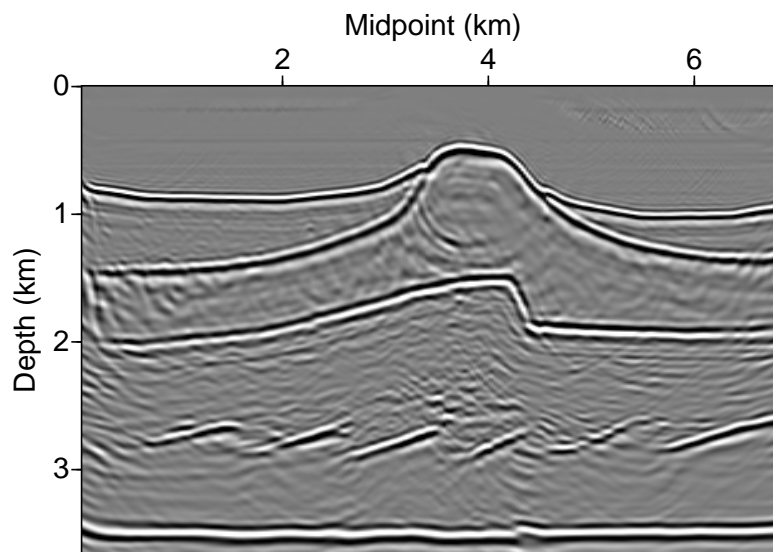


FIG. 6.17. Five-offset stacked migration output for the physical-tank data. The input velocity model is in Figure 6.16.

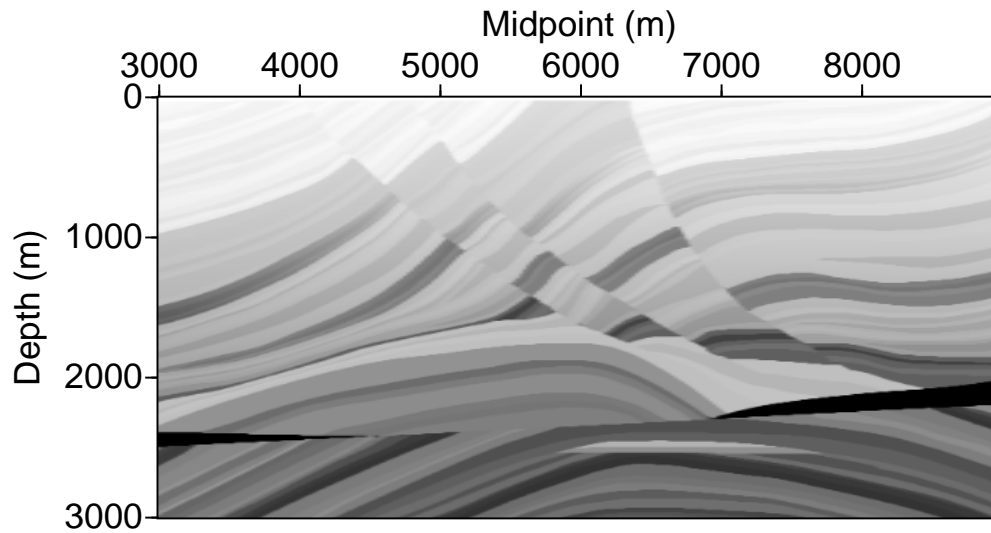


FIG. 6.18. The Marmousi velocity model. The darker shading denotes higher velocity.

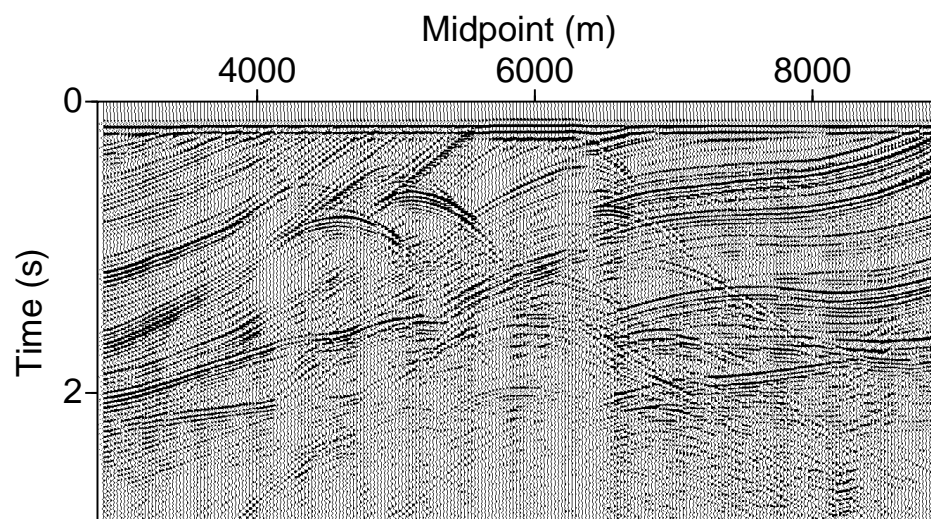


FIG. 6.19. The minimum-offset Marmousi data. The offset is 200 meters.

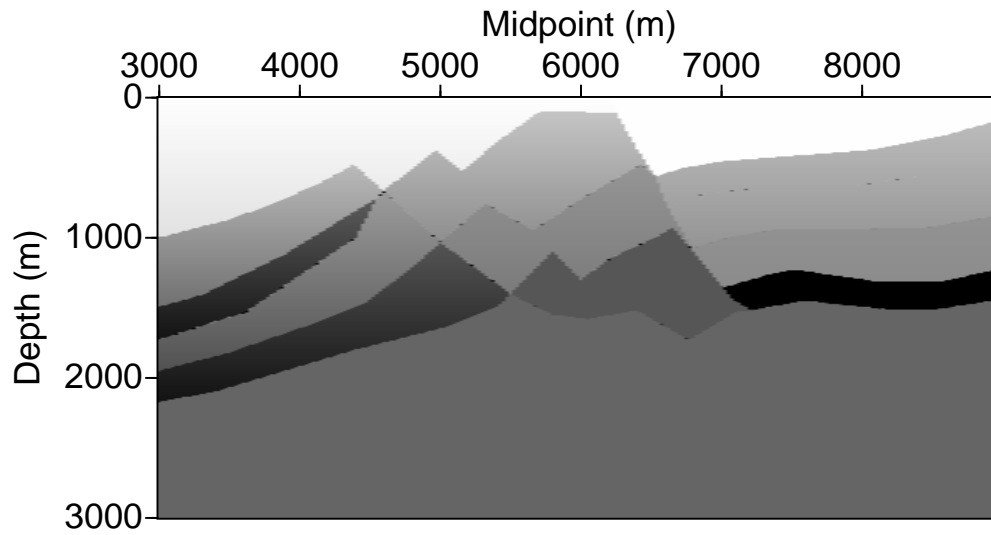


FIG. 6.20. The estimated velocity model using the first-arrival operator.

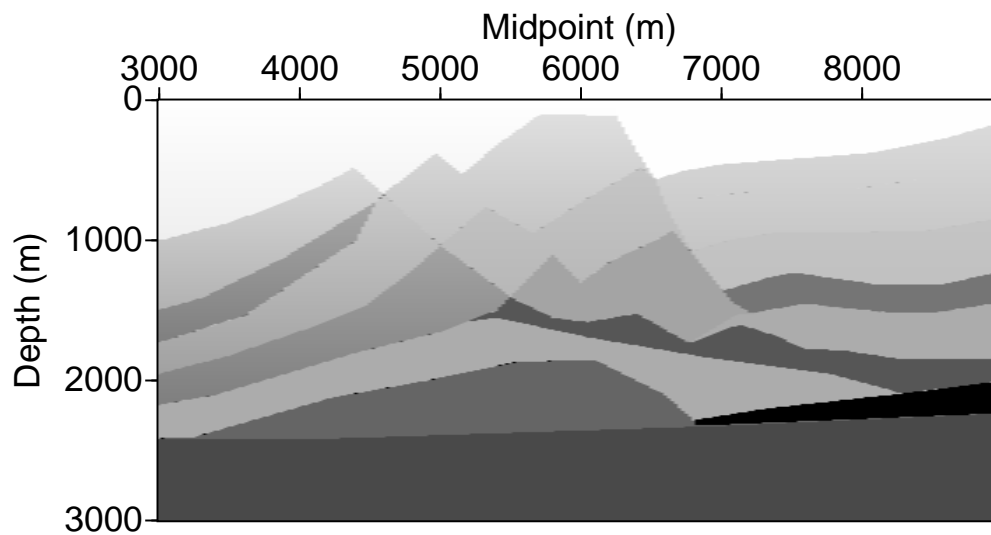


FIG. 6.21. The updated velocity model using the paraxial ray tracer.

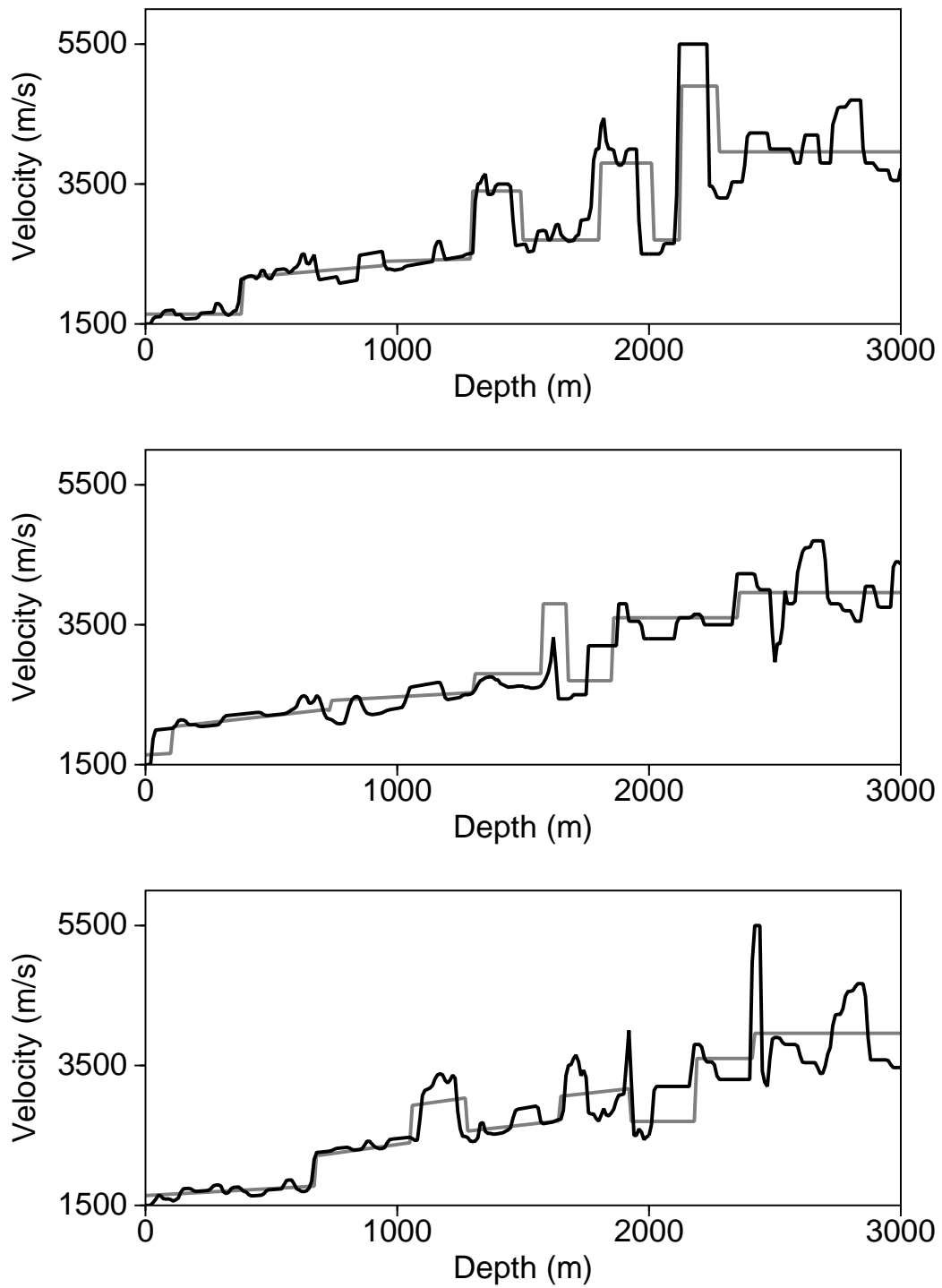


FIG. 6.22. Comparison of the true velocity model to the estimated one. The dark curve denotes the true velocity and the gray denotes the estimated velocity. The top figure is at location $x=8$ km; the middle, at location $x=6$ km; the bottom, at location $x=4$ km.

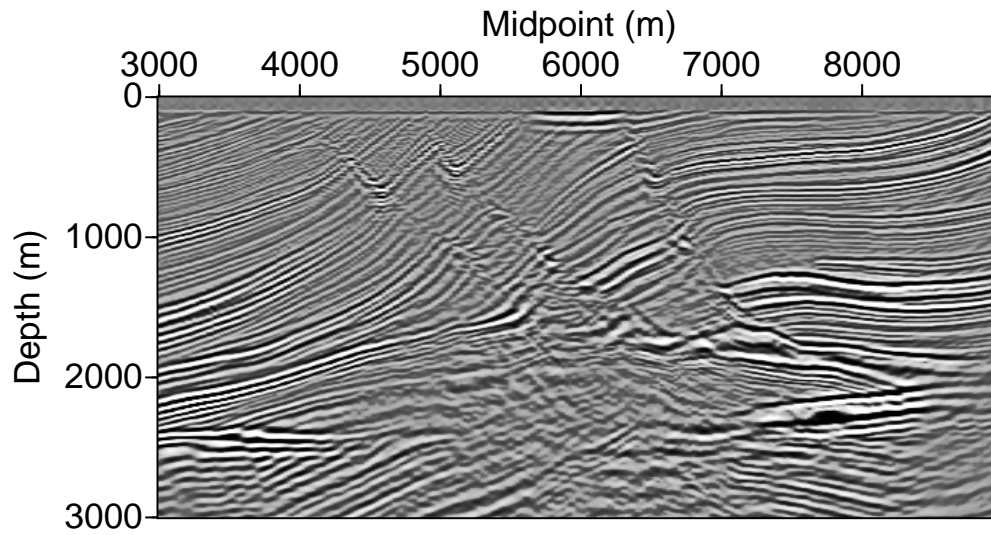


FIG. 6.23. 19-offset stacked migration output for the Marmousi data. The input velocity is one in Figure 6.21.

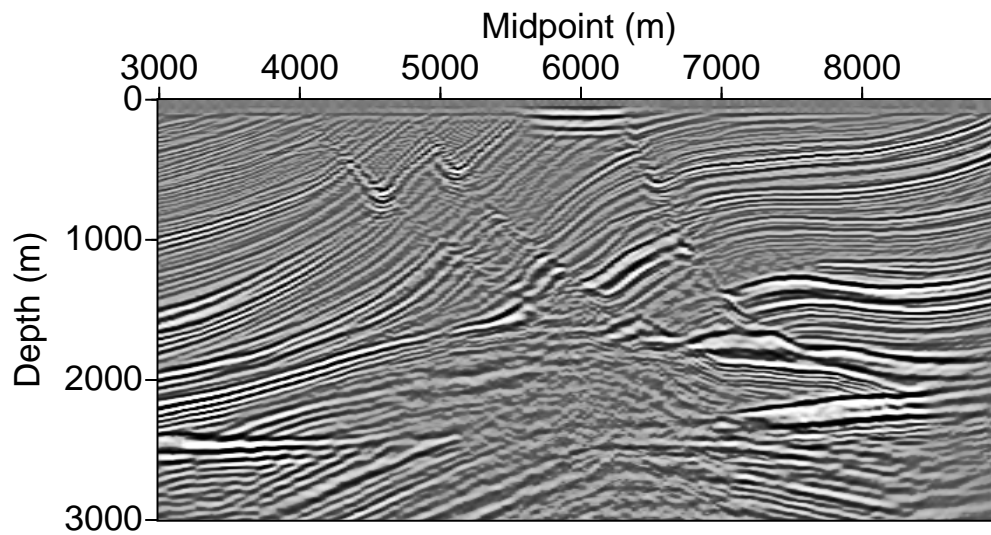


FIG. 6.24. 19-offset stacked migration output for the Marmousi data. The true velocity is used.

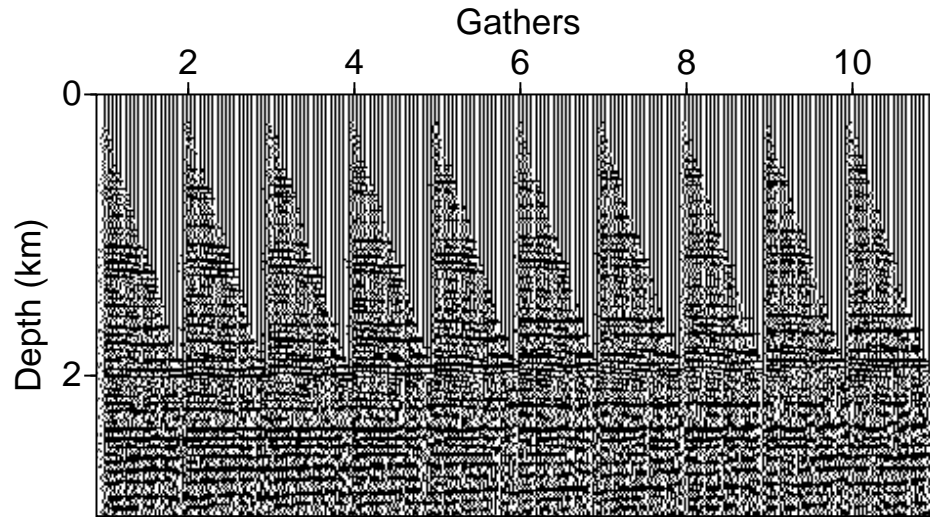


FIG. 6.25. Ten common image gathers. 19 offsets in each CIG. The image location ranges from 4 km to 4.25 km.

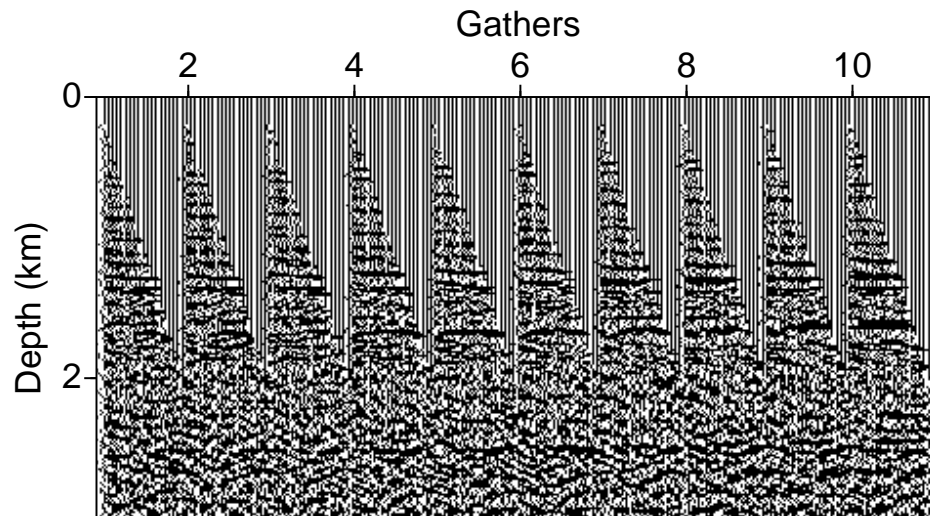


FIG. 6.26. Ten common image gathers. 19 offsets in each CIG. The image location ranges from 6 km to 6.25 km.

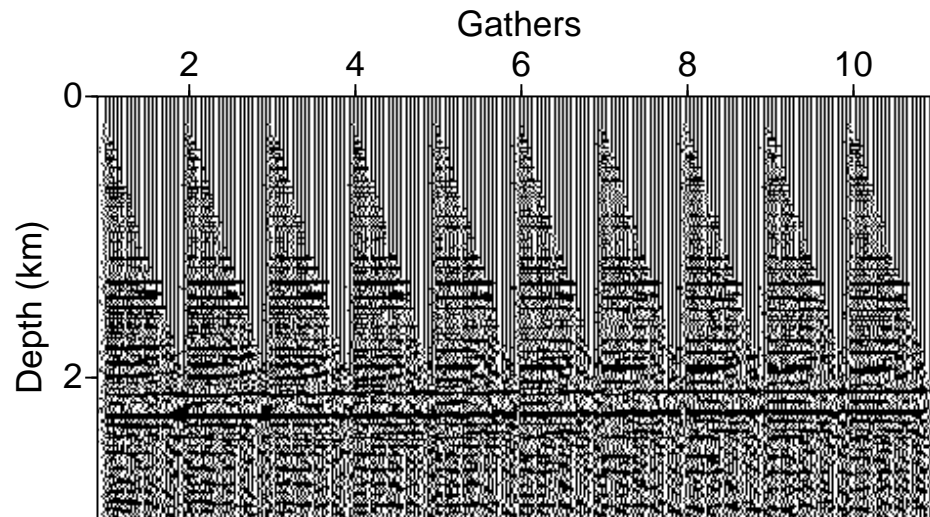


FIG. 6.27. Ten common image gathers. 19 offsets in each CIG. The image location ranges from 8 km to 8.25 km.

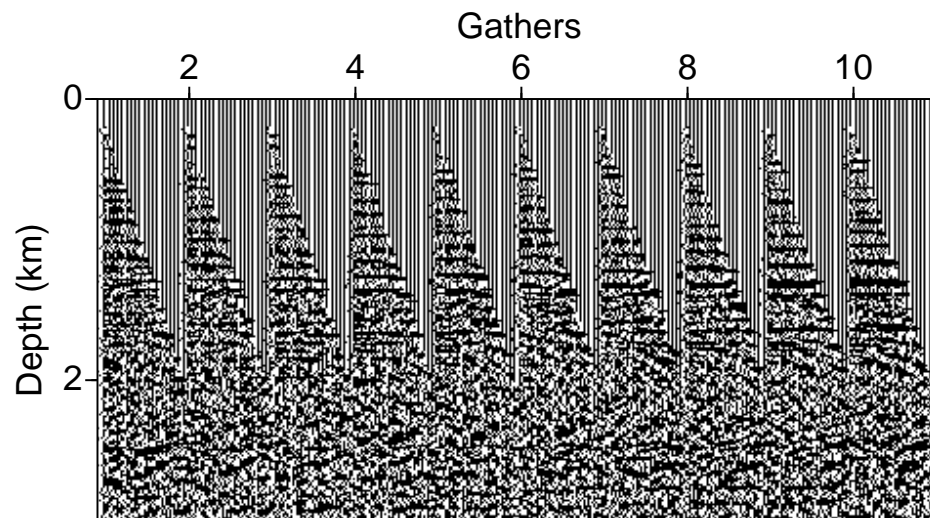


FIG. 6.28. Ten common image gathers from migrated data using the true velocity. The image location ranges from 6 km to 6.25 km.

Chapter 7

CONCLUSIONS

Prestack depth migration provides a powerful tool for knowing if a migration velocity is acceptable, because of its high sensitivity to a velocity model. Moreover, residual moveout in migrated data can be used to update an unacceptable velocity. In this thesis, I studied the relationship between residual moveout and migration velocity in a general context and derived analytical formulas to update velocities. For handling complex media, my formula estimates the update in velocity by computing a derivative function of imaged depths with respect to velocity in a general background medium context. This formula is more accurate than conventional formulas based on hyperbolic residual moveout when the medium has strongly lateral velocity variations. In this sense, I made contributions to theory and applications of migration velocity analysis. However, some questions remain with regard to efficient application of migration velocity analysis.

1. Efficient and accurate migration algorithms

In order to handle complex structures, repeated prestack migration is unavoidable in velocity updating. Therefore, the efficiency of migration velocity analysis largely depends on which prestack migration algorithm is used. In general, integral-type migration approaches, such as Kirchhoff or Gaussian beam, are preferable, because those methods can implement either common shot gathers or common offset gathers, and have the flexibility to image the targeted structures in which velocity

is being estimated. Besides the efficiency, the accuracy should be considered as well. For imaging complex structures, a migration algorithm should be designed to handle turning waves, and multivalued traveltimes.

In the Kirchhoff integral, traveltime calculation by ray tracing or finite differencing dominates the total cost. Finite differencing only calculates the first arrival traveltime, so this approach works fast but fails in calculation of multivalued traveltimes. Ray tracing by a shooting method may handle multivalued traveltimes, but the current algorithm is extremely time consuming (Sun, 1992). The paraxial ray method shows advantages in handling multivalued traveltimes and caustics. This method uses information from the standard dynamic ray-tracing method to extrapolate traveltimes and ray amplitudes at receivers in the vicinity of a central ray. In general, the traveltime calculation by the paraxial ray tracer is more costly than by finite differencing.

The cost of traveltime calculation in Kirchhoff migration may be reduced by generating a table of traveltimes, if the computer memory and disk space are allowable. In this way, the traveltime calculation at one location is implemented only one time, so the cost of traveltime calculation makes up relatively small portion of the total migration cost.

2. Interactive computational techniques

In practice, a velocity estimation procedure must involve interactive computational techniques, which is especially important in the 3-D case. During velocity analysis, one needs good computer graphics tools to pick imaged depths and to build and visualize the velocity model. Because of the limited resolution of velocity analysis, mathematical estimation of velocity models may be unreasonable and non-unique.

By means of computer graphical software, one can interpret and modify the velocity model based on some geological knowledge and information from other sources.

REFERENCES

- Al-Yahya, K., 1989, Velocity analysis by iterative profile migration: *Geophysics*, **54**, 718-729.
- Bleistein, N., 1984, *Mathematical Methods for Wave Phenomena*: Academic Press Inc.
- Bleistein, N., Cohen, J., and Hagin, F., 1987, Two and one-half dimensional Born inversion with an arbitrary reference: *Geophysics*, **52**, 26-36.
- Deregowski, S. M., 1990, Common-offset migrations and velocity analysis: *First break*, **8**, 6, 225-234.
- Doherty, S., and Claerbout, J., 1976, Structure independent velocity estimation: *Geophysics*, **41**, 850-881.
- Etgen, S., 1989, Kinematic residual prestack migration: *SEP*-**61**, 79-101.
- Geoltrain, S., and Brac, J., 1993, Can we image complex structures with first-arrival traveltimes migration: *Geophysics*, **58**, 564-575.
- Hubral, P., and Krey, T., 1980, *Interval Velocities from Seismic Reflection Time Measurements*: Soc. Explor. Geophys, Monograph.
- Jeannot, J. P., Faye, J. P., and Dennelle, E., 1986, Prestack migration velocities from depth-focusing analysis: 56th Ann. Internat. Mtg., Soc. Expl. Geophys., Expanded Abstracts, 438-440.
- Lafond, C. F. and Levander, A. R., 1993, Migration moveout analysis and depth focusing: *Geophysics*, **58**, 91-100.
- Lee, W., and Zhang, L., 1992, Residual shot profile migration: *Geophysics*, **57**, 815-822.
- Liu, Z., 1993, A Kirchhoff approach to seismic modeling and prestack depth migration: 1993 SEG expanded abstracts, p. 888.
- Liu, Z., and Bleistein, N., 1992, Velocity analysis by residual moveout: 1992 SEG expanded abstracts, p. 1034.

- Liu, Z., and Bleistein, N., 1994, Velocity analysis by perturbation: 1994 SEG expanded abstracts, p. 1191.
- Liu, Z., and Bleistein, N., 1995, Migration velocity analysis: theory and an iterative algorithm : *Geophysics*, **60**, 142-153.
- Lynn, W. S., and Claerbout, J. F., 1982, Velocity estimation in laterally varying media: *Geophysics*, **47**, 884-897.
- MacKay, S., and Abma, R., 1992, Imaging and velocity estimation with depth-focusing analysis: *Geophysics*, **57**, 1608-1622.
- MacKay, S., and Abma, R., 1993, Depth-focusing analysis using a wavefront-curvature criterion: *Geophysics*, **58**, 1148-1156.
- Stork, C., 1992, Reflection tomography in the postmigrated domain: *Geophysics*, **57**, 680-692.
- Stork, C., and R. W. Clayton, 1991, An implementation of tomographic velocity analysis: *Geophysics*, **56**, 472-482.
- Sun, Y., 1992, Computation of 2-D multiple arrival traveltimes by an interpolative shooting method: 1992 SEG expanded abstracts, p. 1320.
- Toldi, J., 1989, Velocity analysis without picking: *Geophysics*, **54**, 191-199.
- Versteeg, R., 1994, The Marmousi experience: velocity model determination on a synthetic complex data set: *The Leading EDGE*, **13**, 927-936.
- Zhang, L., 1991, Residual depth migration: 1991 SEG expanded abstracts, p. 1118.

Appendix A

DEPTH VARIATION TO VELOCITY

The purpose of this appendix is to show that the change in image depth z , with respect to changes in velocity is positive for downward propagating waves and negative for upward propagating turned rays. Suppose that migration velocity has a variation $\delta c = \delta c(\mathbf{x})$. For a fixed horizontal location x , the imaged depth z and the surface position parameter ξ are functionals of migration velocity. One takes the total variation in equation (2.5) with respect to δc ; then

$$\left[\frac{\partial \tau_s}{\partial \xi} + \frac{\partial \tau_r}{\partial \xi} \right] \delta \xi + [\delta_c \tau_s + \delta_c \tau_r] + \left[\frac{\partial \tau_s}{\partial z} + \frac{\partial \tau_r}{\partial z} \right] \delta z = \frac{dt}{d\xi} \delta \xi. \quad (\text{A.1})$$

Here δ_c is used to denote the partial functional variation from δc . For example, $\delta_c \tau_s$ means the variation of τ_s related to changing c for fixed \mathbf{x} and ξ . Using equation (2.6) to eliminate $\partial \tau_s / \partial \xi$ and $\partial \tau_r / \partial \xi$ yields

$$\left[\frac{\partial \tau_s}{\partial z} + \frac{\partial \tau_r}{\partial z} \right] \delta z = -[\delta_c \tau_s(\mathbf{x}_s, \mathbf{x}) + \delta_c \tau_r(\mathbf{x}_s, \mathbf{x})].$$

The derivatives of traveltimes with respect to depth can be represented by

$$\frac{\partial \tau_s(\mathbf{x}_s, \mathbf{x})}{\partial z} = \frac{\cos(\theta_s)}{c(\mathbf{x})}, \quad \frac{\partial \tau_r(\mathbf{x}_r, \mathbf{x})}{\partial z} = \frac{\cos(\theta_r)}{c(\mathbf{x})},$$

where θ_s or θ_r are the angles between the ray direction from the source or the receiver, respectively, and the downward pointing vertical direction at \mathbf{x} , or, equivalently, the

angle of incidence from the source or receiver, respectively, measured to the upward vertical direction. I then rewrite δz as

$$\delta z = -\frac{c(\mathbf{x})[\delta_c \tau_s(\mathbf{x}_s, \mathbf{x}) + \delta_c \tau_r(\mathbf{x}_s, \mathbf{x})]}{\cos(\theta_s) + \cos(\theta_r)}. \quad (\text{A.2})$$

An increase in c — δc positive—always results in a *decrease* in the traveltimes— $\delta_c \tau_s + \delta_c \tau_r$ —negative, so that the numerator on the right is negative. More precisely, an increase in the averaged c along raypaths does the same work. In addition,

$$\cos(\theta_s) + \cos(\theta_r) = 2 \cos\left(\frac{\theta_s + \theta_r}{2}\right) \cos\left(\frac{\theta_r - \theta_s}{2}\right).$$

In this equation, $\theta_r - \theta_s$ is the angle between the two raypaths, so $|\theta_r - \theta_s|/2 < 90^\circ$, i.e.,

$$\cos\left(\frac{\theta_r - \theta_s}{2}\right) > 0.$$

$(\theta_r + \theta_s)/2$ is the angle between the normal of reflection and the up-vertical. For downward propagating waves, $(\theta_r + \theta_s)/2 < 90^\circ$, so

$$\cos\left(\frac{\theta_r + \theta_s}{2}\right) > 0;$$

for upward propagating waves (turned waves), $(\theta_r + \theta_s)/2 > 90^\circ$, so

$$\cos\left(\frac{\theta_r + \theta_s}{2}\right) < 0.$$

Thus, when taking account of the minus sign on the right side of the equation (A.2), I conclude that the variation in the imaged depth with respect to increment in the propagation speed is positive for downward propagating waves and is negative

for upward propagating (turned waves). This is true for any velocity distribution.

Appendix B

RMO VELOCITY REPRESENTATION FOR $V(Z)$

In this appendix, the representation of RMO velocity is derived for a laterally invariant velocity medium and a reflector dip.

From Taylor's expansion,

$$(1 - p^2 v^2(\sigma))^{-3/2} = 1 + \frac{3}{2} v^2(\sigma) p^2 + O(p^4), \quad (\text{B.1})$$

so that

$$\int_0^{\tau^*} v^2(\sigma) (1 - p^2 v^2(\sigma))^{-3/2} d\sigma = \int_0^{\tau^*} v^2 d\sigma + \frac{3}{2} p^2 \int_0^{\tau^*} v^4 d\sigma = \tau^* (v_2^2 + \frac{3}{2} v_4^4 p^2), \quad (\text{B.2})$$

and

$$\int_0^{\tau^*} (1 - p^2 v^2(\sigma))^{-3/2} d\sigma = \tau^* (1 + \frac{3}{2} v_2^2 p^2). \quad (\text{B.3})$$

Using equations (B.1) and (B.2), and the definition in (4.53), I obtain

$$v_{rmo}^2 = \frac{\tau^* (v_2^2 + 3/2 v_4^4 p^2)}{\tau^* (1 + 3/2 v_2^2 p^2)} = v_2^2 + \frac{3}{2} (v_4^4 - v_2^4) p^2 + O(p^4). \quad (\text{B.4})$$

Thus, the derivation of equation (4.55) is completed.

Appendix C

LATERAL VELOCITY ANOMALY

In this appendix, the representation of RMO velocity is derived for horizontal reflectors and the medium with a lateral velocity anomaly.

Suppose that reflectors are horizontal and the true slowness $w(x, z)$ can be written by

$$w(x, z) = \bar{w}(z) (1 + \alpha(x, z)) = \frac{1}{\bar{v}(z)} (1 + \alpha(x, z)), \quad (\text{C.1})$$

where $\bar{w}(z)$ is a reference slowness and $\alpha(x, z)$ is a small perturbation. The two-way travelttime \bar{t} in the medium of \bar{w} is represented by

$$\bar{t}(y, h) = 2 \int_0^z \frac{\bar{w}(\sigma)}{\cos \theta} d\sigma, \quad (\text{C.2})$$

where θ is the angle of the ray path from the vertical, y is the midpoint. Because the reflectors are horizontal and the medium velocity is a depth-dependent function plus a small lateral perturbation, I conclude that the reflection point equals approximately the midpoint, i.e, $x = y$. Under the assumption of a small perturbation, the ray path in the medium of $w(x, z)$ is the same as that in the medium of \bar{w} , so the two-way travelttime in the medium of $w(x, z)$ is

$$t(y, h) = 2 \int_0^z \frac{w(\xi(\sigma), \sigma)}{\cos \theta} d\sigma = \bar{t}(h, y) + 2 \int_0^z \frac{\alpha(\xi(\sigma), \sigma)}{\cos \theta} \frac{d\sigma}{\bar{v}(\sigma)}, \quad (\text{C.3})$$

where (ξ, σ) is a point on the ray path and

$$\xi(\sigma) = y + \int_{\sigma}^z \tan \theta ds. \quad (\text{C.4})$$

In particular, $\xi(0) = h - y$. Taking a second-derivative with respect to h in equation (C.3) gives

$$\left. \frac{\partial^2 t(h, y)}{\partial h^2} \right|_{h=0} = \left. \frac{\partial^2 \bar{t}(h, y)}{\partial h^2} \right|_{h=0} + 2 \int_0^z \frac{\partial^2}{\partial h^2} \left[\frac{\alpha(\xi, \sigma)}{\cos \theta} \right]_{h=0} \frac{d\sigma}{\bar{v}(\sigma)}. \quad (\text{C.5})$$

Furthermore,

$$\frac{\partial^2}{\partial h^2} \left[\frac{\alpha(\xi, \sigma)}{\cos \theta} \right] = \frac{\partial^2 \alpha}{\partial h^2} \frac{1}{\cos \theta} + 2 \frac{\partial \alpha}{\partial h} \frac{\partial}{\partial h} \left(\frac{1}{\cos \theta} \right) + \alpha(\xi, \sigma) \frac{\partial^2}{\partial h^2} \left(\frac{1}{\cos \theta} \right). \quad (\text{C.6})$$

The fact that $\theta = 0$ at $h = 0$ gives

$$\left. \frac{\partial}{\partial h} \left(\frac{1}{\cos \theta} \right) \right|_{h=0} = \left. \left(\frac{\sin \theta}{\cos^2 \theta} \frac{\partial \theta}{\partial h} \right) \right|_{h=0} = 0, \quad (\text{C.7})$$

and

$$\cos \theta |_{h=0} = 1. \quad (\text{C.8})$$

Using equations (C.7) and (C.8), I simplify equation (C.6) to

$$\left. \frac{\partial^2}{\partial h^2} \left[\frac{\alpha(\xi, \sigma)}{\cos \theta} \right] \right|_{h=0} = \left. \frac{\partial^2 \alpha}{\partial h^2} \right|_{h=0} + \alpha(y, \sigma) \left. \frac{\partial^2}{\partial h^2} \left(\frac{1}{\cos \theta} \right) \right|_{h=0}. \quad (\text{C.9})$$

Notice that ξ is a function of h , so it follows from the chain rule that

$$\frac{\partial^2 \alpha}{\partial h^2} = \frac{\partial^2 \alpha}{\partial \xi^2} \left(\frac{\partial \xi}{\partial h} \right)^2 + \frac{\partial \alpha}{\partial \xi} \frac{\partial^2 \xi}{\partial h^2}. \quad (\text{C.10})$$

From (C.4), $\xi - y$ is an odd function of h ; hence

$$\left. \frac{\partial^2 \xi}{\partial h^2} \right|_{h=0} = \left. \frac{\partial^2 (\xi - y)}{\partial h^2} \right|_{h=0} = 0. \quad (\text{C.11})$$

This result and equation (C.10) give

$$\left. \frac{\partial^2 \alpha}{\partial h^2} \right|_{h=0} = \left. \frac{\partial^2 \alpha}{\partial y^2} \left(\frac{\partial \xi}{\partial h} \right)^2 \right|_{h=0}. \quad (\text{C.12})$$

Here I use the fact that $\xi = y$ at $h = 0$. From $\theta = 0$ at $h = 0$, and

$$\frac{\partial^2}{\partial h^2} \left(\frac{1}{\cos \theta} \right) = \left(\frac{\sin \theta}{\cos^2 \theta} \frac{\partial^2 \theta}{\partial h^2} \right) + \frac{1 + \sin^2 \theta}{\cos^3 \theta} \left(\frac{\partial \theta}{\partial h} \right)^2, \quad (\text{C.13})$$

I obtain

$$\left. \frac{\partial^2}{\partial h^2} \left(\frac{1}{\cos \theta} \right) \right|_{h=0} = \left. \left(\frac{\partial \theta}{\partial h} \right)^2 \right|_{h=0}. \quad (\text{C.14})$$

In order to do further calculations, I introduce the slope parameter

$$p = \frac{\sin \theta}{\bar{v}(\sigma)}, \quad (\text{C.15})$$

which is independent of σ ; then

$$\cos \theta = \sqrt{1 - (\bar{v}p)^2}. \quad (\text{C.16})$$

From this result and equation (C.4),

$$\xi(\sigma) = y + \int_{\sigma}^z \frac{\bar{v}p}{\sqrt{1 - (\bar{v}p)^2}} ds, \quad (\text{C.17})$$

and

$$h = \int_0^z \frac{\bar{v}p}{\sqrt{1 - (\bar{v}p)^2}} ds. \quad (\text{C.18})$$

These formulas imply that

$$\frac{\partial \xi}{\partial p} = \int_\sigma^z \frac{\bar{v}}{[1 - (\bar{v}p)^2]^{3/2}} ds, \quad (\text{C.19})$$

$$\frac{dh}{dp} = \int_0^z \frac{\bar{v}}{[1 - (\bar{v}p)^2]^{3/2}} ds, \quad (\text{C.20})$$

$$\frac{\partial \theta}{\partial p} = \frac{\bar{v}}{\cos \theta}. \quad (\text{C.21})$$

Equations (C.19) and (C.20) yields

$$\left. \frac{\partial \xi}{\partial h} \right|_{h=0} = \left[\frac{\partial \xi}{\partial p} \left(\frac{dh}{dp} \right)^{-1} \right]_{h=0} = \frac{\int_\sigma^z \bar{v} ds}{\int_0^z \bar{v} ds} = \frac{2 \int_\sigma^z \bar{v} ds}{\bar{t}_0 \bar{v}_s^2(z)}, \quad (\text{C.22})$$

where \bar{v}_s is the asymptotic stacking velocity of \bar{v} and $\bar{t}_0 = \bar{t}(y, 0)$; equations (C.20) and (C.21) yield

$$\left. \frac{\partial \theta}{\partial h} \right|_{h=0} = \left[\frac{\partial \theta}{\partial p} \left(\frac{dh}{dp} \right)^{-1} \right]_{h=0} = \frac{\bar{v}(\sigma)}{\int_0^z \bar{v} ds} = \frac{2\bar{v}(\sigma)}{\bar{t}_0 \bar{v}_s^2(z)}. \quad (\text{C.23})$$

Substituting equations (C.12), (C.14), (C.22) and (C.23) into equation (C.9), I obtain

$$\left. \frac{\partial^2}{\partial h^2} \left(\frac{\alpha(\xi, \sigma)}{\cos \theta} \right) \right|_{h=0} = \frac{\partial^2 \alpha}{\partial y^2} \left(\frac{2 \int_\sigma^z \bar{v} ds}{\bar{t}_0 \bar{v}_s^2(z)} \right)^2 + \alpha(y, \sigma) \frac{4\bar{v}^2(\sigma)}{\bar{t}_0^2 \bar{v}_s^4(z)}. \quad (\text{C.24})$$

Substituting equation (C.24) into equation (C.7), yields

$$\left. \frac{\partial^2 t}{\partial h^2} \right|_{h=0} = \left. \frac{\partial^2 \bar{t}}{\partial h^2} \right|_{h=0} + \frac{8}{\bar{t}_0^2 \bar{v}_s^2(z)} \int_0^z \left[\frac{\partial^2 \alpha}{\partial y^2} \frac{(\int_\sigma^z \bar{v} ds)^2}{\bar{v}_s^2(z)} + \frac{\alpha \bar{v}^2(\sigma)}{\bar{v}_s^2(z)} \right] \frac{d\sigma}{\bar{v}(\sigma)}. \quad (\text{C.25})$$

The asymptotic stacking velocity v_s and \bar{v}_s are calculated by

$$w_s^2(y, z) = \frac{1}{v_s^2(y, z)} = \frac{1}{4} \left[t(y, h) \frac{\partial^2 t(y, h)}{\partial h^2} \right]_{h=0}, \quad (\text{C.26})$$

$$\bar{w}_s(z) = \frac{1}{\bar{v}_s^2(z)} = \frac{1}{4} \left[\bar{t}(y, h) \frac{\partial^2 \bar{t}(y, h)}{\partial h^2} \right]_{h=0}. \quad (\text{C.27})$$

Using equations (C.3), (C.26), (C.27), and notation $\bar{t}_0 = \bar{t}(y, 0)$, I obtain

$$\begin{aligned} t(y, 0) \frac{\partial^2 t(h, y)}{\partial h^2} \Big|_{h=0} - t(y, 0) \frac{\partial^2 \bar{t}(h, y)}{\partial h^2} \Big|_{h=0} &= 4w_s^2(y, z) - 4\bar{w}_s^2(z) \frac{t(y, 0)}{\bar{t}_0} \\ &= 4w_s^2(y, z) - 4\bar{w}_s^2(z) - \frac{8\bar{w}_s^2(z)}{\bar{t}_0} \int_0^z \alpha(y, \sigma) \frac{d\sigma}{\bar{v}(\sigma)}, \end{aligned} \quad (\text{C.28})$$

that is,

$$w_s^2(y, z) - \bar{w}_s^2(z) = \frac{2\bar{w}_s^2}{\bar{t}_0} \int_0^z \alpha(y, \sigma) \frac{d\sigma}{\bar{v}(\sigma)} + \frac{t(y, 0)}{4} \left[\frac{\partial^2 t}{\partial h^2} \Big|_{h=0} - \frac{\partial^2 \bar{t}}{\partial h^2} \Big|_{h=0} \right] \quad (\text{C.29})$$

When α is small, \bar{t} is an approximation of t . By ignoring the second-order perturbation, I obtain

$$\frac{t(y, 0)}{4} \left[\frac{\partial^2 t}{\partial h^2} \Big|_{h=0} - \frac{\partial^2 \bar{t}}{\partial h^2} \Big|_{h=0} \right] = \frac{\bar{t}_0}{4} \left[\frac{\partial^2 t}{\partial h^2} \Big|_{h=0} - \frac{\partial^2 \bar{t}}{\partial h^2} \Big|_{h=0} \right] \quad (\text{C.30})$$

Using equations (C.25), (C.29) and (C.30), I obtain

$$w_s^2(y, z) - \bar{w}_s^2(z) = \frac{2\bar{w}_s^2}{\bar{t}_0} \int_0^z \alpha \frac{d\sigma}{\bar{v}(\sigma)} + \frac{2}{\bar{t}_0 \bar{v}_s^2} \int_0^z \left[\frac{\partial^2 \alpha}{\partial y^2} \frac{(\int_0^z \bar{v} ds)^2}{\bar{v}_s^2(z)} + \frac{\alpha \bar{v}^2(\sigma)}{\bar{v}_s^2(z)} \right] \frac{d\sigma}{\bar{v}(\sigma)}. \quad (\text{C.31})$$

Notice that $y = x$, so the above equation becomes

$$\frac{w_s^2(x, z)}{\bar{w}_s^2(z)} - 1 = \frac{2}{\bar{t}_0} \int_0^z \left[\frac{\partial^2 \alpha}{\partial x^2} \left(\frac{\int_0^z \bar{v} ds}{\bar{v}_s(z)} \right)^2 + \alpha(x, \sigma) \left(1 + \frac{\bar{v}^2(\sigma)}{\bar{v}_s^2(z)} \right) \right] \frac{d\sigma}{\bar{v}(\sigma)}, \quad (\text{C.32})$$

which is the result I stated in equation (4.65).

Appendix D

EQUATION SYSTEM FOR PERTURBATION

In this appendix, a linear equation system is derived for parameter estimation in the perturbation method of Chapter 5.

By using the matrix and vector notations in equation (5.18), I obtain

$$\begin{aligned}
 \overline{\Delta \hat{z}^{(k)}} &= \frac{1}{m} \sum_{j=1}^m \Delta z_j^{(k)} \\
 &= \frac{1}{m} \sum_{j=1}^m \sum_{i=1}^n g_{ij}^{(k)} \Delta \lambda_i \\
 &= \sum_{i=1}^n \left(\Delta \lambda_i \frac{1}{m} \sum_{j=1}^m g_{ij}^{(k)} \right) \\
 &= \sum_{i=1}^n \left(\Delta \lambda_i \overline{\hat{g}_i^{(k)}} \right), \tag{D.1}
 \end{aligned}$$

and

$$\begin{aligned}
 z_j^{(k)} + \Delta z_j^{(k)} - \overline{\hat{z}^{(k)} + \Delta \hat{z}^{(k)}} &= z_j^{(k)} - \overline{\hat{z}^{(k)}} + \Delta z_j^{(k)} - \overline{\Delta \hat{z}^{(k)}} \\
 &= z_j^{(k)} - \overline{\hat{z}^{(k)}} + \sum_{i=1}^n \Delta \lambda_i \left(g_{ij}^{(k)} - \overline{\hat{g}_i^{(k)}} \right). \tag{D.2}
 \end{aligned}$$

Define a quadratic objective function

$$f(\Delta \hat{\lambda}) \equiv \sum_{k=1}^K \sum_{j=1}^m \left(z_j^{(k)} + \Delta z_j^{(k)} - \overline{\hat{z}^{(k)} + \Delta \hat{z}^{(k)}} \right)^2.$$

Thus, finding the minimum of $f(\Delta \hat{\lambda})$ is equivalent to setting its gradient with respect

to $\Delta\hat{\lambda}$ equal $\hat{0}$, i.e.,

$$\frac{\partial f(\Delta\hat{\lambda})}{\partial \Delta\lambda_l} = 0 \quad l = 1, 2, \dots, n. \quad (\text{D.3})$$

By using equation (D.2),

$$f(\Delta\hat{\lambda}) = \sum_{k=1}^K \sum_{j=1}^m \left[z_j^{(k)} - \overline{\hat{z}^{(k)}} + \sum_{i=1}^n \Delta\lambda_i \left(g_{ij}^{(k)} - \overline{\hat{g}_i^{(k)}} \right) \right]^2.$$

The derivatives computed from function are

$$\begin{aligned} \frac{\partial f(\Delta\hat{\lambda})}{\partial \Delta\lambda_l} &= 2 \sum_{k=1}^K \sum_{j=1}^m \left[z_j^{(k)} - \overline{\hat{z}^{(k)}} + \sum_{i=1}^n \Delta\lambda_i \left(g_{ij}^{(k)} - \overline{\hat{g}_i^{(k)}} \right) \right] \left(g_{lj}^{(k)} - \overline{\hat{g}_l^{(k)}} \right) \\ &= 2 \sum_{k=1}^K \sum_{j=1}^m \left(z_j^{(k)} - \overline{\hat{z}^{(k)}} \right) \left(g_{lj}^{(k)} - \overline{\hat{g}_l^{(k)}} \right) \\ &\quad + 2 \sum_{k=1}^K \sum_{j=1}^m \sum_{i=1}^n \Delta\lambda_i \left(g_{ij}^{(k)} - \overline{\hat{g}_i^{(k)}} \right) \left(g_{lj}^{(k)} - \overline{\hat{g}_l^{(k)}} \right). \end{aligned} \quad (\text{D.4})$$

The condition (D.3) implies that

$$\sum_{k=1}^K \sum_{j=1}^m \sum_{i=1}^n \Delta\lambda_i \left(g_{ij}^{(k)} - \overline{\hat{g}_i^{(k)}} \right) \left(g_{lj}^{(k)} - \overline{\hat{g}_l^{(k)}} \right) = - \sum_{k=1}^K \sum_{j=1}^m \left(z_j^{(k)} - \overline{\hat{z}^{(k)}} \right) \left(g_{lj}^{(k)} - \overline{\hat{g}_l^{(k)}} \right);$$

i.e.,

$$\left[\sum_{k=1}^K A^{(k)} \right] \Delta\hat{\lambda} = - \sum_{k=1}^K \hat{b}^{(k)}. \quad (\text{D.5})$$

Thus, I completes the verification that the solution of equation (5.21) is just the minimum of the left side in (5.20).

Appendix E

DERIVATIVE FUNCTIONS IN SIMPLE CASES

In this appendix, the representation of derivatives of imaged depths with respect to velocity and velocity vertical gradient is derived for a horizontal reflector and a constant background velocity.

From equation (5.23),

$$\frac{\partial \tau}{\partial \lambda} = \int_L \frac{\partial}{\partial \lambda} \left(\frac{1}{v(x, z)} \right) dl = - \int_L v^{-2}(x, z) \frac{\partial v(x, z)}{\partial \lambda} dl, \quad (\text{E.1})$$

where L is the raypath. Here, to simplify notation, I suppose that all derivatives with respect to λ are evaluated at $\lambda_1 = \lambda_2 = 0$. When the background velocity is a constant v_0 as in equation (5.24), equation (E.1) becomes

$$\frac{\partial \tau}{\partial \lambda} = - \frac{1}{\cos \theta} \int_0^z v_0^{-2} \frac{\partial v(x, z')}{\partial \lambda} dz', \quad (\text{E.2})$$

where θ is the angle between the raypath and the vertical. For the velocity function in equation (5.28), if $z > d$, then

$$\frac{\partial v(x, z')}{\partial \lambda_1} = 1,$$

and

$$\frac{\partial v(x, z')}{\partial \lambda_2} = z' - z_0;$$

if $z < d$, then

$$\frac{\partial v(x, z')}{\partial \lambda_1} = \frac{\partial v(x, z')}{\partial \lambda_2} = 0.$$

Therefore,

$$\frac{\partial \tau}{\partial \lambda_1} = -\frac{1}{\cos \theta} \int_d^z \frac{1}{v_0^2} dz' = -\frac{1}{\cos \theta} \frac{z - d}{v_0^2}, \quad (\text{E.3})$$

and

$$\frac{\partial \tau}{\partial \lambda_2} = -\frac{1}{\cos \theta} \int_d^z \frac{z' - z_0}{v_0^2} dz' = -\frac{1}{\cos \theta} \frac{(z - z_0)^2 - (d - z_0)^2}{2v_0^2}. \quad (\text{E.4})$$

Because the reflector is horizontal, the ray paths from the source and the receiver are symmetric. I obtain

$$\cos \theta_s = \cos \theta_r = \frac{z}{\sqrt{z^2 + h^2}}.$$

Substituting the above formula and equations (E.3) and (E.4) into equation (5.13), yields

$$g_1(x, h) = \frac{h^2 + z^2}{z^2} \frac{z - d}{v_0},$$

and

$$g_2(x, h) = \frac{h^2 + z^2}{z^2} \frac{(z - z_0)^2 - (d - z_0)^2}{2v_0}.$$

Thus, I completes the verifications of equations (5.29) and (5.30).